CREEP BEHAVIOR IN INTERLAMINAR SHEAR OF A CVI SIC/SIC COMPOSITE AT ELEVATED TEMPERATURE IN AIR AND IN STEAM

THESIS

Matthew T. Pope, Captain, USAF

AFIT/GMS/ENY/12-M02

DEPARTMENT OF THE AIR FORCE
AIR UNIVERSITY

AIR FORCE INSTITUTE OF TECHNOLOGY

Wright-Patterson Air Force Base, Ohio

AFIT/GMS/ENY/12-M02

CREEP BEHAVIOR IN INTERLAMINAR SHEAR OF A CVI SIC/SIC COMPOSITE AT ELEVATED TEMPERATURE IN AIR AND IN STEAM

THESIS

Presented to the Faculty

Department of Aeronautics and Astronautics

Graduate School of Engineering and Management

Air Force Institute of Technology

Air University

Air Education and Training Command

In Partial Fulfillment of the Requirements for the

Degree of Master of Science in Material Science

Matthew T. Pope, BS

Captain, USAF

March 2012

AFIT/GMS/ENY/12-M02

CREEP BEHAVIOR IN INTERLAMINAR SHEAR OF A CVI SIC/SIC COMPOSITE AT ELEVATED TEMPERATURE IN AIR AND IN STEAM

Matthew T. Pope, B.S.

Captain, USAF

Approved:

_____	_____
Dr. Marina B. Ruggles-Wrenn (Chair)	Date
_____	_____
Geoff Fair, PhD (Member)	Date
_____	_____
Thomas Eason, PhD (Member)	Date

Abstract

The creep behavior in interlaminar shear of a Hi-Nicalon /SiC-B_4C ceramic matrix composite (CMC) was studied at 1200°C in laboratory air and in steam environments. The CMC investigated in this effort consisted of an oxidation-inhibited multilayered matrix reinforced with laminated, woven Hi-Nicalon fibers. Fiber preforms had pyrolytic carbon fiber coating with a boron carbide coat applied. Preforms were then densified with the SiC-B_4C oxidation-inhibited matrix through chemical vapor infiltration (CVI). The interlaminar shear properties were measured. The creep behavior was evaluated for interlaminar shear stresses ranging from -16 to -22 MPa. In air and steam, the composite exhibited both primary and secondary creep. Creep run-out was defined as 100 hours at creep stress. Runout was achieved in both air and in steam at -16 MPa. The presence of steam generally decreased the creep life at the stress levels above -16 MPa. The retained properties of all specimens that achieved run-out were characterized. Composite microstructure as well as damage and failure mechanisms were investigated.

Acknowledgments

I extend my sincerest gratitude first and foremost to Dr. Marina Ruggles-Wrenn. Her tireless guidance, expertise, and fortitude were the cornerstone of my success in these efforts. She always took whatever time was necessary to answer my questions, clarify unclear concepts, and redirect me if I went too far off course. I could not have asked for a better advisor who offered me such an excellent research opportunity.

I am also very grateful for the great help and camaraderie from Mr. Barry Page, Mr. Sean Miller, Mr. Chris Zickefoose, and Mr. Jay Anderson for their instruction, for ensuring that test equipment was functioning properly, and for ensuring that I always had backup parts. To Mr. Brain Crabtree, Mr. Dan Ryan, and Jan: I am thankful for the meticulous work done in machining the test specimens and for always finding a way to meet the timeline of this project.

This awesome team…my advisor, the AFIT lab, and the AFIT machine shop…ensured that my efforts were focused in the right direction and that I ultimately succeeded. This team was always a pleasure to work with and always “made it happen”.

Matthew T. Pope

Table of Contents

Page

List of Figures

List of Tables

CREEP BEHAVIOR IN INTERLAMINAR SHEAR OF A CVI SIC/SIC COMPOSITE AT ELEVATED TEMPERATURE IN AIR AND IN STEAM

I. Introduction

Composite materials consist of chemically or physically distinctive reinforcement phases that are distributed within a continuous phase. A composite combines the properties of its components to achieve the desirable overall properties. Composites are generally classified into three families: polymer matrix composites (PMCs), metal matrix composites (MMCs), and ceramic matrix composites (CMCs) [1]. A CMC containing Silicon Carbide (SiC) is the subject of this thesis.

Modern aero-engine designs require higher performance, lighter weight, lower emissions, lower noise, and lower life cycle costs. These requirements demand increased thrust-to-weight ratios and increased turbine inlet temperatures (TIT) [2]. Figure 1 shows historical trends of TIT in jet engines over the past several years.

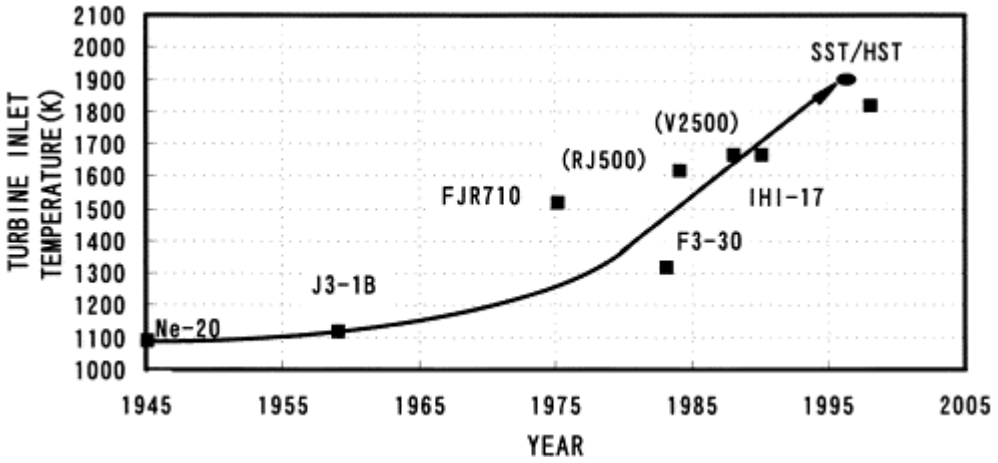

Figure 1 - Trends of TIT in a jet engine [reproduced from 2]

The highest operating temperatures occur at takeoff and during the cruise portion of the mission cycle, and the most severe engine conditions are experienced for hours

instead of just the minutes during takeoff in existing subsonic aircraft. Thus, creep resistance is needed in all hot section components [2] and a thorough understanding of the mechanical behavior of CMCs under all loading regimes is essential before these materials can be widely utilized in aerospace applications.

II. Background

Ceramic Matrix Composites (CMCs)

CMCs directly address the aforementioned aerospace requirements by offering better high-temperature performance than metallic alloys with decreased operating and life cycle costs. CMCs offer lower density than conventional nickel-based alloys while retaining their strength at much higher temperatures. These properties are of primary interest to the aerospace design community. Higher combustion temperatures and decreased cooling air requirements will increase engine thrust while decreasing fuel consumption. Currently, the use of CMCs is being demonstrated in turbine components such as combustor liners, turbine nozzles, shrouds, transition ducts, diffusers, exhaust structures, and several other components. However, many of these CMC demonstration components have shown accelerated degradation of fibers and fiber coatings after minimal operation. This accelerated degradation is primarily driven by oxidative damage from moisture in the operating environment [3].

A CMC consists of a reinforcement (fibers), an interphase, and the matrix. The table below lists specific CMC property goals for aerospace applications as well as the corresponding controlling factors.

Table 1 - Key CMC Properties and Controlling Factors [4]

Key CMC Property Goals **(Importance for CMC engine component)**	**Key Controlling Constituent Factors**
High tensile Proportional Limit Stress (PLS) after CMC processing *(allows high CMC design stress and high environmental resistance)*	Matrix Porosity, Fiber Content
High Ultimate Tensile Strength (UTS) and strain after CMC processing *(allows good CMC toughness and long life after matrix cracking in aggressive environments)*	Fiber Strength, Fiber Content
High UTS retention after interphase exposure at intermediate temperatures in wet oxygen *(allows CMC toughness retention when exposed, uncracked, or cracked, to combustion gases)*	Fiber Coating Composition
High creep resistance at upper use temperature under high tensile stress *(allows long life, dimensional control, low residual CMC stress)*	Matrix Creep, Fiber Creep
Long Rupture life (>500 hours) at upper use temperature under high tensile stress *(allows long-term CMC component service)*	Matrix Rupture, Fiber Rupture
High thermal conductivity at all service temperatures *(reduces thermal stresses due to thermal gradients and thermal shock)*	Fiber-Coating-Matrix Conductivity, Matrix Porosity

Oxide and Non-Oxide CMCs

CMC components can be divided into oxides and non-oxides. Oxides, which are often iterations of Al_2O_3 or Al_2O_3/SiO_2, tend to resist oxidation even at high temperatures [5]. However, oxides have relatively high coefficients of thermal expansion which present tolerance problems in the intended applications where high thermal gradients are the norm. Oxides are also much more prone to creep than non-oxides at lower temperatures. Furthermore even the highest quality oxide fibers lose strength at 1100 °C [5, 6].

Non-oxides such as SiC have lower porosity [5], are typically much stronger, and demonstrate lower creep rates when compared to oxides, even at elevated temperatures. However, SiC is prone to oxidation at elevated temperatures [7] and production of SiC is relatively expensive. Recent research efforts have focused on development of oxide

fibers with increased creep resistance and non-oxide fibers that are less expensive and more oxidation-resistant.

The matrix and fiber coating of the Hi-Nicalon/PyC/HyperSiC in this research were deposited onto the fiber preforms using chemical vapor infiltration (CVI). CVI is advantageous in that it can be used to produce large and fairly complex geometries that exhibit little dimensional change and can be done at relatively low temperatures, minimizing damage to the fiber preforms. It allows deposition of fiber coatings followed by immediate deposition of the matrix phase. This process delivers a matrix with good thermal and mechanical properties because it allows controlled microstructures and deposition of multiple, high-purity matrix layers. However, CVI is very slow and expensive, and requires tight control of temperature, pressure, and gas flow. During CVI, deposition is favored at the locations where the gases first enter the porous body, thus complete filling of all void space is impossible. CVI does not allow a fully densified part and results in 10% porosity at best [9, 18].

Polymer infiltration pyrolysis (PIP), also referred to as liquid polymer infiltration, allows excellent control of matrix composition at relatively low densification temperatures. However, there multiple infiltration and densification cycles required in PIP to obtain a desired density, and the large shrinkage that occurs during the pyrolysis process leads to matrix cracks and porosity [19].

Melt infiltration produces a homogeneous matrix in a single step and generally results in a very low porosity. The resulting matrix is prone to cracking because of a differential between the shrinkage of the matrix and the reinforcement. To minimize this cracking, an excellent match between the coefficient of thermal expansion for the matrix

and reinforcement components must exist. The melt infiltration process also leads to unreacted Silicon deposits throughout the material. These residual, unreacted Silicon deposits degrade the mechanical properties of the material since the melting temperature of Silicon is significantly lower than that of Silicon Carbide [1, 5, 18, 19].

Mechanisms to Increase Fracture Toughness of CMCs

Ceramics primarily posses ionic bonding and some covalent bonding. The intra-atomic transfer of electrons in ionic bonding balances the ionic charges to yield a neutral compound whereas in covalent bonding, there is intra-atomic sharing of electrons. These bond types cause the crystal lattice to resist dislocation motion, and ultimately produce the high strength and brittle behavior that is characteristic of ceramics. At low to moderate temperatures, stress concentrations at a crack tip cannot be relieved by plastic deformation and cracks propagate easily. Therefore, the pursuit of methods to increase the fracture toughness of ceramics must consider concepts other than those relying on dislocation mobility [1].

Since monolithic ceramics are extremely prone to brittle failure under tensile and impact loading, they are not commonly utilized. However, these same ceramics that exhibit brittle behavior and low flaw tolerances can be toughened when used as constituents in a properly designed CMC. Crack deflection in CMCs can be achieved through properly designed fiber-matrix interphases [8, 9]. Specifically, the interphase (sometimes called fiber coating) can facilitate crack deflection and prevent fiber degradation by one or more of the following mechanisms [8, 10]:

1. allowing gradual decoupling of and sliding between the fibers and matrix,

2. preventing interactions between a matrix and fibers that are not in thermodynamic equilibrium,
3. acting as a sacrificial layer that interacts with and neutralizes environmental oxidators/reducers that would otherwise attack the fibers and matrix.

Typical failure mechanisms of a CMC can be correlated to the stress-strain relationship as schematically shown in Figure 2. A strong bond between the fibers and matrix does not allow decoupling of the fibers and matrix. This inability to decouple will allow a matrix crack to propagate through the fibers that are in its path and cause sudden failure of the material. A weaker bond between the matrix and fibers will allow the decoupling of matrix and fiber to permit crack bridging and crack deflection, thus dissipating crack energy and delaying material failure.

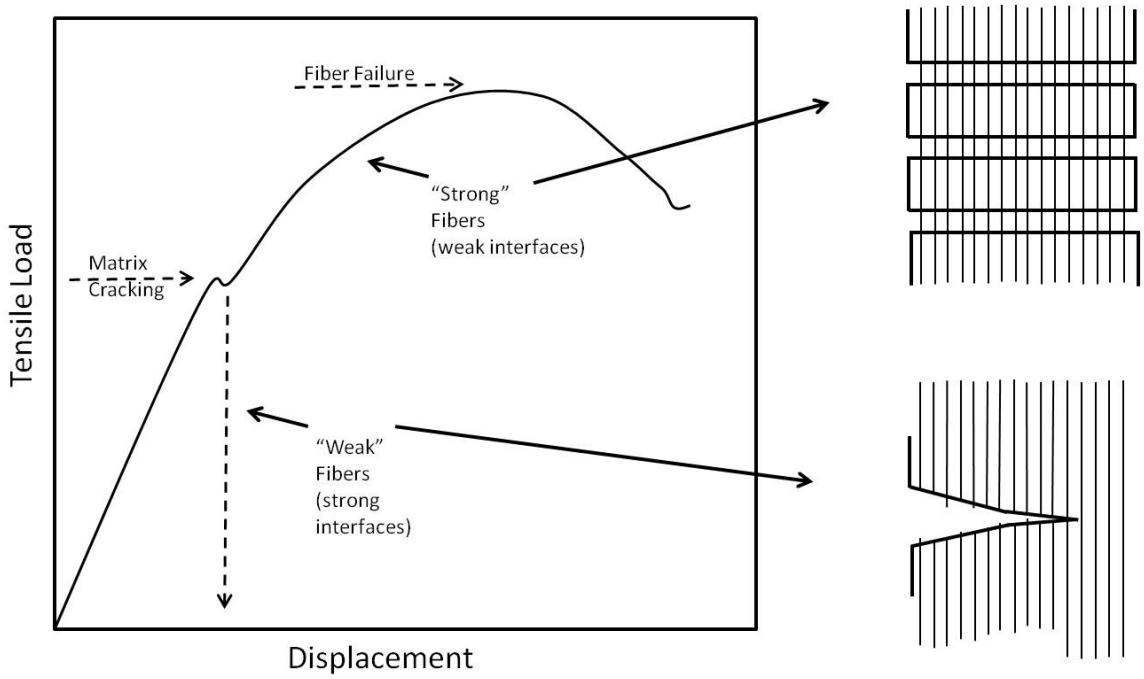

Figure 2 - Tensile stress-strain curve for a "tough" ceramic matrix composite [reproduced from 9]

The strain required for failure of the fibers is often many orders of magnitude greater than the failure strain of the matrix. In harsh operating environments where the strain placed on the matrix causes matrix cracking, the oxidizing environment is allowed to enter the composite through the matrix cracks and to attack both fibers and matrix. The oxidizing environment then degrades the interphase (fiber coating), promoting fiber-matrix bonding, which ultimately causes the material to exhibit the very brittle behavior the designer would like to avoid [9]. Therefore, even when the advantages of both an interphase and weaker bond between the matrix and fibers are present, embrittlement due to oxidation is still a significant problem.

Previous Research on Interlaminar Shear Properties of SiC/SiC CMCs

The vast majority of life-limiting assessments for CMCs and resulting improvements in damage tolerance have been focused on the fiber-dominated properties and mechanical behaviors. However, two-dimensional laminated CMCs are often susceptible to failure in the matrix-rich interlaminar regions because of bending stresses and thermal gradient loads. This interlaminar failure or delamination may ultimately lead to loss of stiffness and accelerate structural failure of the CMC [11, 12].

Several recent studies examined the behavior of CMCs in shear [13-15]. Choi et al [11, 12, 16, 17, 25] evaluated the high-temperature life limiting behavior in interlaminar shear of several non-oxide CMCs. Choi and co-workers established the interlaminar shear strength (ILSS) as a function of loading rate using double-notch shear (DNS) specimens and demonstrated that the ILSS degraded with decreasing loading rate. Choi and co-workers proposed a power-law type crack growth model to account for the

degradation of the ILSS of the composite at elevated temperatures. High-temperature creep tests in interlaminar shear were used to validate the proposed phenomenological model.

The studies performed by Choi and co-workers focused on the non-oxide CMCS with matrix-rich interlaminar regions, where the interlaminar failure is controlled by the fiber-matrix interface. Furthermore, Choi and co-workers performed all high-temperature experiments in laboratory air. In contrast, Laffey [22] investigated behavior of a porous-matrix oxide-oxide CMC, where the interlaminar shear failure is controlled by the exceptionally weak porous matrix. The oxide-oxide CMC consisted of a porous alumina matrix reinforced with the Nextel™720 fibers. Moreover, Laffey evaluated the ILSS and assessed the creep behavior in interlaminar shear of the Nextel™720/alumina composite at 1200 °C in air and in steam environments. The presence of steam drastically reduced creep lifetimes.

Thesis Objective

The objective of this thesis research is to evaluate the ILSS and to investigate the creep behavior in interlaminar shear of a ceramic composite comprised of Hi-Nicalon™ fibers, pyrolytic carbon fiber coating with boron carbide overlay, and a SiC-based multilayered matrix. The oxidation-inhibited self-healing matrix consists of alternating layers of SiC and B_4C. The composite is processed via chemical vapor infiltration (CVI). This study investigates creep behavior of the Hi-Nicalon™/SiC-B_4C composite in interlaminar shear at 1200 °C in air and in steam environments. The composite microstructure, as well as damage and failure mechanisms are discussed.

III. Test Material and Specimen Geometry

Hi-Nicalon™/SiC-B_4C Ceramic Composite

The Hi-Nicalon™/SiC-B_4C (Hi-N/SiC-B_4C) ceramic composite that is the subject of this research was manufactured by Hyper-Therm High-Temperature Composites, Inc. (Huntington Beach, CA). The composite was reinforced with Hi-Nicalon™ fibers woven in a five-harness satin weave, and was processed by CVI. The self-healing matrix has alternating layers of silicon carbide and boron carbide. Laminated fiber preforms were produced from 18 plies of woven fabric in a 0°/90° layup symmetric about mid-plane with warp and fill plies alternated. Before the infiltration, the preforms were coated with pyrolytic carbon fiber coating (~0.40 μm thick) with boron carbide overlay (~1.0 μm thick) to decrease bonding between the fibers and the matrix. The composite had an average finished fiber volume of approximately 36.4% and an average density of ~2.40 g/cm^3. All specimens were cut from two 5.0 mm thick panels and sealed with a CVI SiC overcoat after machining. The overall microstructure of the CMC is displayed in Fig. 15, which shows the oxidation inhibited matrix consisting of alternating layers of SiC and B_4C as well as 0° fibers, PyC fiber coating and B_4C overlay.

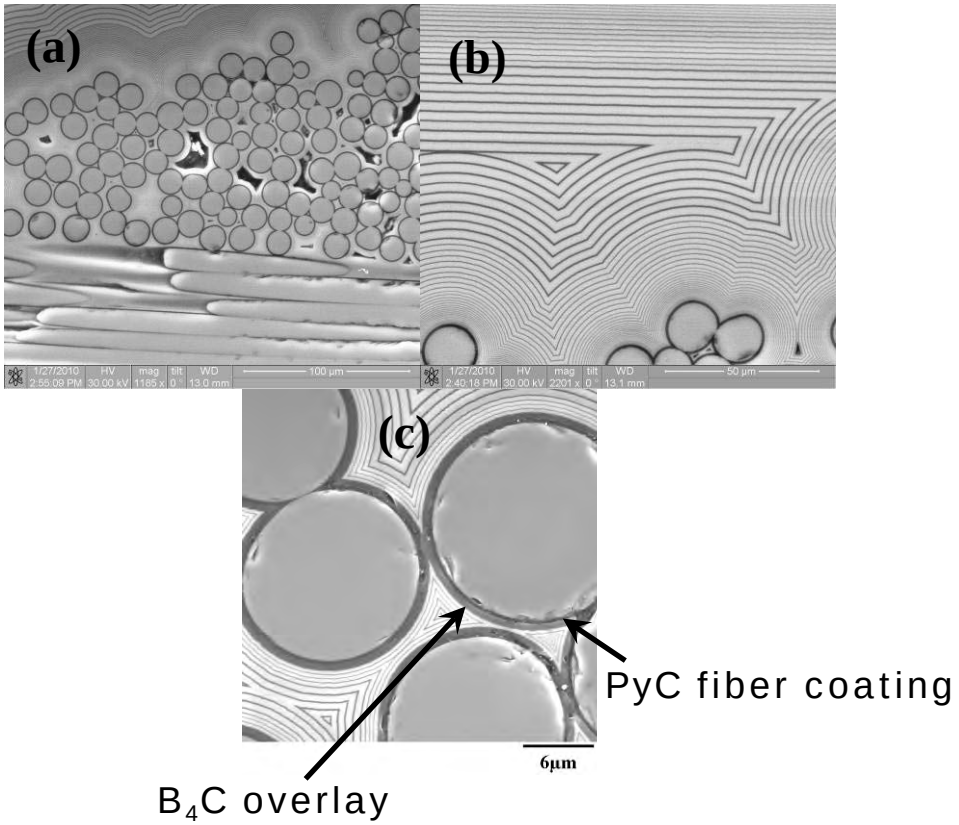

Figure 3 - SEM micrographs showing: (a) typical microstructure of Hi-Nicalon™/SiC-B_4C ceramic composite, (b) oxidation inhibited matrix consisting of alternating layers of SiC and B_4C, (c) fibers and PyC fiber coating with B_4C overlay [15]

Self-Healing SiC-B_4C Matrix

Matrix material selection is driven by thermal properties and processing considerations [18]. SiC is an excellent candidate for high-temperature aerospace applications because it has stable mechanical properties at high-temperatures. However, when used as a matrix material in SiC/SiC composites, SiC experiences extensive microcracking when subjected to relatively low tensile stresses (100-200 MPa). When the composite is exposed to an oxidizing environment at elevated temperatures, these matrix microcracks promote the diffusion of oxygen into the composite interior and towards the oxidation-prone interphases and fibers. The objective of the material processing is to design the SiC matrix so as to slow down the oxygen diffusion into the CMC and to improve the composite oxidation resistance and durability in the oxidizing environments. One of the material design philosophies is to introduce elements that can form fluid oxide phases at elevated temperature into the SiC matrix. Once exposed to a wide temperature range, such elements (for example boron) would form a fluid oxide phase, which in turn would fill the matrix cracks, thus rendering the matrix self-healing. Boron oxide phases can form at relatively low temperatures (500-1000 °C) according to:

$$B_4C_{(s)} + 4O_{2(g)} \rightarrow 2B_2O_{3(s,l)} + CO_{2(g)}$$

At intermediate temperatures, both SiC and B_4C oxidize, producing a SiO_2- B_2O_3 viscous phase. One possible way to introduce a B-bearing phase into a SiC matrix is to build a multilayered matrix, consisting of alternating layers of SiC and B_4C. In the case of the Hi-N/SiC-B_4C composite studied in this research effort, a multilayered SiC-based matrix includes concentric layers of the crack-arresting B_4C around groups of fibers. At 1200°C in air and in steam, both SiC and B_4C would oxidize yielding fluid glassy phases, which

can fill the matrix cracks as soon as they are initiated, thus inhibiting the diffusion of oxygen along crack paths and increasing the oxidation resistance and durability of the composite.

Hi-Nicalon Fiber Reinforcement

Hi-Nicalon™ fibers are the SiC-based fibers of the second generation. The development of the Hi-Nicalon fibers followed the development of the early SiC-based fibers such as Nicalon. It was recognized that the SiC-based fibers of the first generation were not pure SiC, but consisted of SiC-nanocrystals (1-2 nm in size) and free carbon embedded in an amorphous SiC_xO_y matrix. Consequently, the stiffness of the Nicalon fibers (E = 220 GPa) was considerably below that of the pure SiC ($E \approx 400$ GPa), while their failure strain was relatively high ($\varepsilon_f = 1.4\%$). Still most importantly, the Nicalon fibers exhibited dramatic loss of strength at temperatures exceeding 1100-1200 °C. In fact, the Nicalon fibers decomposed at temperatures beyond 1100-1200 °C. Therefore, the use of these fibers was limited to composites that could be processed at lower temperatures and then employed at lower temperatures.

Hi-Nicalon are oxygen-free fibers, which consist of a mixture of SiC-nanocrystals (~0.5 nm in size) and free carbon. These fibers do not decompose at higher temperatures because they do not contain an appreciable amount of the SiC_xO_y phase. The Hi-Nicalon fibers exhibit creep at temperatures near 1200 °C, but their creep resistance increases with heat treatment at 1400-1600 °C, which serves to stabilize their microstructure. The reduction in oxygen also produced the Hi-Nicalon fibers that are approximately 35% stiffer than the first generation Nicalon fibers. Hi-Nicalon fibers also exhibit improved strength retention at high temperatures compared to the first generation SiC-based fibers

[19]. Table 2 compares properties of Hi-Nicalon fibers with those of other ceramic fibers.

Table 2 - Properties of Hi-Nicalon fiber reinforcement versus other common ceramics [18]

Fiber	*Composition*	*Tensile Strength (ksi)*	*Tensile Modulus (msi)*	*Density (g/cm^3)*	*Diameter (mil)*	*Critical Bend Radii (mm)*
SCS-6	SiC on C Monofilament	620	62	3.00	5.5	7.0
Nextel 312	$62Al_2O_3$-$14B_2O_3$-$15SiO_2$	250	22	2.7	0.4	0.48
Nextel 440	$70Al_2O_3$-$2B_2O_3$-$28SiO_2$	300	27	3.05	0.4–0.5	–
Nextel 480	$70Al_2O_3$-$2B_2O_3$-$28SiO_2$	330	32	3.05	0.4–0.5	–
Nextel 550	$73Al_2O_3$-$27SiO_2$	290	28	3.03	0.4–0.5	0.48
Nextel 610	99 α-Al_2O_3	425	54	3.88	0.6	–
Nextel 720	$85Al_2O_3$-$15SiO_2$	300	38	3.4	0.4–0.5	–
Almax	99 α-Al_2O_3	260	30	3.60	0.4	–
Altex	$85Al_2O_3$-$15SiO_2$	290	28	3.20	0.6	0.53
Nicalon NL200	57Si-31C-12O	435	32	2.55	0.6	0.36
Hi-Nicalon	62Si-32C-0.5O	400	39	2.74	0.6	–
Hi-Nicalon-S	68.9Si-30.9C-0.2O	375	61	3.10	0.5	–
Tyranno LOX M	55.4Si-32.4C-10.2O-2Ti	480	27	2.48	0.4	0.27
Tyranno ZM	55.3Si-33.9C-9.8O-1Zr	480	28	2.48	0.4	–
Sylramic	66.6Si-28.5C-2.3B-2.1Ti-0.8O-0.4N	465	55	3.00	0.4	–
Tonen Si_3N_4	58Si-37N-4O	360	36	2.50	0.4	0.80

Interphase Material

As described earlier in the thesis, the interphase will allowing gradual decoupling of and sliding between the fibers and matrix, prevent detrimental interactions between matrix and fiber, and act as a sacrificial layer that interacts with and neutralizes environmental oxidators/reducers while sparing fibers and matrix [8, 10]. The interphase used in the CMC for this research effort, boron carbide, is also used in the layered matrix where it forms a flowing glassy phase that facilitates a self-healing matrix.

Specimen Geometry

Specimen geometry for this effort was based on ASTM Standard C1425-05. A drawing for this specimen and experiment-specific dimensions are given in the figure and table below.

The double-notch shear (DNS) test specimens measuring 150 mm x 20 mm were

used in all tests. The thickness of the specimens was the same as the nominal thickness of the composite panels, i. e. ~5.0 mm. The notches of 0.5-mm width were extended to the middle of each test specimen within ±0.05 mm so that shear failure occurred on the plane between the notch tips. The distance between the notches was 13 mm. Schematic of the DNS specimen and notch details are shown in Figs. 4 and 5, respectively. Note that dimensions of the DNS specimens used in this study were different from those recommended in the ASTM Standard C1425. The 13-mm distance between the notches was chosen specifically to enable the measurement of compressive strain between the notch tips with an MTS high-temperature extensometer of 12.5-mm gage length. The overall specimen length of 150 mm ensures that the local stress fields at the notch tips are not influenced by the external loading at the specimen ends due to gripping.

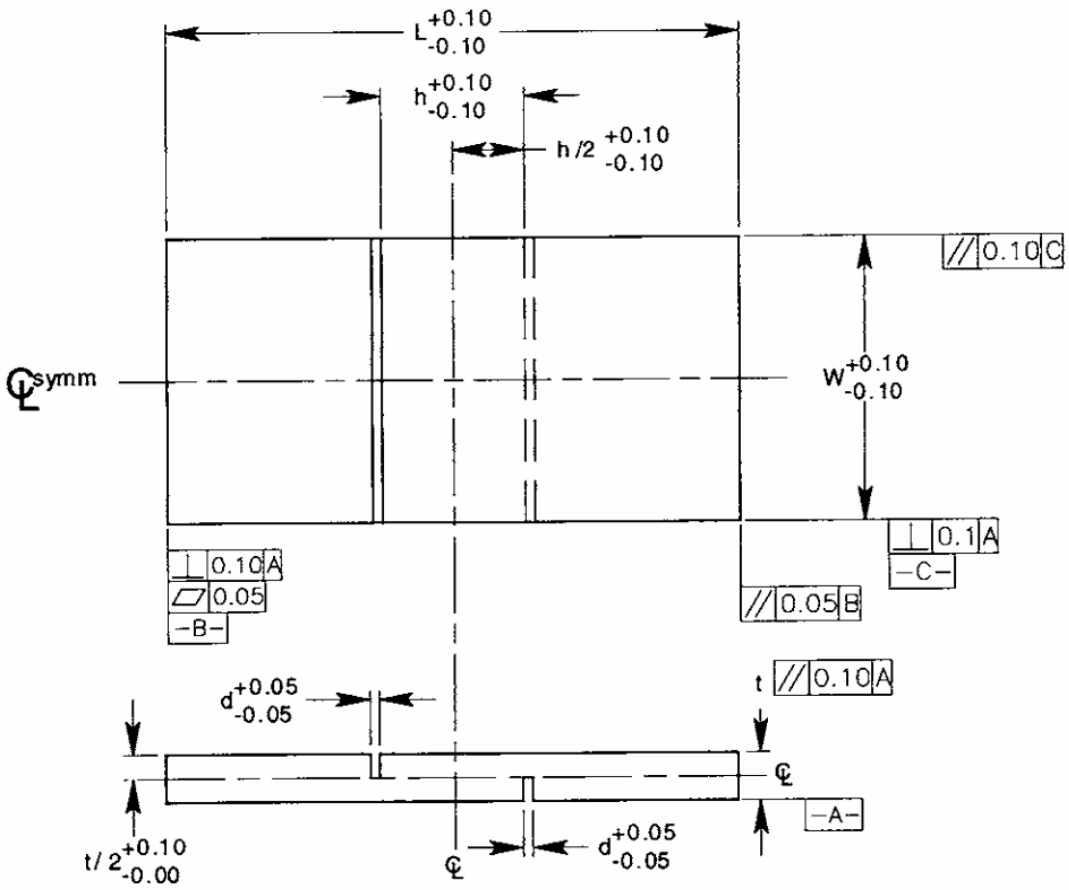

Dimensions	Value (mm)
L	150.00
h	12.00
W	20.00
d	0.50
t/2	2.50

Figure 4 - Double-notch shear (DNS) test specimen (dimensions in mm) [14]

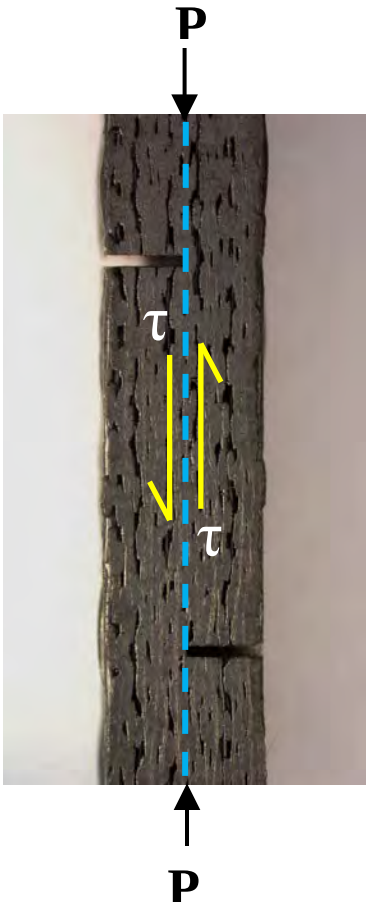

Figure 5 - Double-notch shear (DNS) test specimen, notch details

IV. Experimental Setup and Procedures

Standard Test Method for Interlaminar Shear Strength of CMCs

The test method described in ASTM Standard C1425 [20] is used to determine the ILSS of continuous fiber-reinforced ceramic composites at elevated temperatures by compression of a double notched specimen (DNS) [20]. The compression test of the DNS forces failure to occur along the specimen midplane. The DNS compression test has advantages over the four-point flexural method and the Iosipescu tests. The compression test of the DNS assures that failure of the specimen by interlaminar shear occurs consistently. The notching to the midplane ensures that the entire load is transmitted by shear forces, forcing failure through the matrix-rich region that lies between the notches. The specimen geometry and setup are also simple and less expensive. Furthermore, the DNS method also delivers the most conservative value of ILSS [21]. A schematic of the DNS specimen is given in Figure 6.

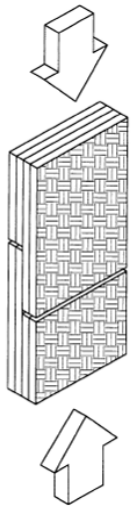

Figure 6 - Schematic of compression of double-notched specimen [20]

Experimental Setup

Mechanical Test Equipment

A servocontrolled MTS 810 mechanical testing machine of 5 kip capacity was used in all tests.

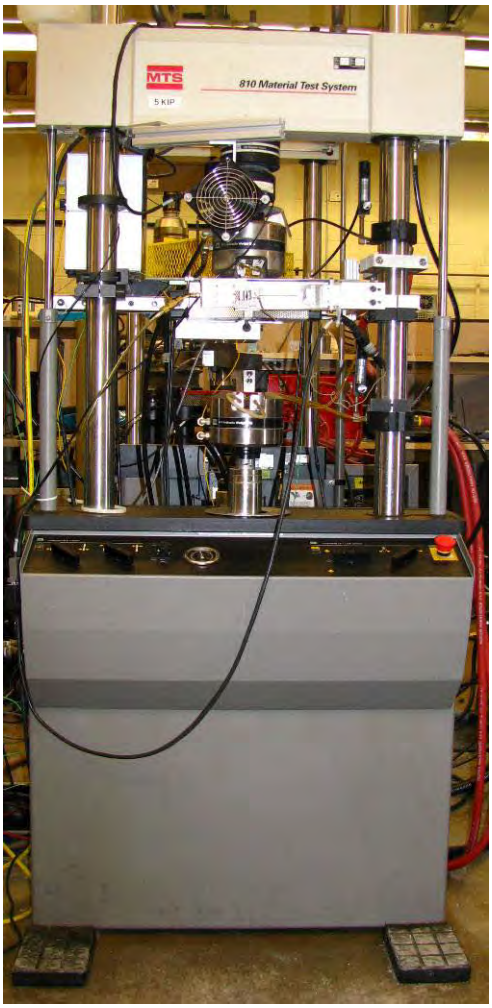

Figure 7 - MTS 810 5 kip testing system

The specimens were gripped at both ends with MTS series 647 hydraulic water-cooled wedge grips. The wedges were coated with Surfalloy to prevent specimen slipping. A Neslab model HX-75 chiller circulated 15°C deionized water to cool the wedge grips. An MTS Model 632.53 E-14 uniaxial low-contact force, high-temperature

extensometer fitted with two 6-in alumina extension rods was used for strain measurement. An MTS Force Transducer (Model 661.19E-04, range: -5,500 lb. to +5,500 lb.) measured the force. Displacement was measured internal to the MTS system.

Environmental Test Equipment

An AMTECO Hot Rail two-zone furnace system and two MTS 409.83 Temperature Controllers were used in all high-temperature tests.

Figure 8 - MTS 409.83 Temperature Controller

The two-zone furnace employed two R-type non-contacting thermocouples to measure the temperature inside the furnace. For testing at high temperature, a specimen was instrumented with R-type thermocouples in order to calibrate the furnace on a periodic basis. An Omega HH501BR thermometer (see Fig. 9) was employed to read the temperature measurements from thermocouples attached to the specimen. The furnace controllers (using non-contacting R-type thermocouples exposed to the ambient

environment near the test specimen) were adjusted to determine the settings needed to achieve the desired temperature of the test specimen. The determined settings were then used in actual tests. The controller settings for testing in steam were determined by placing the specimen instrumented with thermocouples in steam and repeating the furnace calibration procedure. Note that the calibration procedure was repeated each time furnace elements were replaced.

Figure 9 - Omega HH501BR thermometer

The top and bottom exterior surfaces of the furnace were insulated with the Rescor ceramic blanket (rated up to 3000 °F) in order to minimize the heat loss. Care should be taken to remove Rescor insulation prior to ungripping the specimen in order to avoid damaging the furnace. Since ungripping displaces the both the top and bottom grip cylinders towards the furnace, if insulation is in place during ungripping, displacement may compress and destroy the furnace. Figure 10 shows a test in progress with the insulation in place.

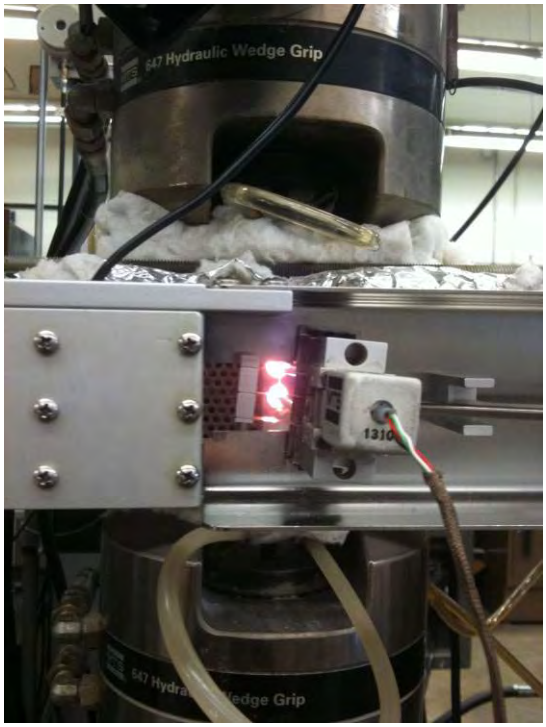

Figure 10 - Front view of test in progress with insulation in place

Tests in steam environment employed an alumina susceptor (tube with end caps), which fits inside the furnace. The specimen gage section is located inside the susceptor, with the ends of the specimen passing through slots in the susceptor. Steam enters the susceptor through a feeding tube in a continuous stream with a slightly positive pressure, expelling the dry air and creating a near 100% steam environment inside the susceptor. The two holes on the front of the susceptor allowed entry of the extensometer rods that were used to measure strain. For procedural consistency, the susceptor was also used in experiments performed in laboratory air. Figure 11 shows the alumina

susceptor.

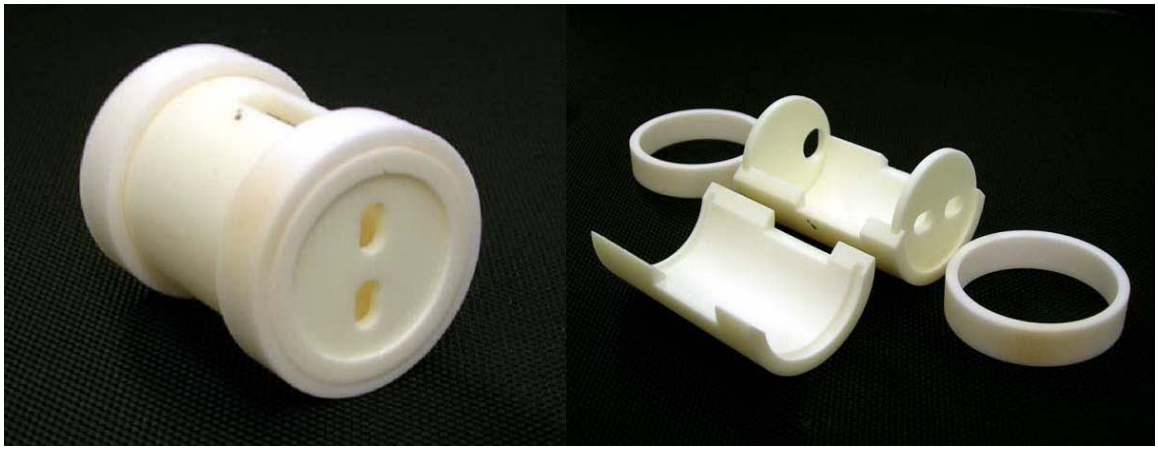

Figure 11 - Ceramic susceptor [22]

Figure 12 below shows the ceramic extensometer contact rods and the ceramic susceptor inside the furnace with the upper half of the failed specimen still gripped at the end of the test.

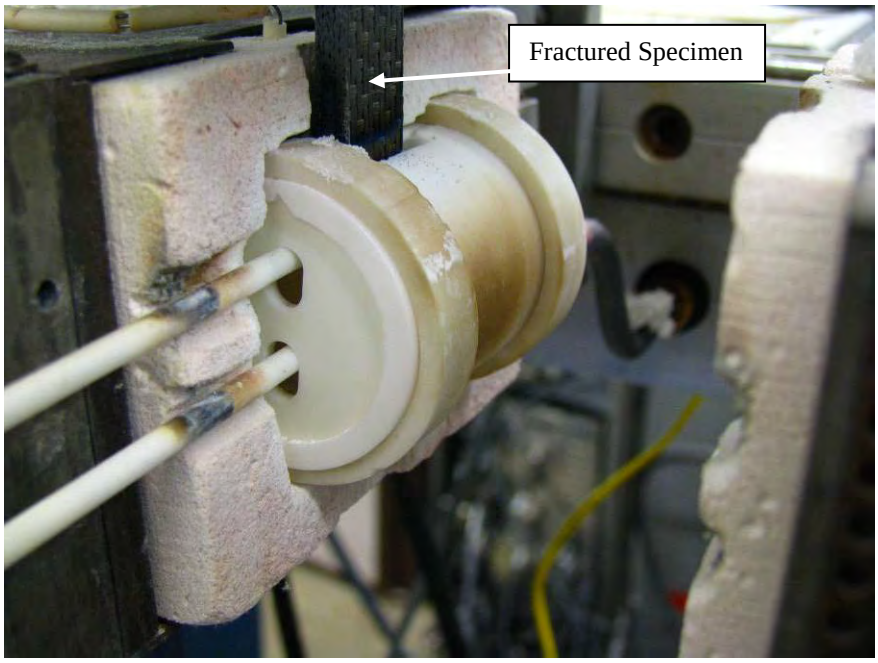

Figure 12 - Open furnace, post-test

An Amteco Chromalox 2110 Steam Generator supplied with deionized water was used to produce steam during tests conducted in steam environment. The steam generator and the feeding tube that delivers steam into the susceptor are shown in Figures 13 and 14, respectively.

Figure 13 - Chromalox Steam Generator

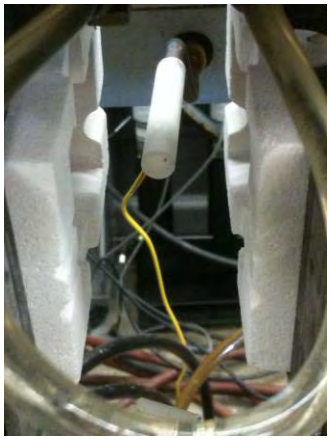

Figure 14 - Steam feed tube without susceptor in place

Test Procedures

Mechanical Testing – MPT Procedures

An MTS Flex Test 40 digital controller was used for input signal generation and data collection. The MPT procedures used in this research were similar to those used by Mehrman, Siegert, and Laffey [22-24]. Laffey noted that the experiment had to be stopped instantaneously when failure occurred in compression, otherwise the fracture surfaces would be destroyed. The procedures used here monitored the load and shut off the hydraulics when the error between load command and load feedback exceeded the

failure detection parameters given in Figure 15. Creep runout was defined as 100 h at creep stress. The retained properties of all specimens that achieved run-out were characterized. The same failure detector that was previously used for monitoring failure during creep was used to detect failure during the test for retained properties.

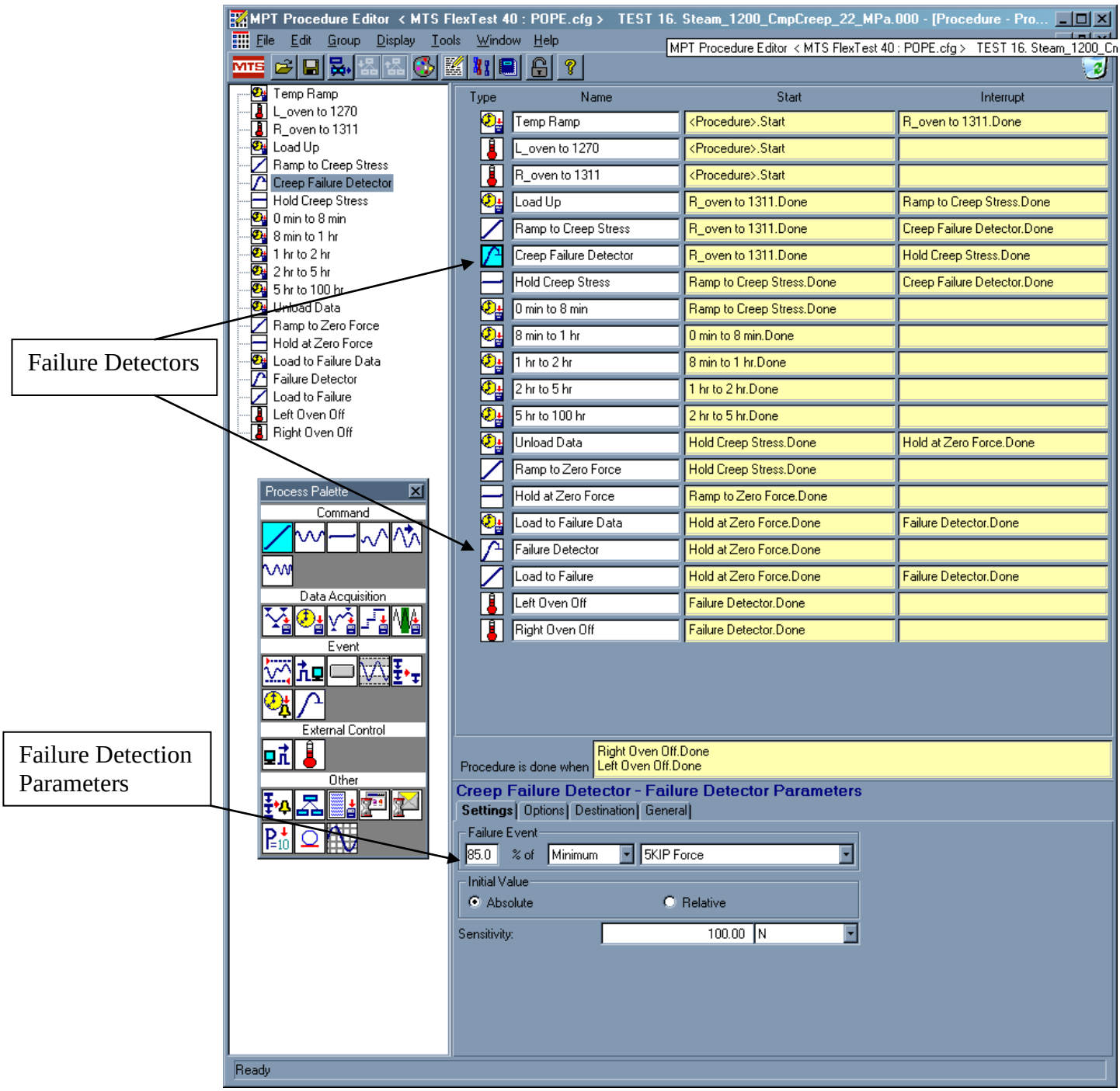

Figure 15 - MTS procedure showing failure detectors

Mechanical Testing – Specimen and Testing Machine Preparation

In order to achieve the desired stress levels for experiments, the effective area of the specimen was calculated using the following equation:

$$\sigma = \frac{P}{Wh}$$

where *W* and *h* represent the specimen *width* and *distance between the notches* respectively, and *P* is the applied *force*. A Mitsutoyo Corporation Digital Micrometer (Model NTD12-6"C) was used to measure the width of specimens and the distance between the notches in order to calculate the effective area where interlaminar shear would cause failure in accordance with ASTM standard C1425-05. Measurements were taken three times, and then averaged. The individual measurements for each specimen are found in the Table 3 below.

Table 3 –Specimen Dimensions

Plate ID	Specimen #	Width, W (mm)	Length, L (mm)	Thickness, t (mm)	Distance Between Notches, h (mm)	Notch Depth, t/2 (mm)
10C362-2	3	15.10	152.49	5.25	12.16	2.63
10C362-2	5	15.01	152.34	5.27	12.06	2.64
10C362-2	6	15.06	152.32	5.24	12.13	2.62
10C362-6	3	14.96	152.49	5.21	12.22	2.61
10C362-6	4	15.02	152.49	5.20	12.21	2.60
10C362-8	1	14.95	152.46	5.30	11.68	2.65
10C362-8	4	15.01	152.42	5.25	11.70	2.63
10C362-8	5	14.92	152.40	5.38	11.82	2.69
10C362-9	1	14.95	152.49	5.33	12.14	2.67
10C362-9	2	14.96	152.38	5.27	12.29	2.64
10C362-9	3	15.09	152.47	5.31	12.42	2.66
10C362-9	4	15.06	152.43	5.21	11.97	2.61

Prior to testing, the specimen was prepared for gripping. Specimen tabs were attached to the specimen before gripping in the top grips. Adhesive was not used to directly attach the tabs to the specimen because previous research efforts showed this allowed slipping in the MTS grips. Rather, aluminum tabs were attached to the specimen at both ends using a very small strip of tape. The tape at the top end of the specimen remained in place to ensure that the tabs were aligned with the specimen-grip interface as the top grips were engaged. Tape used at the bottom end of the specimen was removed once the specimen was gripped. The gripping pressure was 10 MPa. Figure 16 shows the aluminum tabs in place on the top end of a test specimen.

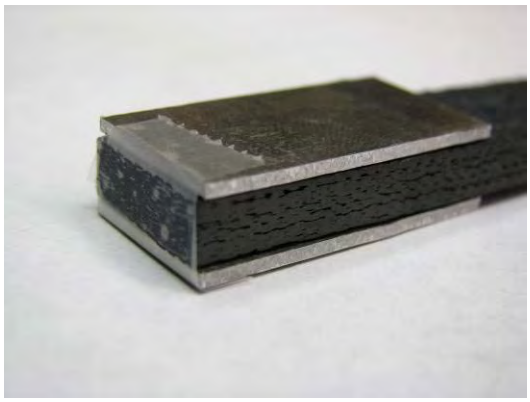

Figure 16 - Aluminum specimen tabs

With tabs in place, specimens were gripped in the top grip first while in displacement mode. A level was used during gripping to ensure the specimen axis was positioned parallel to the loading direction and position was verified yet again after gripping was accomplished. Once the top of the specimen was gripped, the susceptor was placed around the specimen and the furnace was closed around the susceptor. Proper position of the susceptor entry holes for both the extensometer rods and steam feeding

tube relative to the holes in the furnace was carefully verified upon closing of the furnace. In the case of the experiments conducted in air, the susceptor entry hole for the steam feeding tube was closed off with Rescor insulation to minimize heat loss from the furnace. Before gripping the bottom of the specimen, control was switched from displacement to force. Then the force command was set to zero and the bottom of the specimen was then promptly gripped. Finally the insulation was installed both above and below the oven.

The extensometer rod contact positions on the specimen relative to the specimen notches were carefully chosen. The 13-mm distance between specimen notches was selected specifically to enable the measurement of compressive strain between the notch tips with an MTS high-temperature extensometer of 12.5-mm gage length. For strain measurement, the extensometer rods were placed as close to the notch tips of the specimen as possible (see Fig. 17).

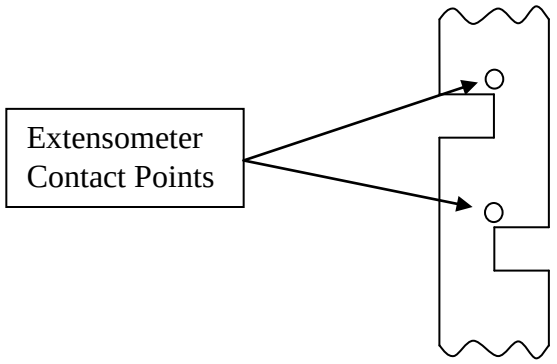

Figure 17 - Locations of extensometer rod tips

In all tests, a specimen was heated to 1200 °C at 1°C/s, and held at 1200 °C for additional 30 min prior to testing. The same procedures were used for testing in air and in steam. Data collection during different parts of each test was accomplished at different rates as shown in Table 4.

Table 4 - Data sampling rates

Test Event	**Data Collection Rate**
Heat Up	2 sec
Load Up	25 Hz
0 to 8 min	4 Hz
8 min to 60 min	3 Hz
1 hr to 2 hr	1 Hz
2 hr to 5 hr	0.33 Hz
5 hr to 100 hr	2 min
Unload	10 Hz
Load to Failure	25 Hz

When a specimen failed at the end of the experiment, the testing system was immediately shut off and the bottom half of the failed specimen was promptly removed from the furnace. Thus the interior of the fracture surface of the bottom half of the failed specimen was exposed to significant temperatures and prolonged oxidation for a few minutes at most. The bottom half of the specimen was labeled and prepared for further analysis and examination with the SEM.

Microstructural Characterization

Fractured specimens were cut using a diamond-tipped saw blade at the AFIT machine shop. No coolant fluid was used during cutting in order not to contaminate the fracture surfaces. The fracture surfaces of test specimens were examined with a Zeiss Stemi SV II optical microscope equipped with a Zeiss AxioCam HRc digital camera and

the Quanta 200 scanning electron microscope (SEM). Since the test material is conductive, no coatings were necessary for the SEM analysis.

V. Results and Discussion

The results of the experimental investigation are presented in this chapter. A summary of all tests is given in Table 5. Because the test specimens were cut from several panels, the specimen numbers contain reference to the composite panel. For example, number P8-1 refers to the specimen 1 from panel 8.

Table 5 - Summary of Experiments

Specimen	Test Type	Test Environment	ABS Stress Level (MPa)	Time to Rupture (hours)	ABS Failure Strain (%)
P6-3	Compression to Failure	Air	27.6	-	0.154
P8-1	Compression to Failure	Air	27.3	-	0.115
P2-3	Compression to Failure	Air	27.0	-	0.172
P6-4	Compression to Failure	Air	26.8	-	0.153
P6-4	Creep in Interlaminar Shear	Air	16.0	100.0	0.107
P9-2	Creep in Interlaminar Shear	Air	18.0	83.0	0.145
P8-4	Creep in Interlaminar Shear	Air	20.0	26.3	0.121
P2-6	Creep in Interlaminar Shear	Air	22.0	6.1	0.084
P2-5	Creep in Interlaminar Shear	Steam	16.0	100.0	0.169
P8-5	Creep in Interlaminar Shear	Steam	18.0	73.0	0.178
P9-3	Creep in Interlaminar Shear	Steam	20.0	18.9	0.248
P9-4	Creep in Interlaminar Shear	Steam	22.0	14.0	0.253

Coefficient of Thermal Expansion

In each high-temperature test, strain was recorded during the heat up to test temperature of 1200 °C. As no mechanical loading was yet applied, the recorded strain represents thermal expansion only and thus permits us to determine the linear thermal expansion coefficient of the material. The coefficient of linear thermal expansion (CTE) was calculated for each specimen using the following formula:

$$\alpha = \frac{\varepsilon_t}{\Delta T}$$

where ε_t is the experimentally measured thermal strain (m/m) and ΔT is the temperature change in °C of the test specimen during heat up. Thermal expansion results are summarized in Table 6, where thermal strain and coefficient of linear thermal expansion are presented for each specimens tested. Note that the CTE was 0.262 x 10^{-6}/°C higher on average in steam than in air.

Table 6 - Thermal strains produced by Hi-Nicalon/PyC/HyperSiC due to temperature rise

Specimen	Thermal Strain (%)	Coefficient of Linear Thermal Expansion, α (10^{-6}/°C)
P2-5	0.57	4.86
P2-6	0.54	4.55
Average:	*0.55*	*4.70*
Standard Deviation:	*0.03*	*0.22*
P6-3	0.47	4.03
P6-4	0.54	4.57
P6-4	0.52	4.42
Average:	*0.51*	*4.34*
Standard Deviation:	*0.03*	*0.28*
P8-1	0.48	4.12
P8-4	0.53	4.53
P8-5	0.55	4.67
Average:	*0.52*	*4.44*
Standard Deviation:	*0.03*	*0.28*
P9-2	0.51	4.31
P9-3	0.60	5.09
P9-4	0.46	3.89
Average:	*0.52*	*4.43*
Standard Deviation:	*0.07*	*0.61*

Interlaminar Shear Strength

ILSS was assessed in monotonic compression to failure tests performed in stress control with the stress rate of 11.6 MPa/s. Elapsed time, strain, displacement, force commanded, force feedback, and furnace temperatures were recorded during each test. The monotonic stress-strain response is presented in Fig. 18. The shear stress-compressive strain curves are nearly linear to failure. Test results are summarized in Table 7, where the ILSS and compressive failure strain values are presented for each test specimen. In air, the average ILSS was 27.2 MPa. Note that Choi et al [11, 25] reported similar ILSS values (19-31 MPa) for a 2-D woven Hi-Nicalon/SiC composite at 1316 °C.

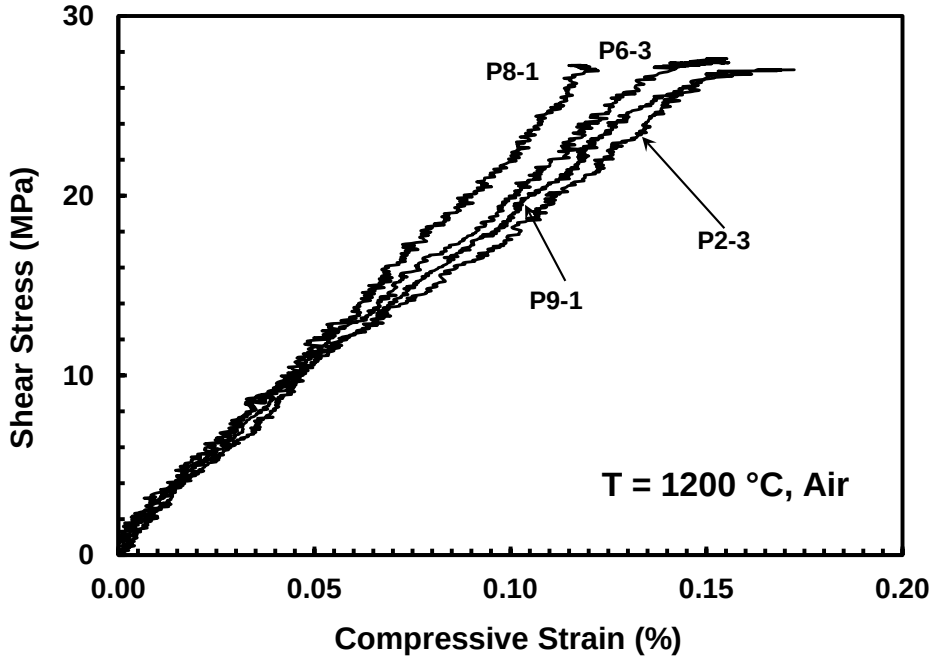

Figure 18 – Compression to failure stress-strain curves for Hi-Nicalon/PyC/HyperSiC Ceramic composite at 1200°C in Air

Table 7 - Compressive properties obtained for Hi-Nicalon/PyC/HyperSiC at 1200°C in Air

Specimen	ILS (MPa)	Compressive Failure Strain (%)
P6-3	27.6	0.154
P8-1	27.3	0.115
P2-3	27.0	0.172
P9-1	26.8	0.153
Average:	*27.2*	*0.149*

Creep Rupture Tests in Air at 1200°C in Laboratory Air

At 1200 °C in air compressive creep tests were performed at the stress levels of 16, 18, 20 and 22 MPa. Results of the creep-rupture tests are summarized in Table 8, where rupture time and creep strain accumulation are shown for each applied shear stress level. Creep strain vs. time curves obtained at 1200 °C in air are shown in Fig. 19.

All creep vs. time curves obtained in air exhibit primary and secondary creep regimes, but no tertiary creep regime. In air, creep run-out of 100 h is achieved at the shear stress of 16 MPa (58.8% ILSS). The strains accumulated during all creep tests conducted at 1200 °C in air are comparable to those obtained in the monotonic test.

Table 8 - Results of creep-rupture tests in interlaminar shear for Hi-Nicalon/PyC/HyperSiC Ceramic Composite at 1200°C in laboratory air

Specimen	Creep Stress (MPa)	Time to Rupture (h)	Creep Strain (%)
P6-4	16.0	100	0.11
P9-2	18.0	83.0	0.15
P8-4	20.0	26.3	0.12
P2-6	22.0	6.10	0.08

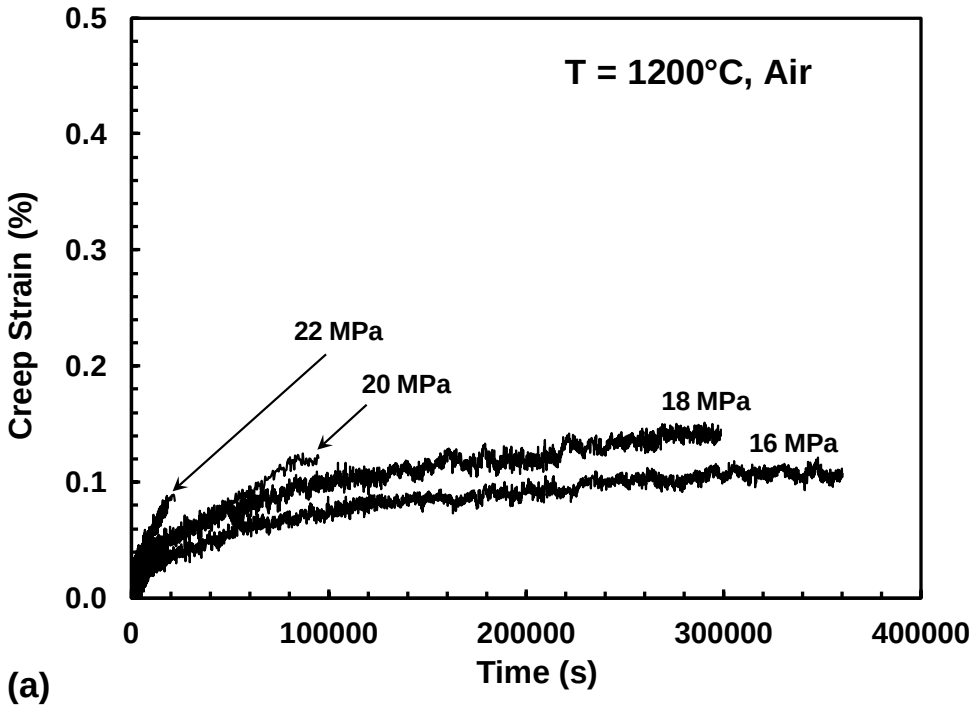

Figure 19 - ABS Creep Strain vs. Time curves for interlaminar shear creep tests on Hi-Nicalon/SiC-B4C Hi-Nicalon/PyC/HyperSiC Ceramic composite obtained at applied interlaminar shear stresses in the 16-22 MPa range at 1200 °C in air at 1200°C

Creep Rupture Tests in Steam at 1200°C

Results of the creep-rupture tests performed at 1200 °C in steam are summarized in Table 9, where results of the creep-rupture tests performed at 1200 °C in air are included for comparison. Creep strain vs. time curves obtained at 1200 °C in steam are shown in Fig. 31. Additionally the creep curves produced at 1200 °C in steam are compared to those obtained at 1200 °C in air in Fig. 20.

As was the case at 1200 °C in air, all creep vs. time curves obtained in steam exhibit primary and secondary creep, but no tertiary creep regime. In steam as in air, creep run-out of 100 h was achieved at the shear stress of 16 MPa (58.8% ILSS). The strains accumulated during 100 h at 16 MPa in steam were also comparable to those

obtained in the monotonic test. However, the strains accumulated at 20 and 22 MPa in steam considerably exceeded the strains produced in the monotonic tests.

Table 9- Results of creep-rupture tests in interlaminar shear for Hi-Nicalon/PyC/HyperSiC Ceramic Composite at 1200°C in laboratory air and in steam

Specimen	Creep Stress (MPa)	Time to Rupture (h)	Creep Strain (%)
Laboratory Air			
P6-4	16.0	100 [a]	0.11
P9-2	18.0	83.0	0.15
P8-4	20.0	26.3	0.12
P2-6	22.0	6.1	0.08
Steam			
P2-5	16.0	100 [a]	0.17
P8-5	18.0	73.0	0.18
P9-3	20.0	18.9	0.25
P9-4	22.0	14.0	0.25

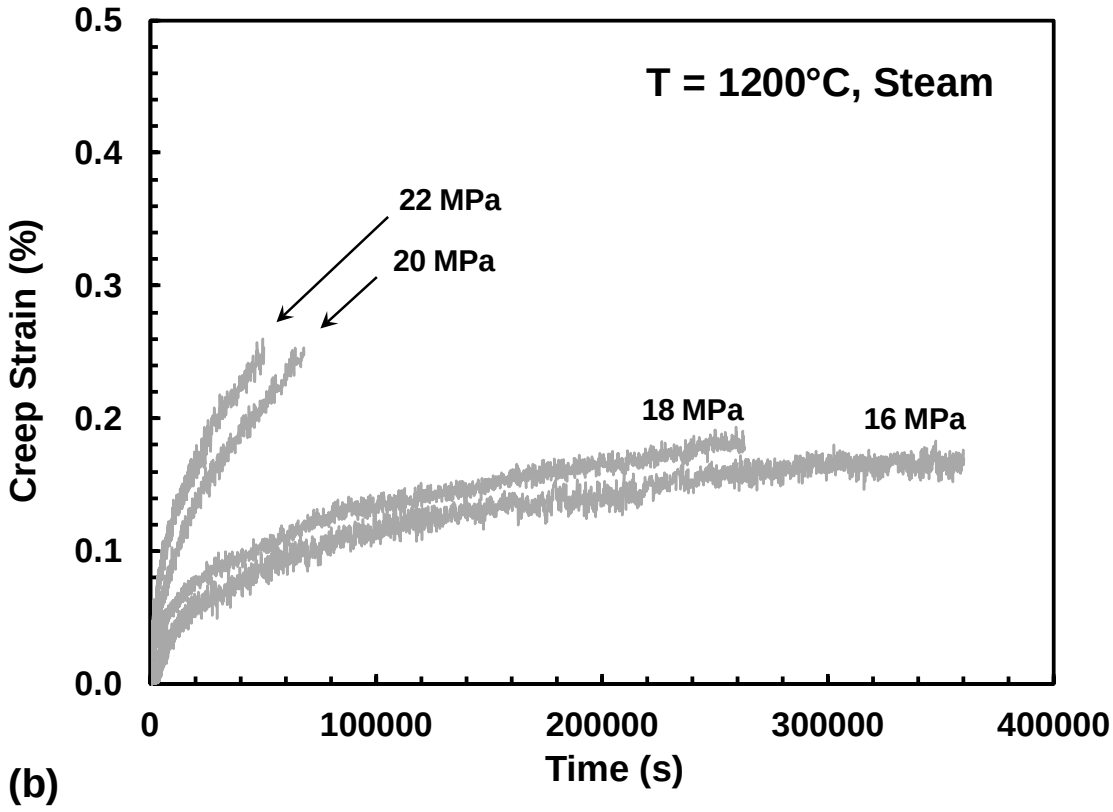

Figure 20 - - Creep strain vs. time curves for Hi-Nicalon/PyC/HyperSiC Ceramic Composite obtained at applied interlaminar shear stresses in the 16-22 MPa range at 1200 °C in steam

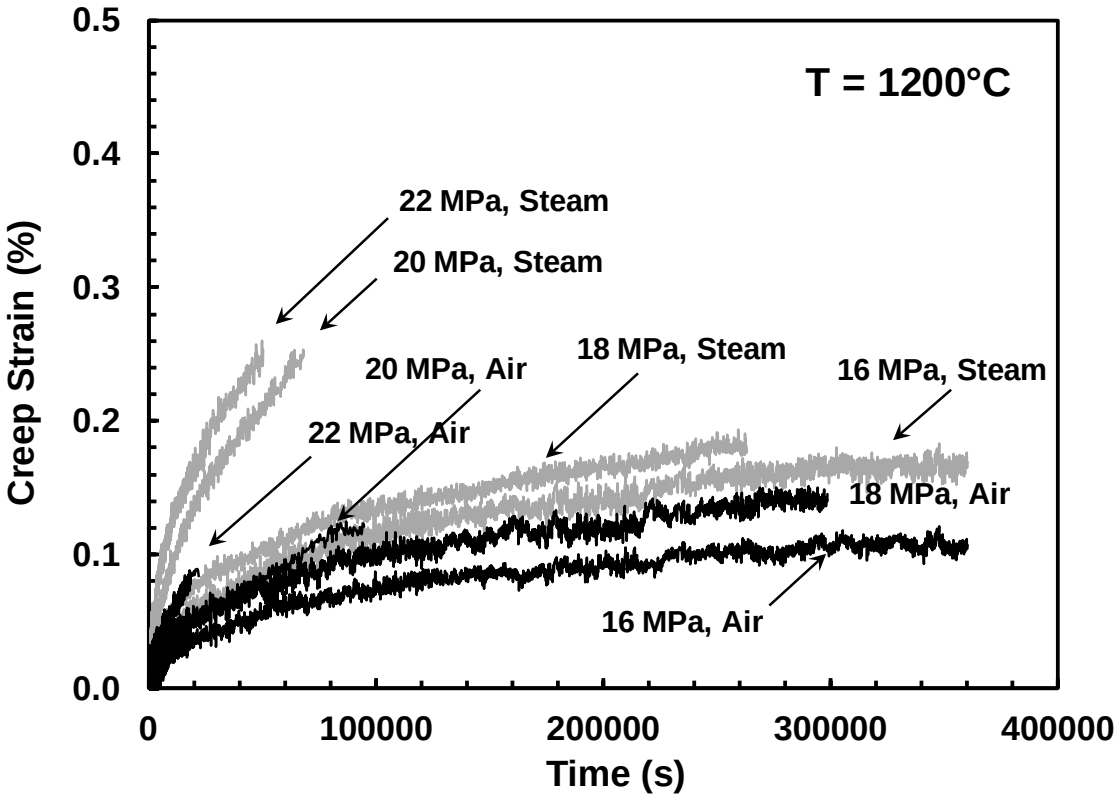

Figure 21 – Creep strain vs. time curves for Hi-Nicalon/PyC/HyperSiC Ceramic Composite obtained at applied interlaminar shear stresses in the 16-22 MPa range at 1200 °C in air and in steam

Stress-rupture behavior is summarized in Fig. 22, where applied shear stress is plotted vs. time to rupture at 1200 °C in air and in steam. In air and in steam, creep run-out of 100 h was achieved at 16 MPa (58.8% ILSS). For applied shear stress of 18 MPa the presence of steam has little effect on creep lifetime. The reduction in creep lifetime due to steam was limited to 12%. At 20 MPa, the reduction in creep life due to steam was more significant at 28%. However, at 22 MPa, the presence of steam appeared to be beneficial and extended creep lifetime.

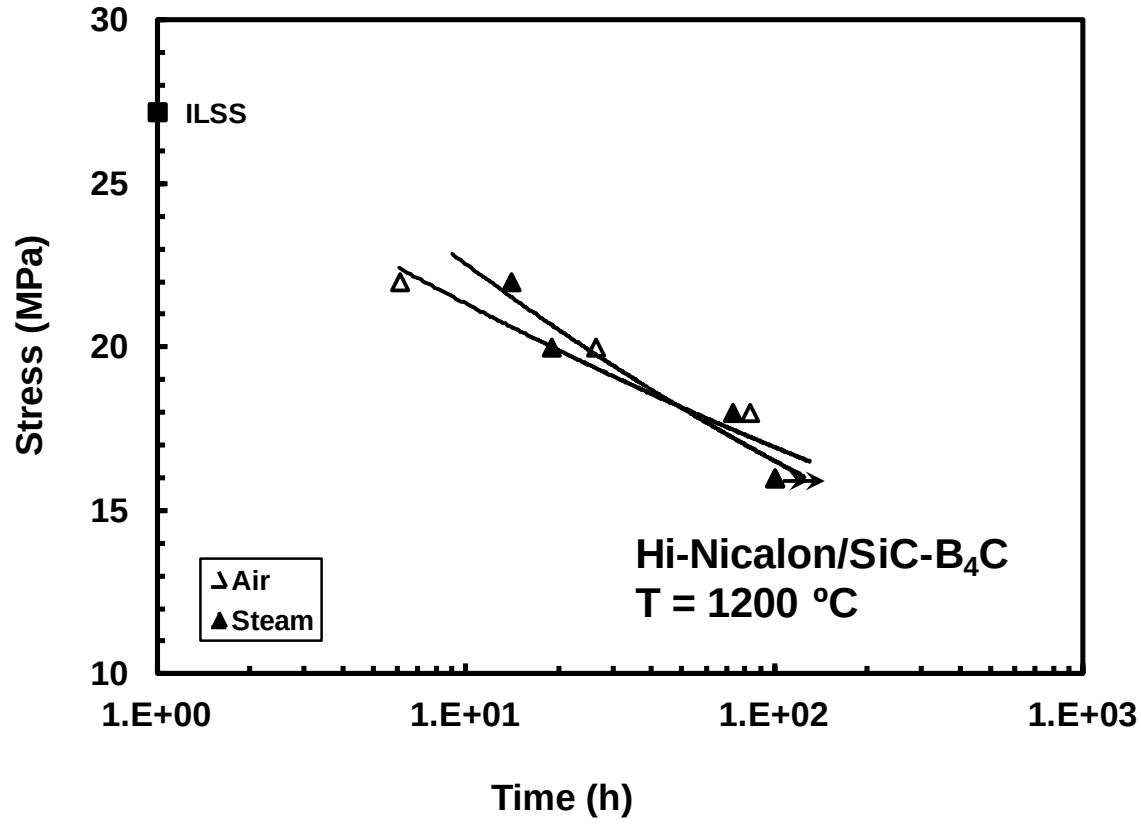

Figure 22 - Interlaminar shear stress vs. time to rupture for Hi-Nicalon/PyC/HyperSiC Ceramic Composite at 1200 °C

Minimum Strain Rate

Minimum creep rate was measured in all tests. Creep strain rate as a function of applied stress is shown in Figure 23. In steam, the minimum creep rate increases by a factor of ~12 when applied stress increases from 16 to 22 MPa. At the lowest (runout) creep stress of 16 MPa, the creep rate in steam is ~4 times more than that in air at the same stress. At the highest creep stress of 22 MPa, creep rate in steam is only about 70% of that observed in air.

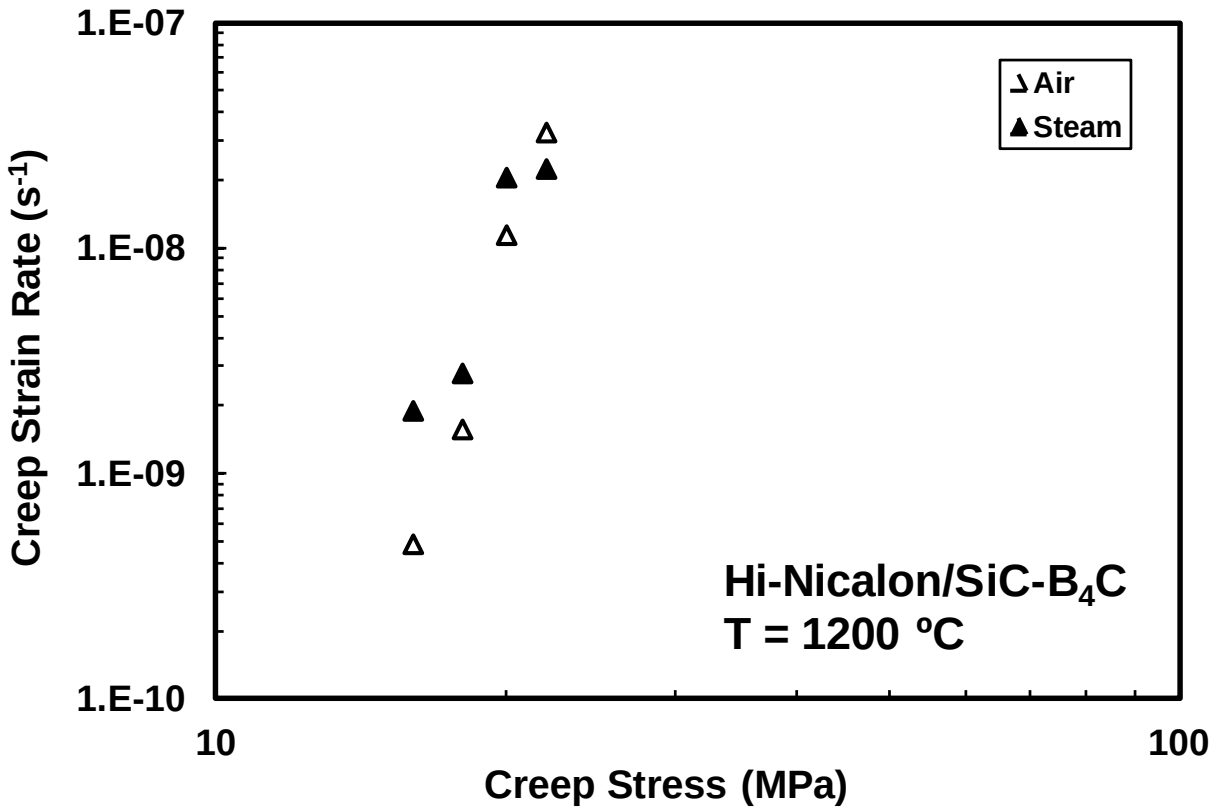

Figure 23- Minimum creep rate as a function of applied stress for Hi-Nicalon/PyC/HyperSiC Ceramic Composite at 1200 °C

Retained Properties

Specimens that achieved the 100-hour runout were subjected to compression tests to failure to characterize the retained interlaminar shear properties. Retained ILSS values of the specimens that achieved a run-out at 16 MPa in air and in steam are given in Table 10. The stress-strain curves obtained for the Hi-Nicalon/SiC-B_4C specimens subjected to prior creep in interlaminar shear in air and in steam are presented in Fig. 24. The ILSS of the specimen pre-crept at 16 MPa in air has decreased only by ~4% compared to the ILSS of the as-processed specimen. Conversely, prior creep in steam has degraded the ILSS of Hi-Nicalon/SiC-B_4C by a considerable 25%. The specimen

pre-crept at 16 MPa in steam retained approximately 75% of its ILSS. As seen in Fig. 24, prior creep in either environment had little qualitative effect on stress-strain behavior.

Table 10 - Summary of the retained properties of Hi-Nicalon/PyC/HyperSiC Ceramic composite subjected to prior creep at 1200°C

Specimen	Creep Stress	Retained Interlaminar Shear Strength (MPa)	Strength Retention (%)	Failure Strain (%)
Laboratory Air				
P6-4	16	26.1	96.0%	0.068
Steam				
P2-5	16	20.4	75.0%	0.17

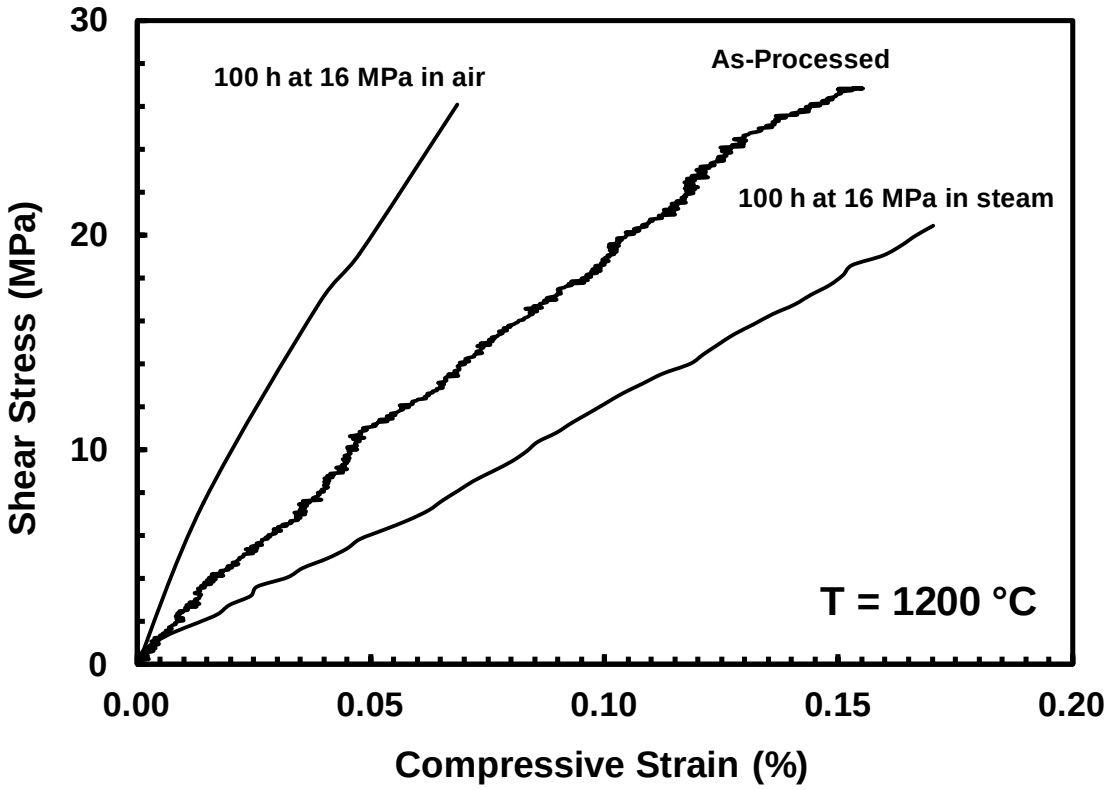

Figure 24 - Effects of prior creep in interlaminar shear on interlaminar shear stress - compressive strain behavior of Hi-Nicalon/PyC/HyperSiC Ceramic Composite at 1200 °C

Composite Microstructure

When a specimen failed, the testing machine was immediately shut off and the bottom half of the failed specimen was removed from the furnace. Hence, the interior of the fracture surface of the bottom half of the failed specimen was exposed to significant temperatures and prolonged oxidation for only a few minutes. These are the fracture surfaces that were examined with an SEM.

Figure 25 shows a typical fracture surface of the DNS specimen tested in compression to failure at 1200 °C in air. Delamination of the woven 0°/90° fiber layers from the matrix-rich regions appears to be the primary mechanism of interlaminar shear failure. Most of the fracture surface in Fig. 25 (a) is fairly smooth and clean, indicating that only a single fiber layer is associated with delamination. However, some rough areas exposing debris and fiber fracture (Fig. 25(a)) are also visible. Higher magnification images (Figs. 25 (b) and (c)) show that in the process of delamination the departing fibers leave distinct troughs in the remaining matrix. It is seen that small amounts of the matrix material remain bonded to the fibers exposed during delamination.

(a)

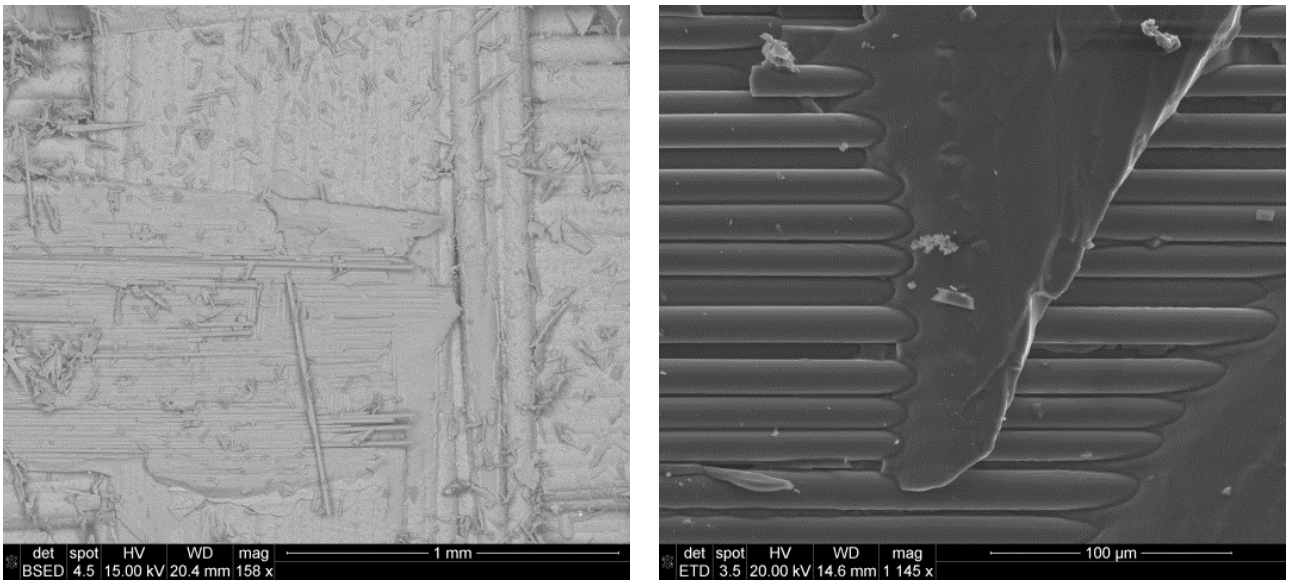

(b) (c)

Figure 25 - Fracture surface of the Hi-Nicalon/SiC-B_4C DNS specimen tested in compression to failure at 1200 °C in air. Test duration < 5 s.

In contrast, the fracture surfaces of the DNS specimens tested in compression creep at 1200 °C in air or in steam (see Figs. 26-33) reveal that the failure mechanisms in

these cases include various degrees of fiber fracture. It is noteworthy that the amount of fiber fracture appears to be influenced by test duration and test environment.

Consider the fracture surface produced in creep test performed at 22 MPa at 1200°C in air (Fig. 26 (a) and (b)). Recall that this specimen failed after 6.1 h in creep.

(a) (b)

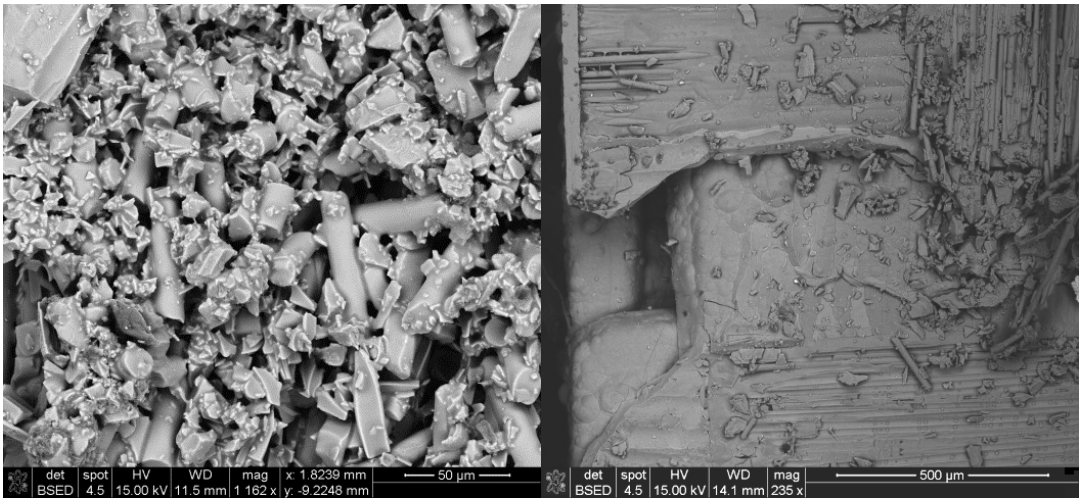

(c) (d)

Figure 26 - Fracture surface of the Hi-Nicalon/SiC-B_4C DNS specimen tested in creep at 22 MPa and 1200 °C in air. Time to rupture = 6.1 h.

The fracture surface (Fig. 26 (a) and (b)) shows that in this case, the failure mechanism includes noticeable fiber fracture. Some areas of the fracture surface still show clean delamination of a single fiber layer from the matrix-rich regions. However, noticeable rougher areas of the fracture surface (Figs. 26 (a) and (b)) show increased damage in fiber tows, occasionally exposing multiple 0°/90° fiber layers (Fig. 26 (d)). As seen in Fig. 26 (c), the failure also involves extensive damage to the matrix. Considerable amounts of fiber fragments and matrix debris are observed on the periphery of the fracture surface (Fig. 26 (c)).

Figure 27 presents the micrographs of the fracture surface produced in creep test performed at 22 MPa at 1200°C in steam. Creep lifetime achieved in this test was 14 h. Note that the fracture surface in Figure 27 does not show the extensive amount of fiber fragments and matrix debris observed around the periphery of the fracture surface produced in the 22 MPa creep test performed in air. A considerable area of the fracture surface in Figs. 27 (a) and (b) shows clean delamination of a single fiber layer with minimal fiber fracture and minimal matrix damage. Higher magnification images (Figs. 27 (c), (d), (e)) show grooves left in the matrix by the fibers during the aforementioned process of delamination. Glassy phase forming at the edges of the fracture surface is seen in Fig. 27 (f). Fig. 27 (f) also shows some of this glassy phase covering the fibers near the edge of the fracture surface. The glassy phase is most likely boria glass formed by reaction of B_4C matrix layers with the oxidizing environment.

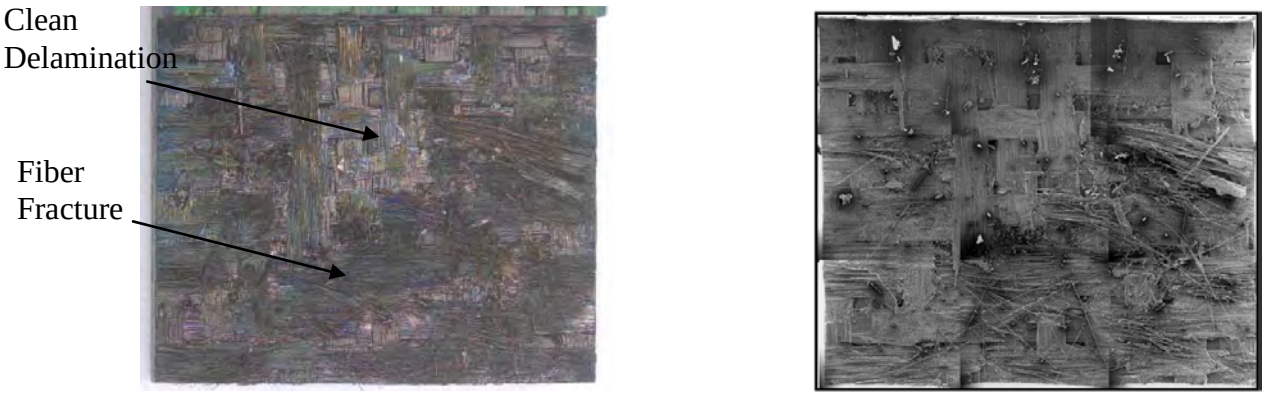

(a) (b)

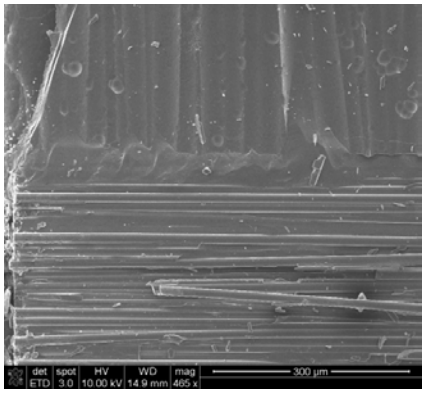

(c)

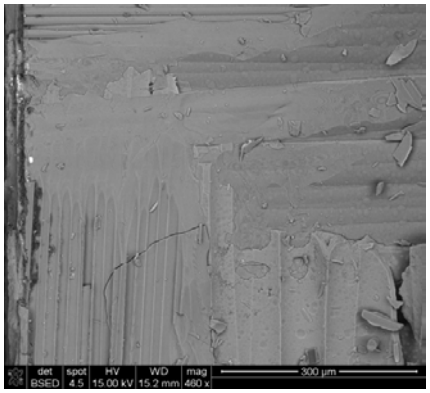

(d)

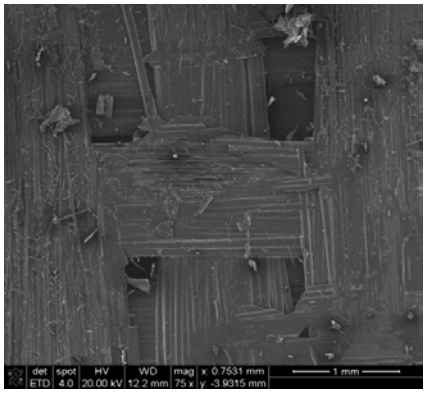

(e)

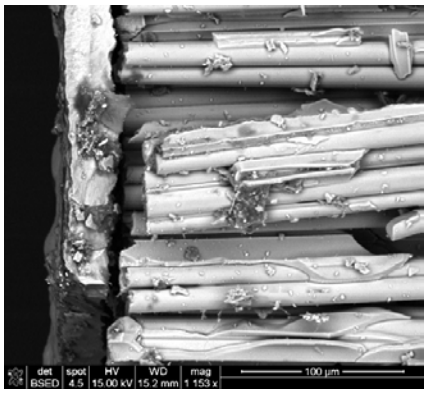

(f)

Figure 27 - Fracture surface of the Hi-Nicalon/SiC-B_4C DNS specimen tested in creep at 22 MPa and 1200 °C in steam. Time to rupture = 14 h.

Figure 28 presents the micrographs of the fracture surface produced in creep test performed at 20 MPa at 1200°C in air. Creep lifetime achieved in this test was 26.3 h.

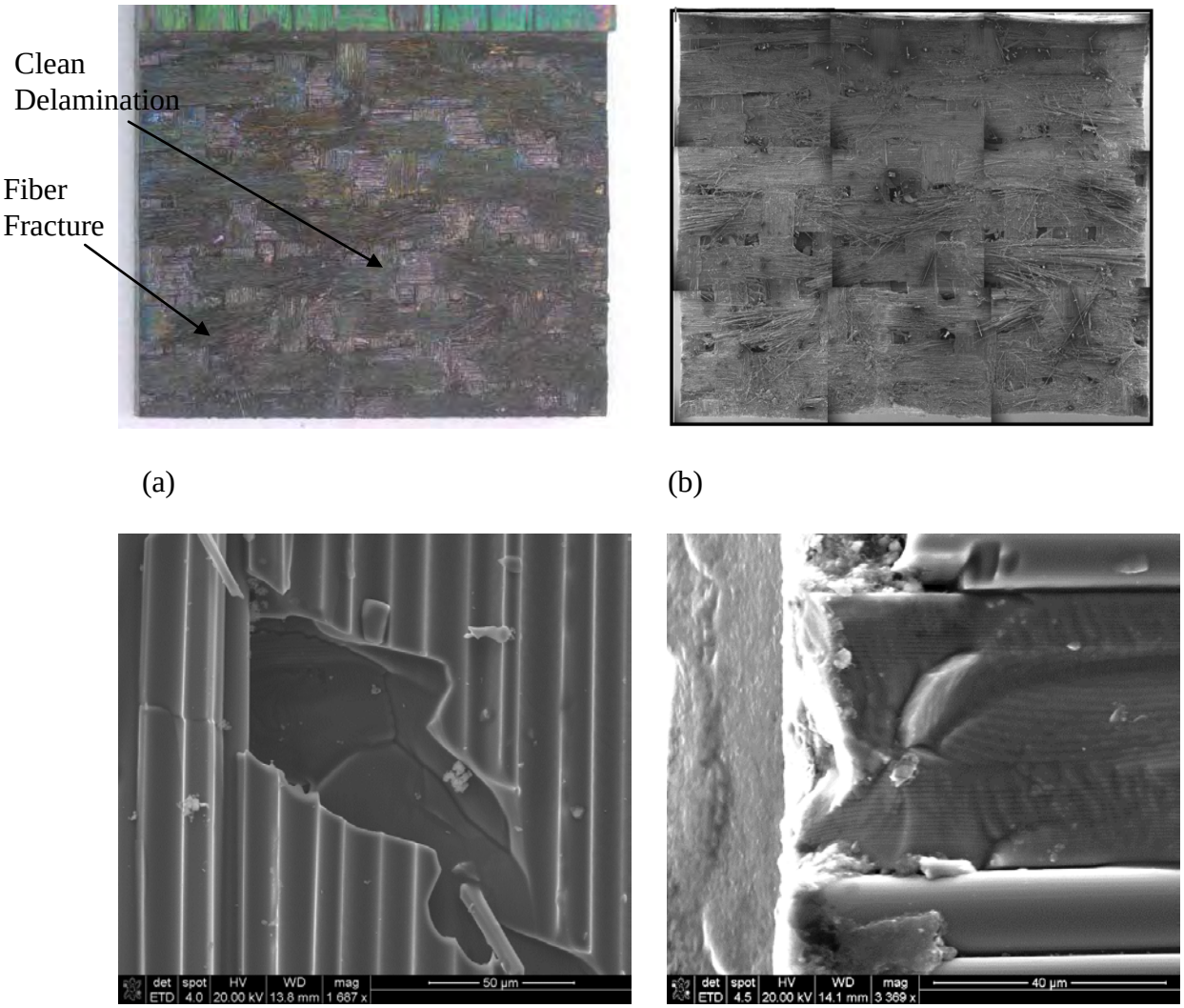

Figure 28 -Fracture surface of the Hi-Nicalon/SiC-B_4C DNS specimen tested in creep at 20 MPa and 1200 °C in air. Time to rupture = 26.3 h.

Fracture surface in Figs. 28 (a) and (b) produced in the 20 MPa creep test in air shows a greater amount of fiber fracture and matrix damage than that obtained in the 22 MPa creep test performed in air (see Fig. 26). Apparently, test duration is causing a

progressive change in the failure mechanism. In the 22 MPa test of shorter 6.1-h duration, matrix damage and interply delamination appeared to be the dominant failure mechanisms. Contrastingly, in the 20 MPa test of 26.3-h duration, considerable fiber fracture is now observed. Very few areas of clean interply delamination can be seen in the fracture surface. One of those areas is seen in the higher magnification image in Fig. 28 (c), which shows grooves left in the matrix by the fibers in the course of delamination. Despite a longer test duration, and consequently a longer exposure to the oxidizing environment at elevated temperature under load, only little amounts of glassy phase were observed at the edges of the fracture surface. Figure 28 (d) shows some glassy phase, believed to be boria, at the periphery of the fracture surface.

Figure 29 presents the micrographs of the fracture surface obtained in creep test performed at 20 MPa at 1200°C in steam. Creep lifetime produced in this test was 19 h.

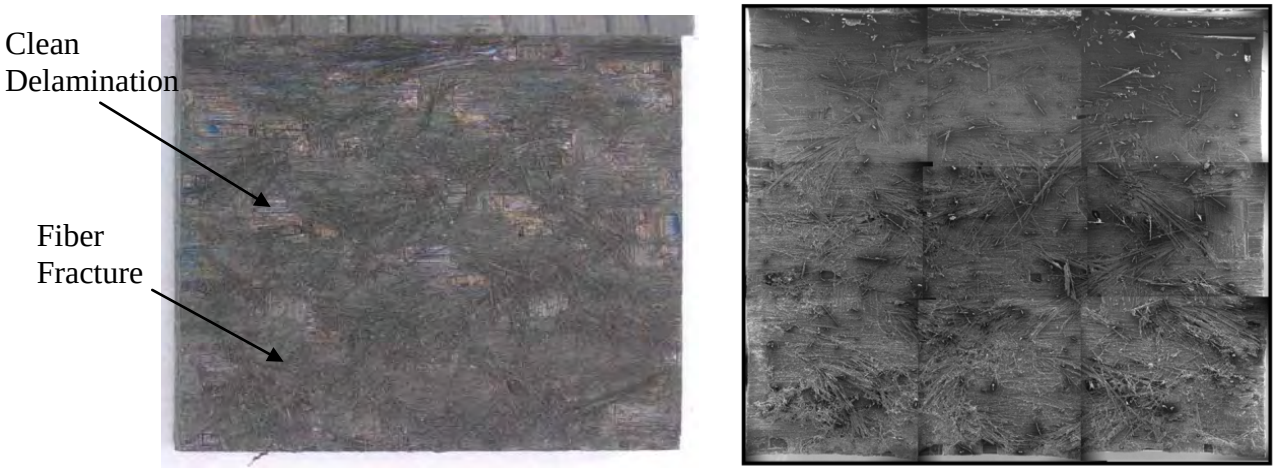

(a) (b)

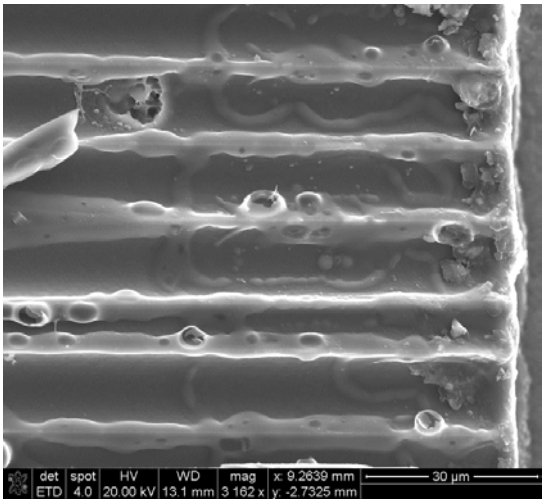
det spot HV WD mag x: 9.2639 mm 30 µm
ETD 4.0 20.00 kV 13.1 mm 3 162 x y: -2.7325 mm

(c)

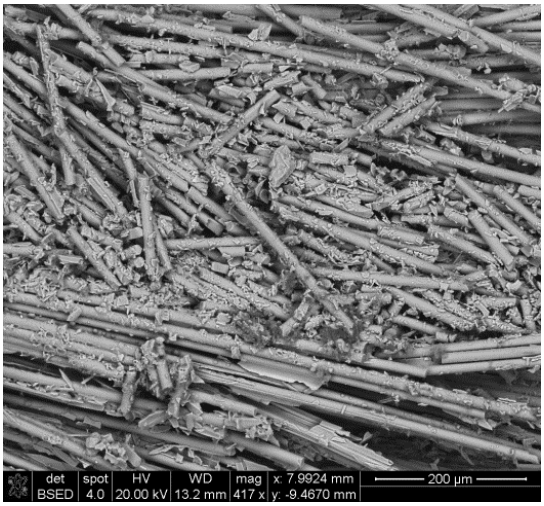
det spot HV WD mag x: 7.9924 mm 200 µm
BSED 4.0 20.00 kV 13.2 mm 417 x y: -9.4670 mm

(d)

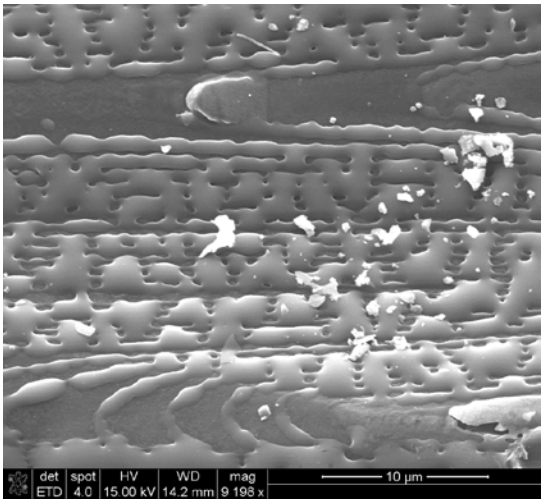
det spot HV WD mag 10 µm
ETD 4.0 15.00 kV 14.2 mm 9 198 x

(e)

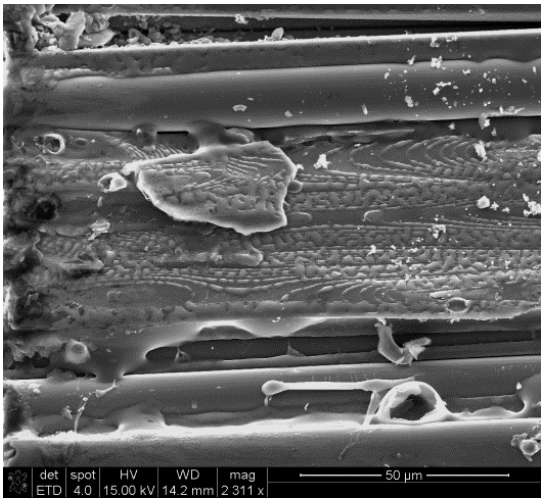
det spot HV WD mag 50 µm
ETD 4.0 15.00 kV 14.2 mm 2 311 x

(f)

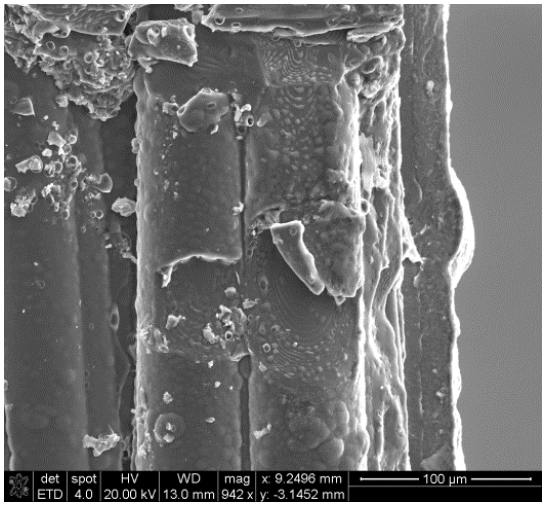
det spot HV WD mag x: 9.2496 mm
ETD 4.0 20.00 kV 13.0 mm 942 x y: -3.1452 mm
100 µm

(g)

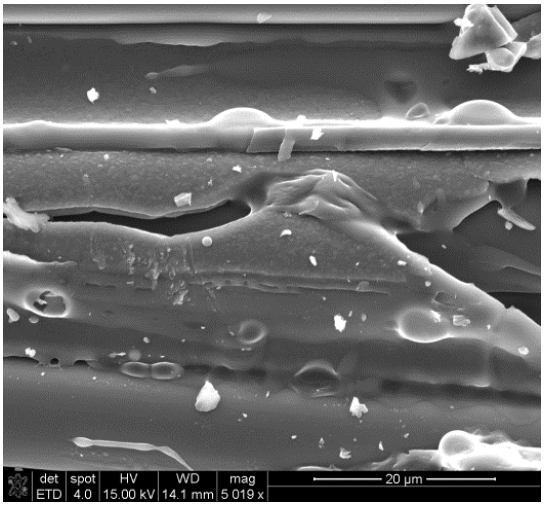
det spot HV WD mag
ETD 4.0 15.00 kV 14.1 mm 5 019 x
20 µm

(h)

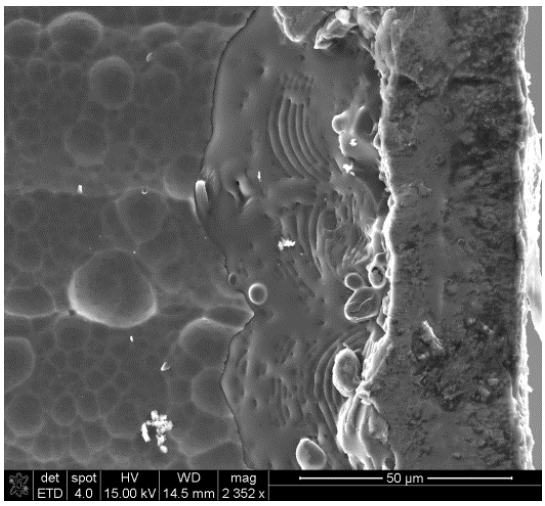
det spot HV WD mag
ETD 4.0 15.00 kV 14.5 mm 2 352 x
50 µm

(i)

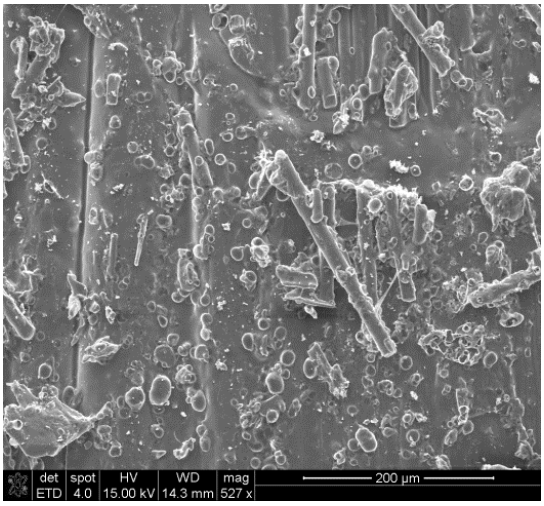
det spot HV WD mag
ETD 4.0 15.00 kV 14.3 mm 527 x
200 µm

(j)

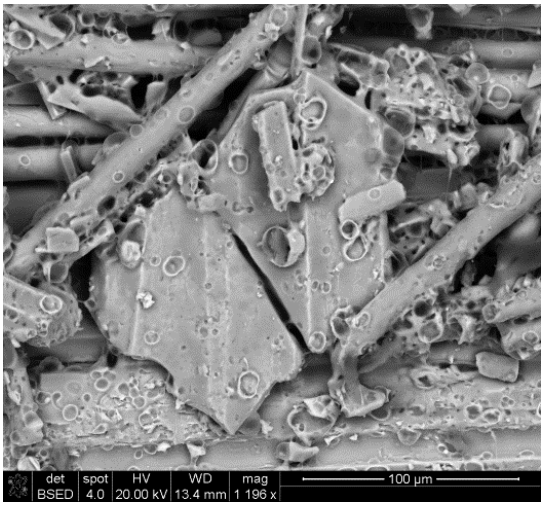

(k)

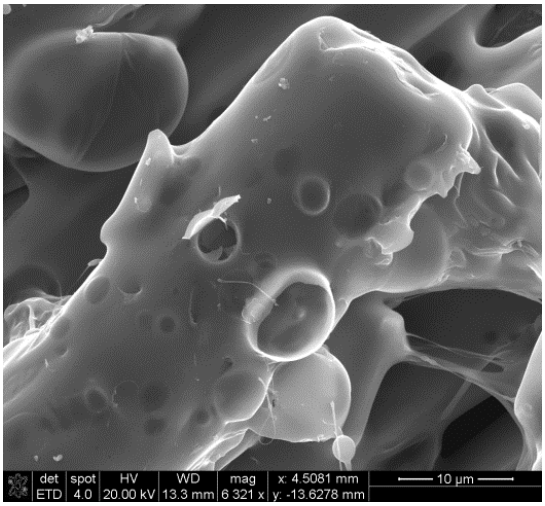

(l)

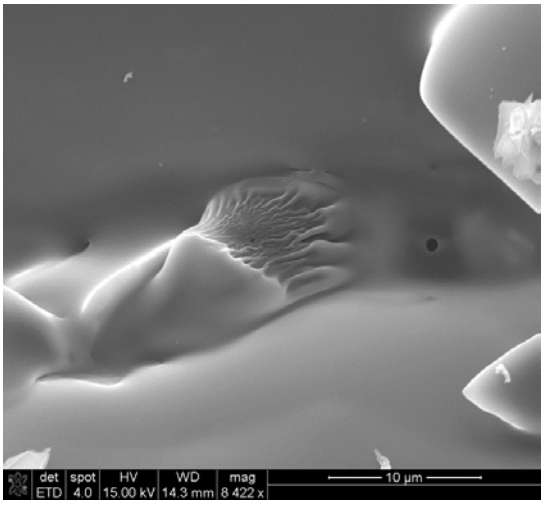

(m)

Figure 29 - Fracture surface of the Hi-Nicalon/SiC-B_4C DNS specimen tested in creep at 20 MPa and 1200 °C in steam. Time to rupture = 19 h.

Fracture surface in Figs. 29 (a) and (b) produced in the 20 MPa creep test in steam shows a greater amount of fiber fracture and matrix damage than that obtained in the 22 MPa creep test performed in steam (see Fig. 27). It was noted that at 1200°C in air, the test duration caused a progressive change in failure mechanism. The same observation can be made regarding the tests performed at 1200°C in steam. In the 22

MPa test of a shorter 14-h duration matrix damage and interply delamination appeared to be the primary failure mechanisms. Conversely, considerable fiber fracture and fewer areas of clean interply delamination can be seen in the fracture surface produced in the 20 MPa test of 19-h duration. A higher magnification image in Fig. 29 (c) shows grooves left in the matrix by the fibers during interply delamination at 22 MPa in steam. Fiber fragments can be seen in some limited areas of the fracture surface (see Fig. 29 (d)). Note that Fig. 29 (d) shows some matrix bonded to the fiber fragments. Furthermore, glassy layer appears to be covering the fiber fragments in Fig. 29 (d). Higher magnification images in Figs. 29 (e)-(m) reveal a widespread formation of the glassy phase throughout the fracture surface. Figure 29 (e) shows glassy phase that is most likely boria glass resulting from the B_4C matrix layers. It is likely that the oxidation of the B_4C matrix layers is followed by the oxidation of the SiC in the matrix, thus resulting in the formation of the borosilicate glass during the test. Bubbles, which are seen in the higher magnification images in Figs. 29 (h)-(l), are most likely the gaseous reaction products diffusing through the borosilicate glass. Note that the borosilicate glass has higher viscosity than boria glass, thereby making it more difficult for the gaseous reaction products to escape.

Figure 30 presents the micrographs of the fracture surface obtained in creep test performed at 18 MPa at 1200°C in air. Creep lifetime produced in this test was 83 h. Fracture surface in Figs. x (a) and (b) shows a large amount of fiber fracture and matrix damage and is dominated by areas exposing multiple 90° fiber bundles. As the test duration increased to 83 h, the failure mechanism has changed dramatically to include extensive fracture of fiber tows.

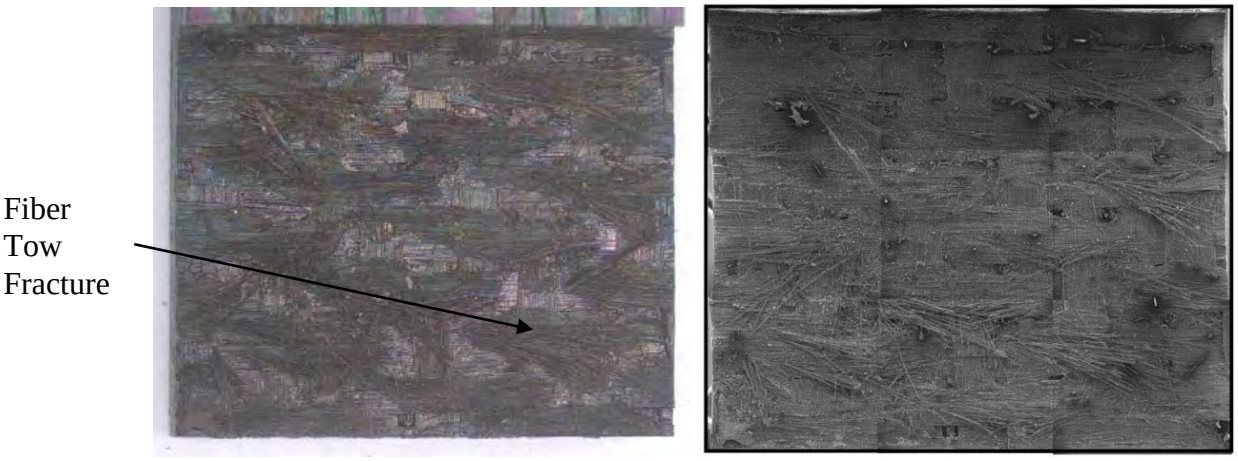

(a) (b)

Figure 30 - Fracture surface of the Hi-Nicalon/SiC-B_4C DNS specimen tested in creep at 18 MPa and 1200 °C in air. Time to rupture = 83 h.

Fracture surface produced in creep test performed at 18 MPa at 1200°C in steam is shown in Figure 31. Creep lifetime produced in this test was 73 h.

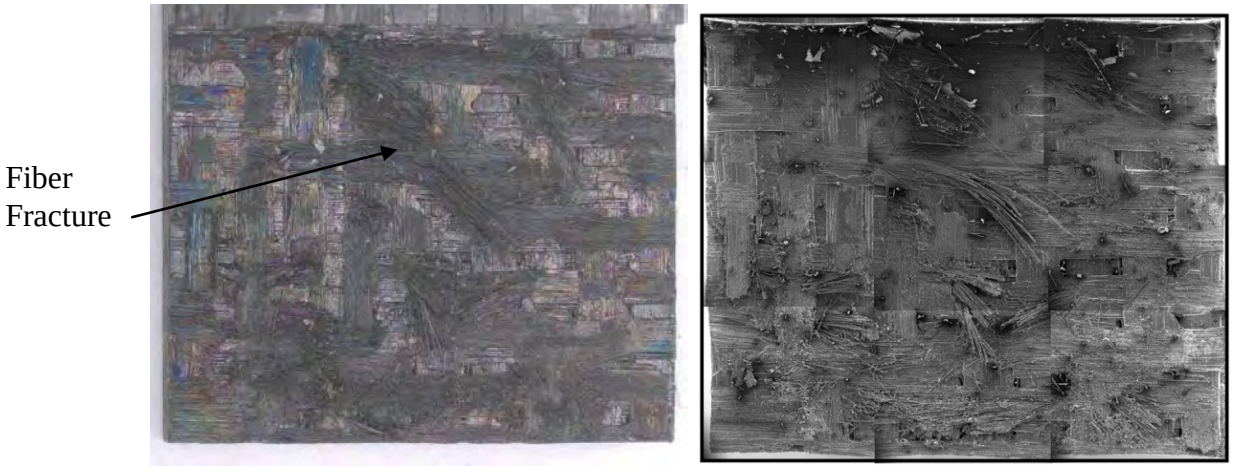

(a) (b)

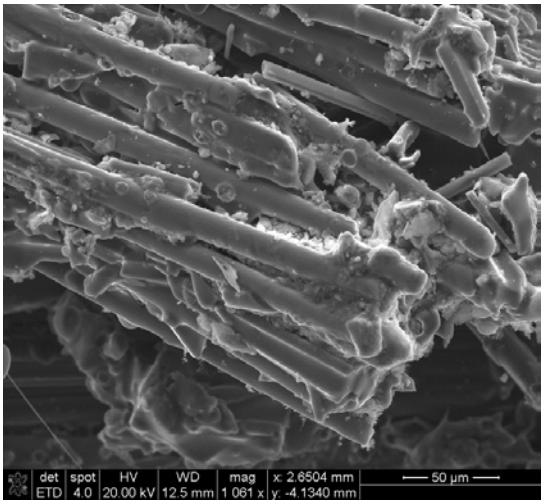
det spot HV WD mag x: 2.6504 mm
ETD 4.0 20.00 kV 12.5 mm 1 061 x y: -4.1340 mm
50 µm

(c)

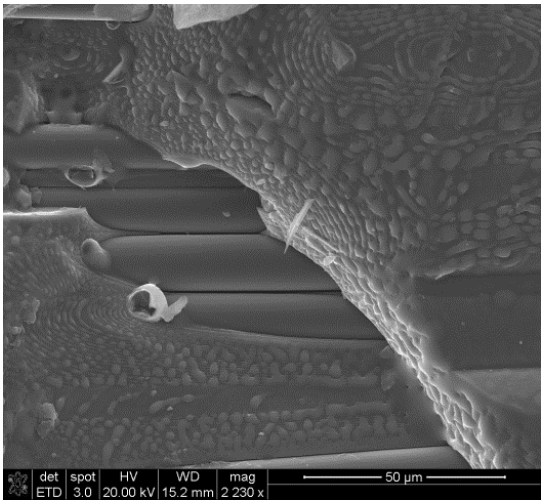
det spot HV WD mag
ETD 3.0 20.00 kV 15.2 mm 2 230 x
50 µm

(d)

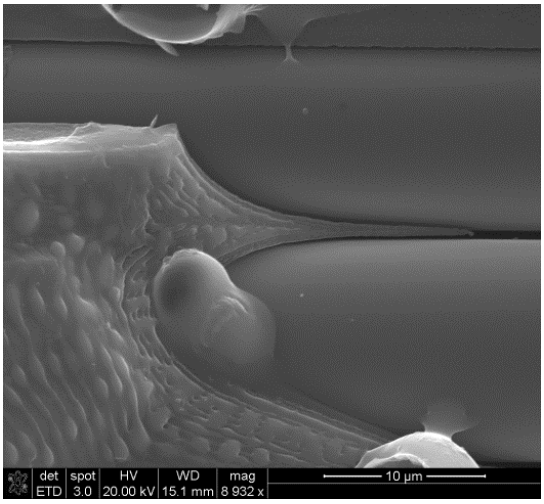
det spot HV WD mag
ETD 3.0 20.00 kV 15.1 mm 8 932 x
10 µm

(e)

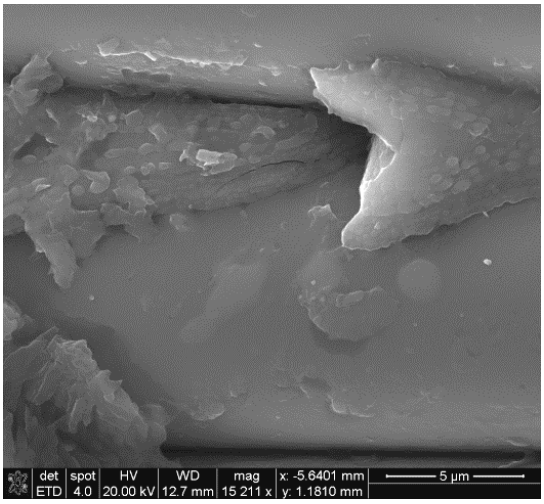
det spot HV WD mag x: -5.6401 mm
ETD 4.0 20.00 kV 12.7 mm 15 211 x y: 1.1810 mm
5 µm

(f)

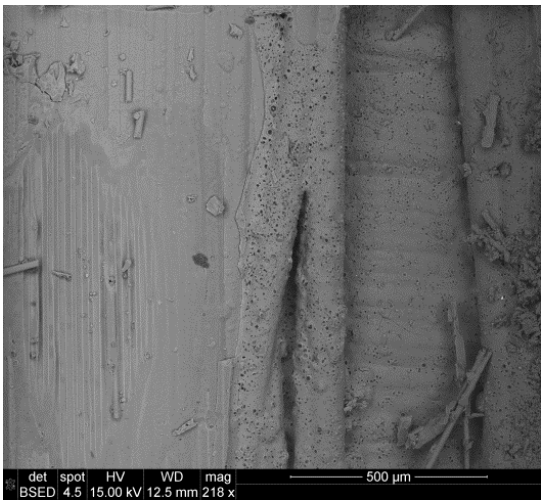
det spot HV WD mag
BSED 4.5 15.00 kV 12.5 mm 218 x
500 µm

(g)

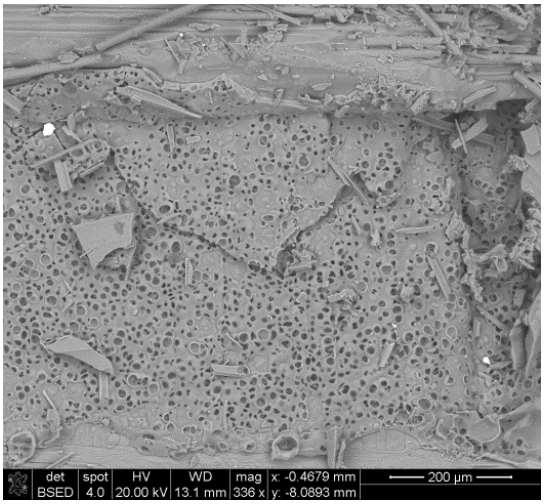
det spot HV WD mag x: -0.4679 mm
BSED 4.0 20.00 kV 13.1 mm 336 x y: -8.0893 mm
200 µm

(h)

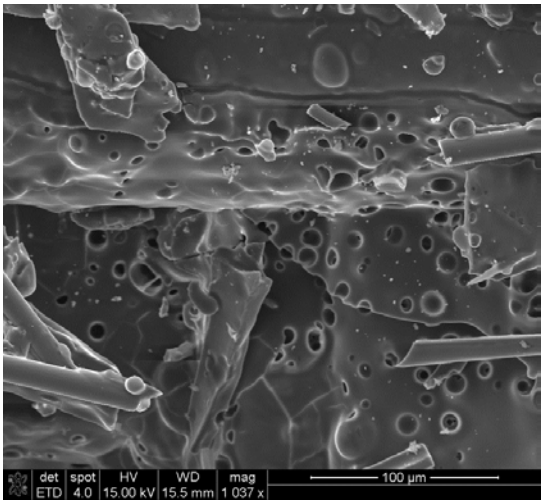
det spot HV WD mag
ETD 4.0 15.00 kV 15.5 mm 1 037 x
100 µm

(i)

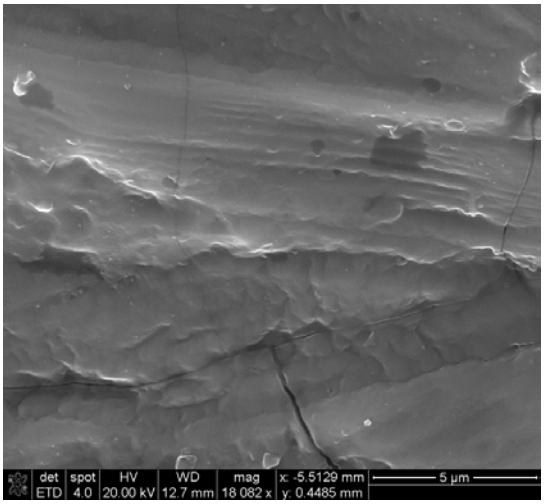
det spot HV WD mag x: -5.5129 mm
ETD 4.0 20.00 kV 12.7 mm 18 082 x y: 0.4485 mm
5 µm

(j)

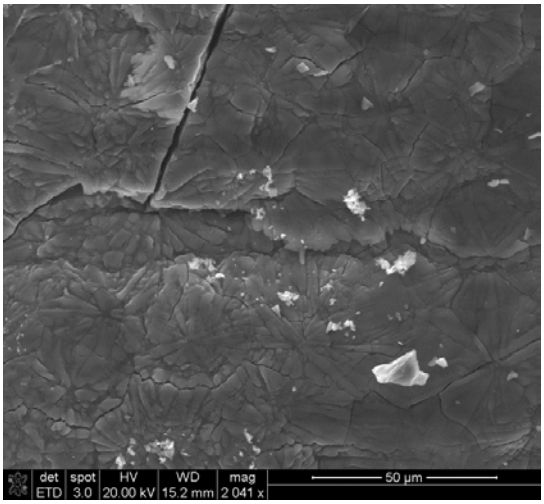

(k)

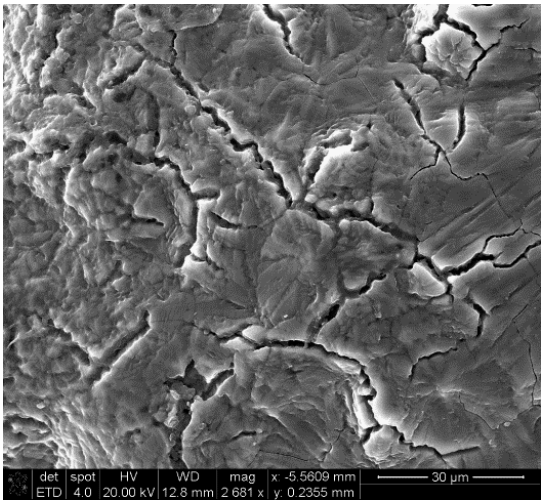

(l)

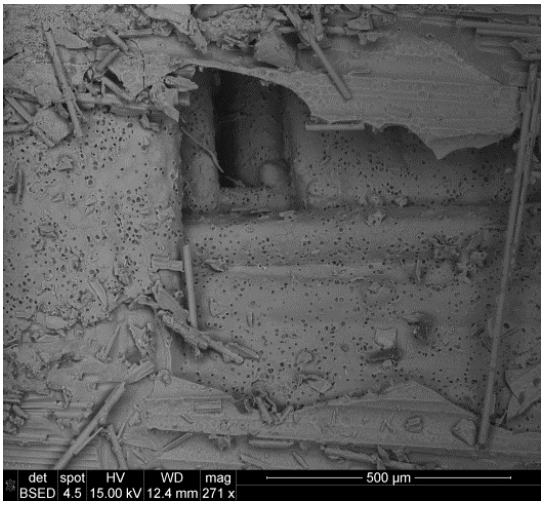

(m)

Figure 31 -Fracture surface of the Hi-Nicalon/SiC-B_4C DNS specimen tested in creep at 18 MPa and 1200 °C in steam. Time to rupture = 73 h.

Fracture surface in Figs. 31 (a) and (b) shows extensive fiber fracture and matrix damage. Areas of clean interply delamination are not observed. As in the case of the test performed in air, the increase in test duration to 73 h caused a dramatic change in the failure mechanism. Fiber fracture is now the primary failure mechanism. Longer test duration also translates into increased exposure to oxidizing environment at elevated

temperature, which causes pervasive formation of the glassy phase throughout the fracture surface (Figs. 31 (d)-(m)). Additionally, extensive fiber-matrix bonding is observed (Fig. 31 (c)). It appears that the glassy phase has crystallized near the edges of the fracture surface (see Fig. 31 (k) and (l)). It is likely that borosilicate glass is the glassy phase present on this fracture surface. However, it is possible that due to prolonged test duration in steam, only silica remains in some areas. The EDS analysis would have to be performed to reach a definitive conclusion.

Figure 32 presents the micrographs of the fracture surface subjected to 100 h of creep at 16 MPa then failed in compression at 1200°C in air. Fracture surface in Figs. 32 (a) and (b) is dominated by areas exposing multiple 90° fiber bundles. Extensive fiber fracture is evident. With the test duration exceeding 100 h, the primary failure mechanism has changed from interply delamination to fracture of fiber tows. Higher magnification image in Fig. 32 (c) shows an area of fiber fracture and matrix damage. Some fiber fragments and pulverized matrix can be seen around the periphery of the fracture surface (Fig. 32 (d)).

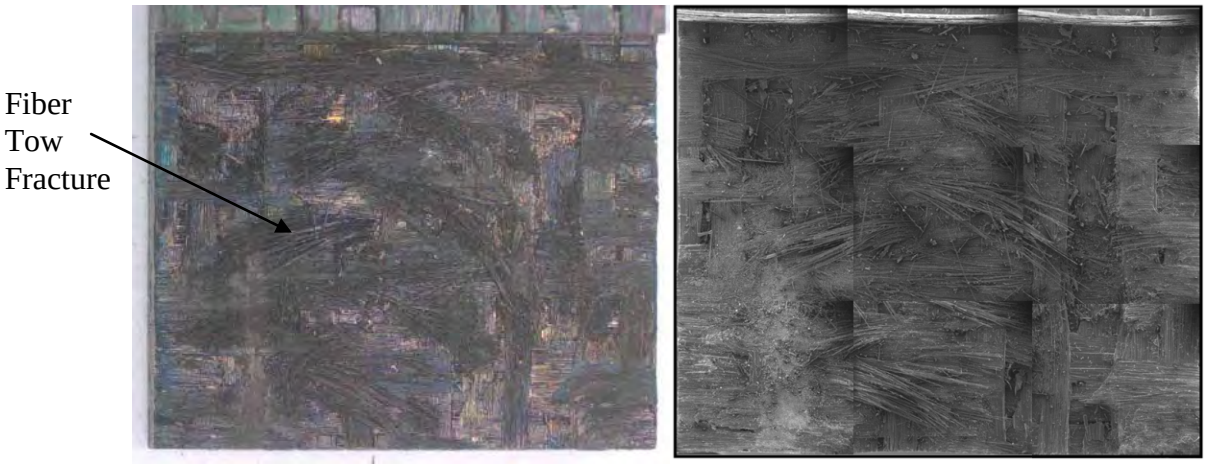

(a) (b)

(c)

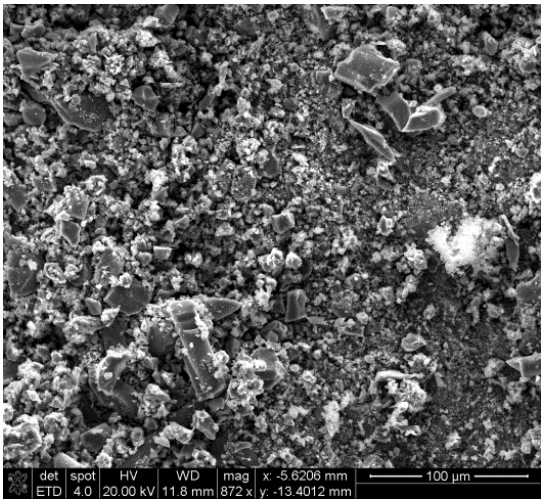

(d)

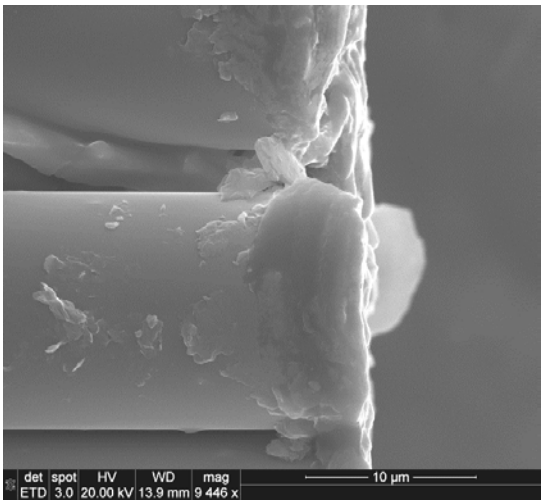

(e)

Figure 32 - Fracture surface of the Hi-Nicalon/SiC-B_4C DNS specimen subjected to 100 h of creep at 16 MPa then failed in compression and 1200 °C in air.

It appears that even such prolonged exposure (> 100 h) at 1200°C in air under load did not result in significant formation of the glassy phase on the fracture surface. Only minimal amounts of glassy phase were observed at the periphery of the fracture surface. Figure 32 (e) shows some glassy phase covering the tips of the fibers at the edge of the fracture surface. Glassy phase was not observed in the interior of the fracture surface.

Figure 33 presents the micrographs of the fracture surface subjected to 100 h of creep at 16 MPa then failed in compression at 1200°C in steam. Fracture surface in Figs. 33 (a) and (b) is dominated by extensive fiber fracture. Areas of violent failure exposing multiple 0°/90° fiber layers (shown Figs. 33 (c) and (d)) are seen throughout the fracture surface. Extensive fiber/matrix bonding is also observed throughout the fracture surface. Damaged fibers and matrix (shown in Figs. 33 (e)-(h)) are observed in multiple areas of the fracture surface. No areas of clean interply delamination can be found. The primary failure mechanism has completely changed from interply delamination to fracture of fiber tows.

(a) (b)

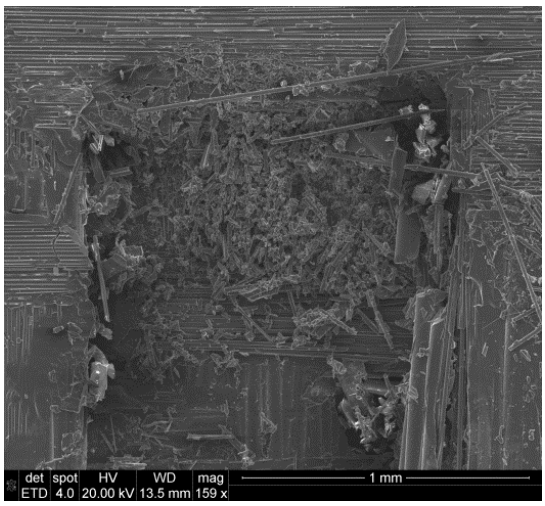
det spot HV WD mag
ETD 4.0 20.00 kV 13.5 mm 159 x
1 mm

(c)

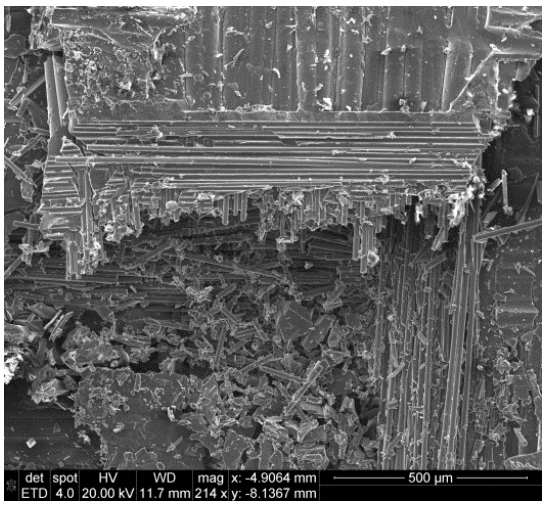
det spot HV WD mag x: -4.9064 mm
ETD 4.0 20.00 kV 11.7 mm 214 x y: -8.1367 mm
500 µm

(d)

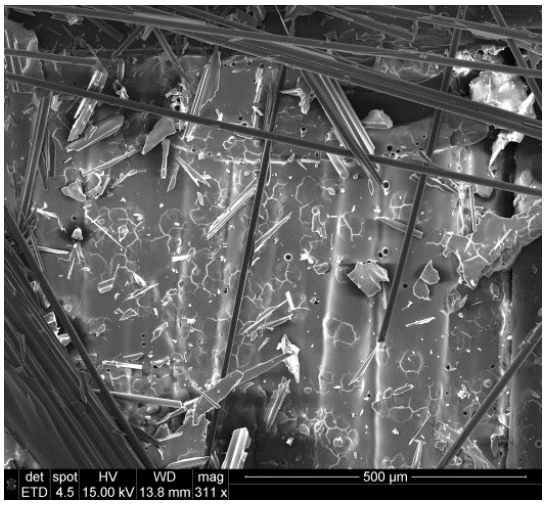
det spot HV WD mag
ETD 4.5 15.00 kV 13.8 mm 311 x
500 µm

(e)

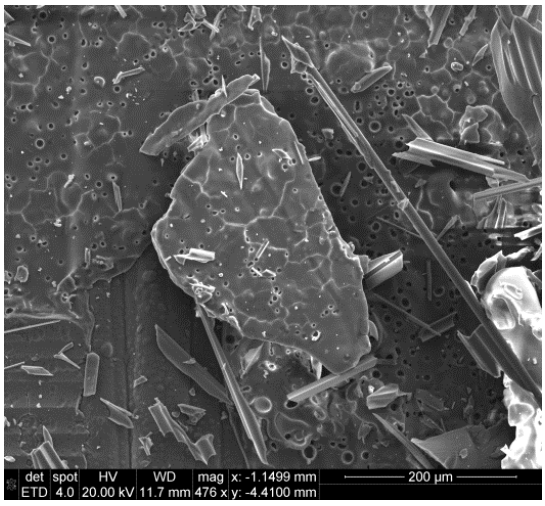
det spot HV WD mag x: -1.1499 mm
ETD 4.0 20.00 kV 11.7 mm 476 x y: -4.4100 mm
200 µm

(f)


det spot HV WD mag
BSED 4.5 15.00 kV 13.5 mm 398 x
400 µm

(g)


det spot HV WD mag
BSED 4.0 15.00 kV 19.4 mm 327 x
500 µm

(h)

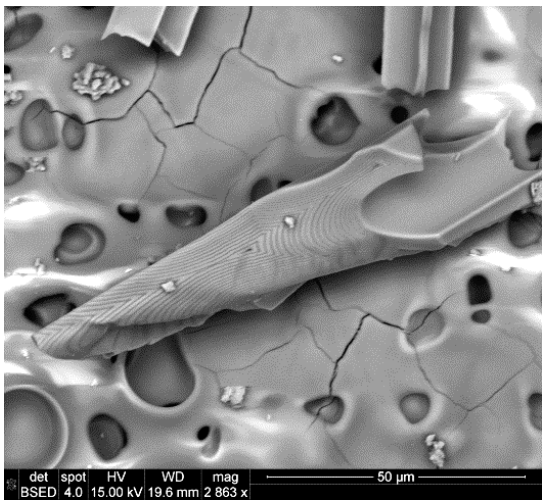
det spot HV WD mag
BSED 4.0 15.00 kV 19.6 mm 2 863 x
50 µm

(i)

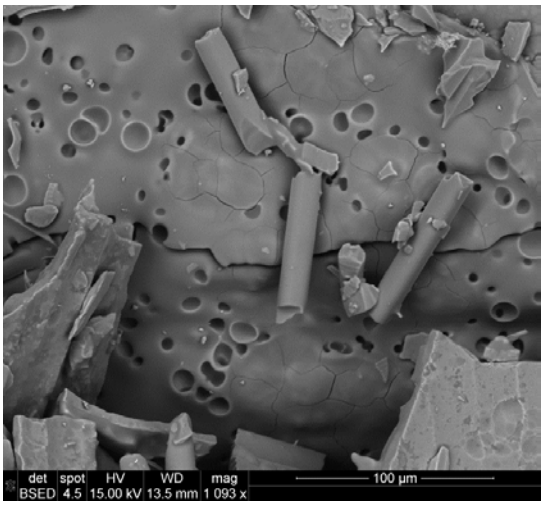
det spot HV WD mag
BSED 4.5 15.00 kV 13.5 mm 1 093 x
100 µm

(j)

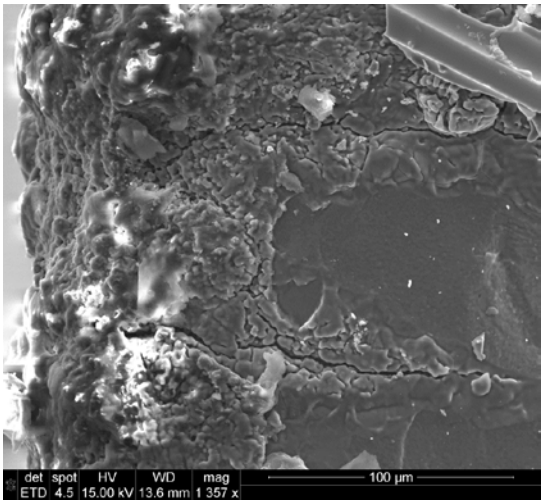

(k)

Figure 33 - Fracture surface of the Hi-Nicalon/SiC-B_4C DNS specimen subjected to 100 h of creep at 16 MPa then failed in compression and 1200 °C in steam.

Pervasive formation of the glassy phase is observed throughout the fracture surface. It is recognized that the increased amounts of the glassy phase are caused by the increased (>100 h) exposure at 1200°C in steam under load. It is likely that the oxidation of the B_4C matrix layers is followed by the oxidation of the SiC in the matrix, thus resulting in the formation of the borosilicate glass during the test. However, the EDS analysis would have to be performed to reach a definitive conclusion. Figures 33 (i) and (j) shows glassy phase present on the fracture surface. Note the "craters" in Figs. 33 (i) and (j), which are left in the glassy layer by escaping gases. Recall that gaseous reaction products are formed along with the glassy phase. If the viscosity of the glassy layer is high, the gases can only diffuse relatively slowly through the glassy layer. In the presence of steam, viscosity of the glassy layer decreases, allowing the gaseous reaction products to escape thereby leaving behind the craters in the glassy layer. Figure 33 (k) shows a larger deposit of the glassy phase near the edge of the fracture surface.

Furthermore, it appears that the glassy phase in Fig. 33 (k) has crystallized and cracks have formed after cooling down to room temperature.

VI. Conclusions and Recommendations

Interlaminar shear behavior of a Hi-Nicalon/SiC-B4C ceramic composite was observed in both air and steam environments at 1200°C. Compression testing to failure was conducted to obtain and average as-processed interlaminar shear strength of 27.2 MPa and an average compressive failure strain of 0.149%.

Compressive creep behavior at 1200°C in both air and steam was evaluated for interlaminar shear stresses ranging from 16 to 22 MPa. Primary and secondary creep regimes are observed in both air and steam. At a compressive creep stress level of 16 MPa (~59% ILSS), the specimens achieved run-out of 100 hours at 1200°C in both air and steam.

The presence of steam only moderately affects creep lifetimes and larger creep strains are accumulated in steam than in air. At 18 MPa (~66% ILSS), steam decreased creep life by ~12% and increased strain by ~0.17%. At 20 MPa (~74% ILSS), the presence of steam decreased creep life by ~28% and increased strain by ~0.13%. However, at 22 MPa (~80% ILSS), the presence of steam actually increased creep life by ~123% and increased strain by ~0.06% above that observed in air.

The specimen pre-crept in steam strained to 0.170% and only retained 75% ILSS, whereas the specimen pre-crept in air strained to only 0.068% and retained 96% of the as-processed ILSS. The retained ILSS of the run-out specimen in air was only 4% less than

the as-processed ILSS but the strain for the specimen pre-crept in air (0.068%) was less than the as-processed material (0.149%). Secondary creep rates are not dramatically influenced by steam.

The dominant failure mechanism changes with increasing test duration at 1200°C in air and in steam. For tests of shorter duration (≤ 26 h), interply delamination and matrix damage are the primary failure mechanisms. For tests of longer duration (> 26 h), the primary failure mechanism becomes fiber fracture. Fracture surfaces produced at 1200°C in air do not exhibit significant amounts of glassy phase, irrespective of the test duration. Fracture surfaces produced at 1200°C in steam exhibit increasing amounts of glassy phase with increasing test duration.

Future efforts in characterizing this material should perform additional compressive creep tests to improve confidence in creep results. Creep tests in interlaminar shear using tensile loading could be compared with compressive creep results. Additional efforts should also evaluate the rate dependence of interlaminar shear strength. Finally, Energy Dispersive X-Ray Spectroscopy should be performed to establish glassy phase composition.

Appendix A: Additional Optical Micrographs

Figure 34 – P6-3, Fracture surface of Hi-Nicalon/PyC/HyperSiC Ceramic Composite specimen tested in compression to failure at 1200 °C in air

Figure 35 – P8-1, Fracture surface of Hi-Nicalon/PyC/HyperSiC Ceramic Composite specimen tested in compression to failure at 1200 °C in air

Figure 36 – P2-3, Fracture surface of Hi-Nicalon/PyC/HyperSiC Ceramic Composite specimen tested in compression to failure at 1200 °C in air

Figure 37 – P9-1, Fracture surface of Hi-Nicalon/PyC/HyperSiC Ceramic Composite specimen tested in compression to failure at 1200 °C in air

Figure 38 – P6-4, Fracture surface of Hi-Nicalon/PyC/HyperSiC Ceramic Composite specimen tested in creep at -16 MPa and 1200 °C in air

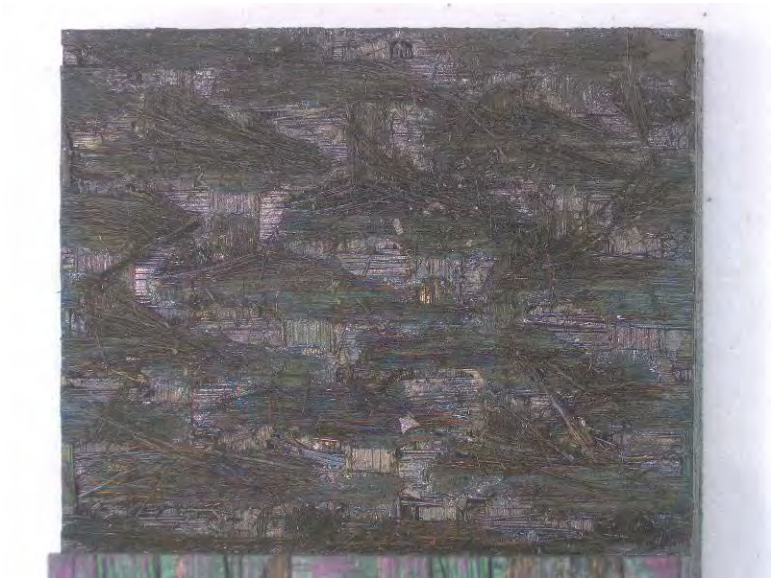

Figure 39 – P9-2, Fracture surface of Hi-Nicalon/PyC/HyperSiC Ceramic Composite specimen tested in creep at -18 MPa and 1200 °C in air

Figure 40 – P8-4, Fracture surface of Hi-Nicalon/PyC/HyperSiC Ceramic Composite specimen tested in creep at -20 MPa and 1200 °C in air

Figure 41 – P2-6, Fracture surface of Hi-Nicalon/PyC/HyperSiC Ceramic Composite specimen tested in creep at -22 MPa and 1200 °C in air

Figure 42 – P2-5, Fracture surface of Hi-Nicalon/PyC/HyperSiC Ceramic Composite specimen tested in creep at -16 MPa and 1200 °C in steam

Figure 43 – P8-5, Fracture surface of Hi-Nicalon/PyC/HyperSiC Ceramic Composite specimen tested in creep at -18 MPa and 1200 °C in steam

Figure 44 – P9-3, Fracture surface of Hi-Nicalon/PyC/HyperSiC Ceramic Composite specimen tested in creep at -20 MPa and 1200 °C in steam

Figure 45 – P9-4, Fracture surface of Hi-Nicalon/PyC/HyperSiC Ceramic Composite specimen tested in creep at -22 MPa and 1200 °C in steam

Table 11 - Comparison of fracture surfaces at each stress level

Stress Level	Air	Steam
-16 MPa		
-18 MPa		
-20 MPa	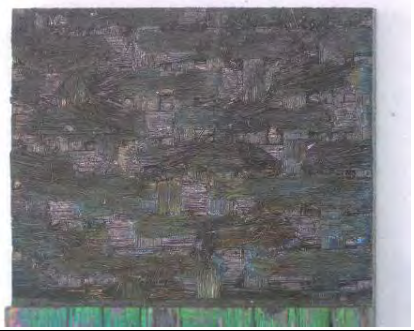	
-22MPa		

Appendix B: Additional SEM Micrographs

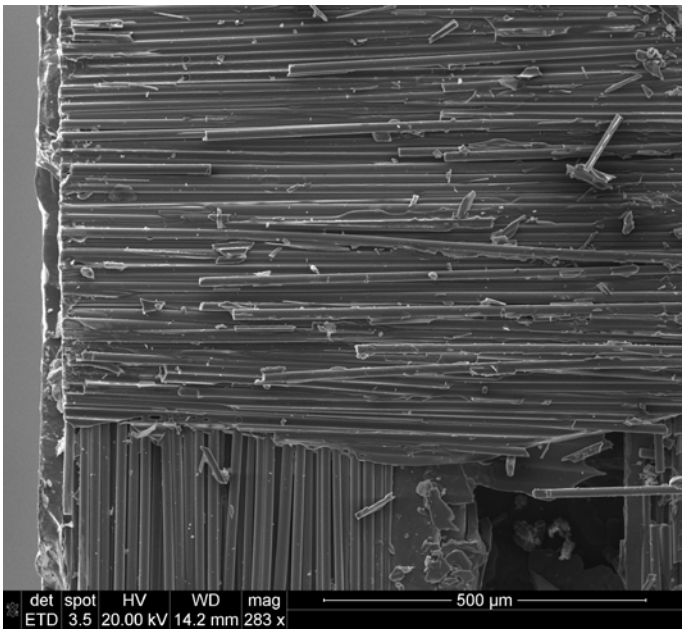

Figure 46 - SEM image showing clean delamination zone of Hi-Nicalon/PyC/HyperSiC Ceramic Composite specimen tested in compression to failure at 1200 °C in air

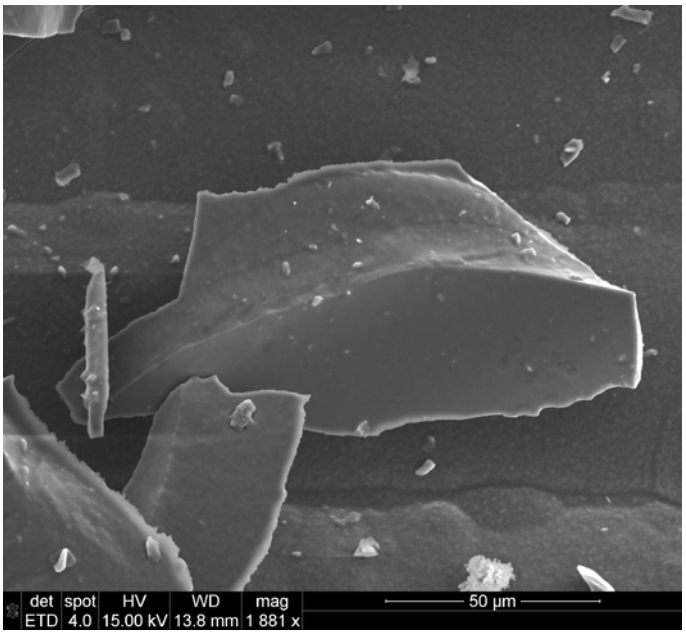

Figure 47 - SEM image showing sharp edges of broken matrix of Hi-Nicalon/PyC/HyperSiC Ceramic Composite specimen tested in compression to failure at 1200 °C in air

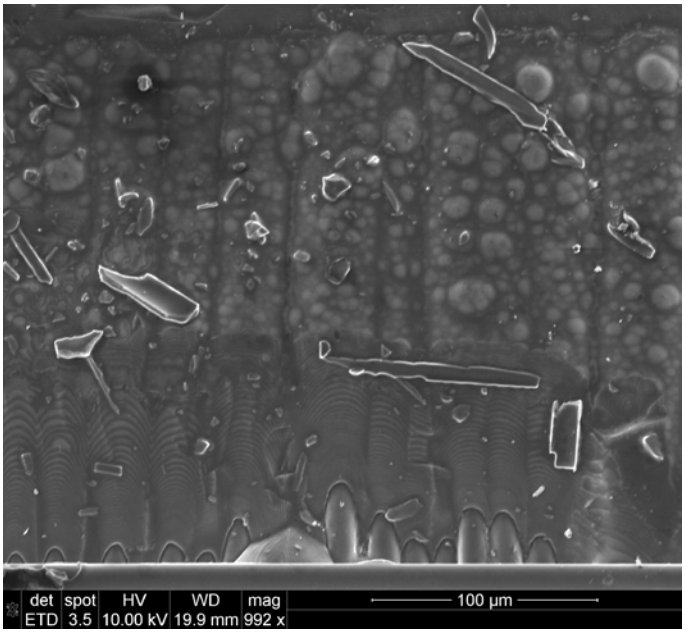

Figure 48 - SEM image showing absence of glass formation on broken matrix of Hi-Nicalon/PyC/HyperSiC Ceramic Composite specimen tested in compression to failure at 1200 °C in air

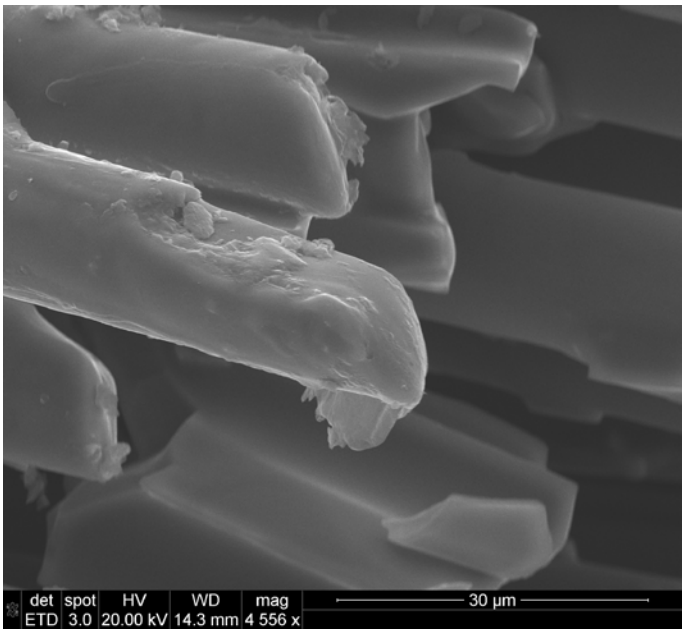

Figure 49 - SEM image showing minimal glass formation on external fiber tip of Hi-Nicalon/PyC/HyperSiC Ceramic Composite specimen tested in compression at 16 MPa at 1200 °C in air

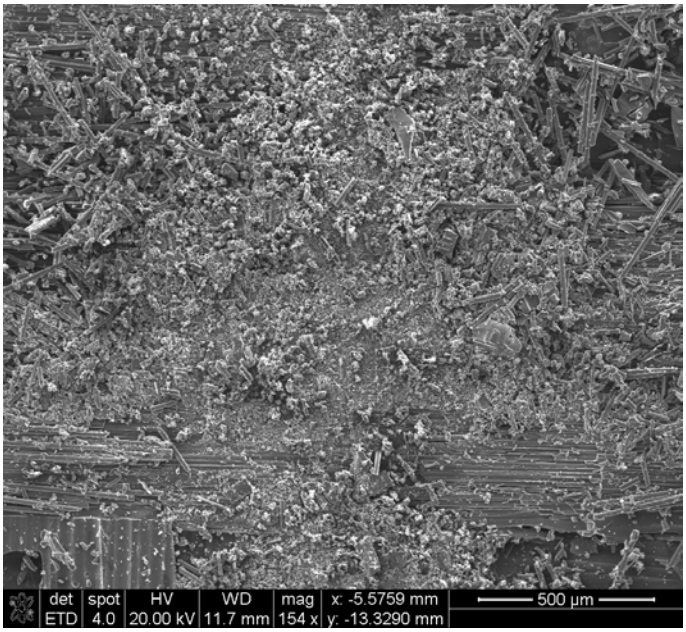

Figure 50 - SEM image showing disintegrated matrix of Hi-Nicalon/PyC/HyperSiC Ceramic Composite specimen tested in compression at 16 MPa at 1200 °C in air

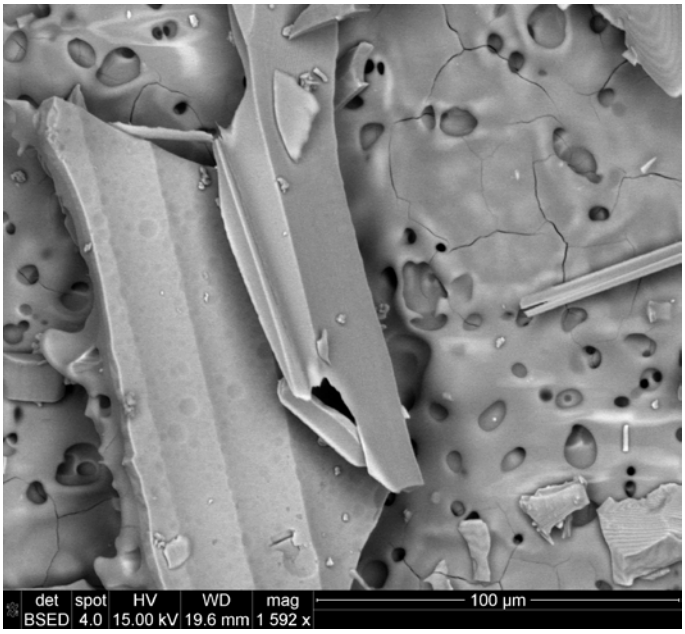

Figure 51 - SEM image showing glass formation of Hi-Nicalon/PyC/HyperSiC Ceramic Composite specimen tested in compression at 16 MPa at 1200 °C in steam

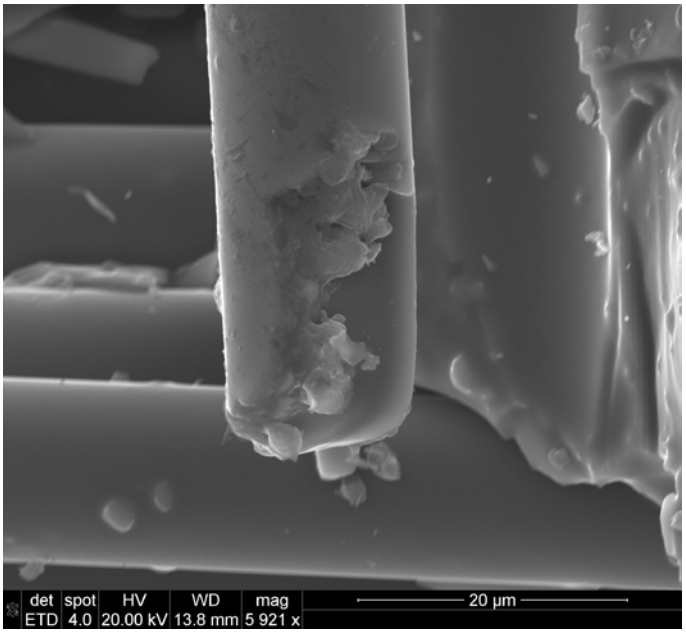

Figure 52 - SEM image showing fractured fiber tip of Hi-Nicalon/PyC/HyperSiC Ceramic Composite specimen tested in compression at 16 MPa at 1200 °C in steam

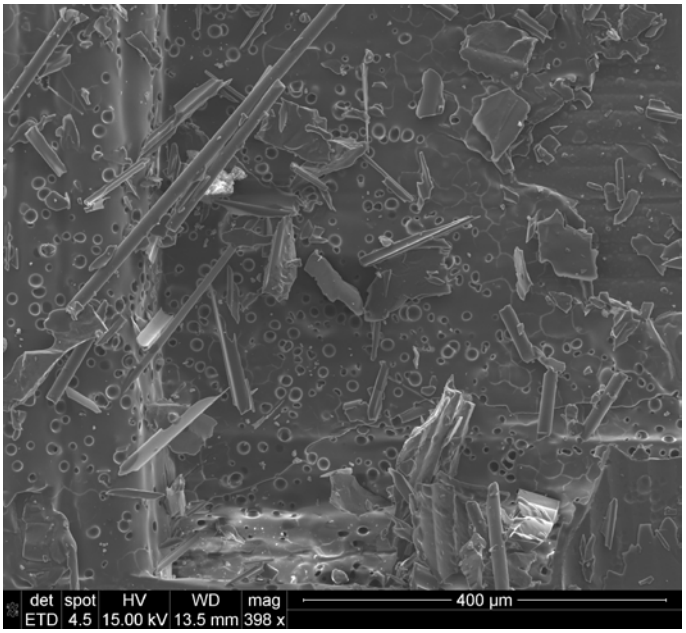

Figure 53 - SEM image showing glass formation of Hi-Nicalon/PyC/HyperSiC Ceramic Composite specimen tested in compression at 16 MPa at 1200 °C in steam

Figure 54 - SEM image showing glass formation of Hi-Nicalon/PyC/HyperSiC Ceramic Composite specimen tested in compression at 16 MPa at 1200 °C in steam

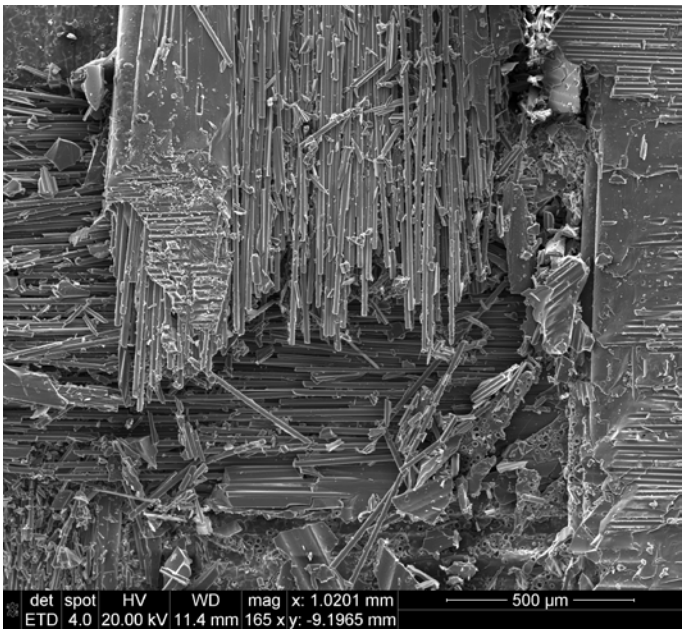

Figure 55 - SEM image showing failed fibers of Hi-Nicalon/PyC/HyperSiC Ceramic Composite specimen tested in compression at 16 MPa at 1200 °C in steam

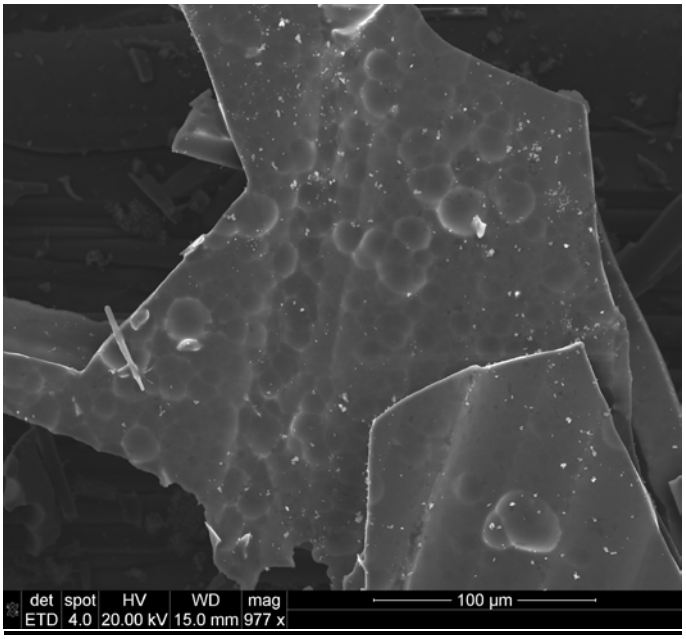

Figure 56 - SEM image showing sharp edges broken matrix of Hi-Nicalon/PyC/HyperSiC Ceramic Composite specimen tested in compression at 18 MPa at 1200 °C in air

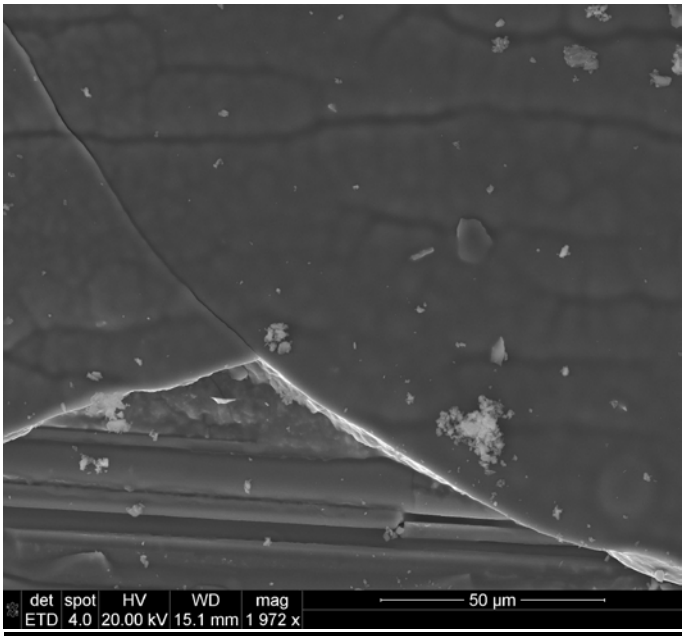

Figure 57 - SEM image showing sharp edges broken matrix of Hi-Nicalon/PyC/HyperSiC Ceramic Composite specimen tested in compression at 18 MPa at 1200 °C in air

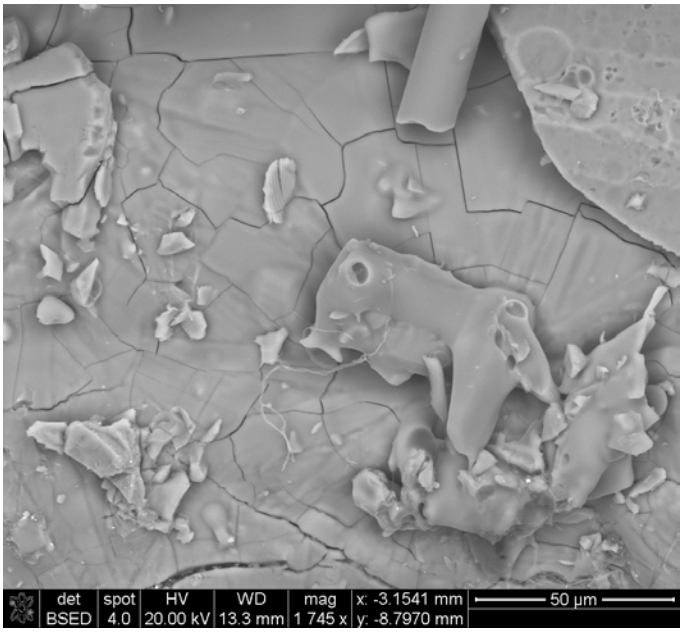

Figure 58 - SEM image showing thick glass formation of Hi-Nicalon/PyC/HyperSiC Ceramic Composite specimen tested in compression at 18 MPa at 1200 °C in steam

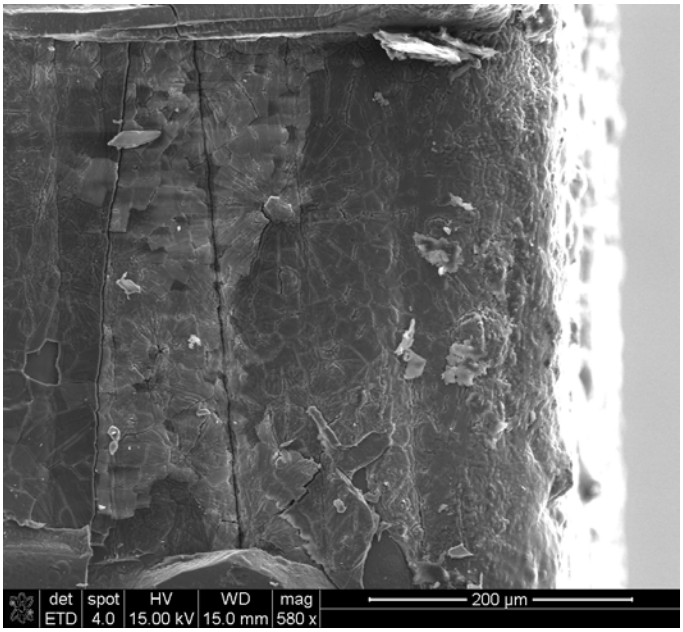

Figure 59 - SEM image showing thick glass formation at specimen edge of Hi-Nicalon/PyC/HyperSiC Ceramic Composite specimen tested in compression at 18 MPa at 1200 °C in steam

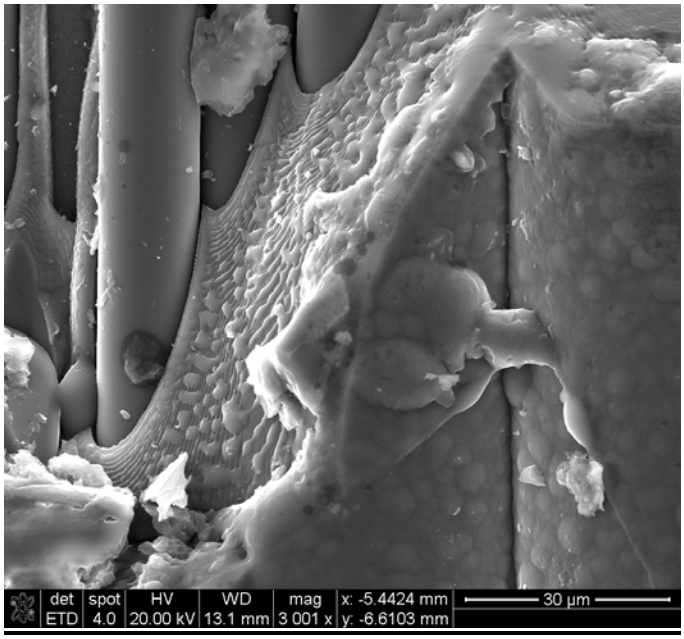

Figure 60 - SEM image showing thick glass formation flowing from fractured matrix of Hi-Nicalon/PyC/HyperSiC Ceramic Composite specimen tested in compression at 18 MPa at 1200 °C in steam

Figure 61 - SEM image showing thick glass formation at matrix void of Hi-Nicalon/PyC/HyperSiC Ceramic Composite specimen tested in compression at 18 MPa at 1200 °C in steam

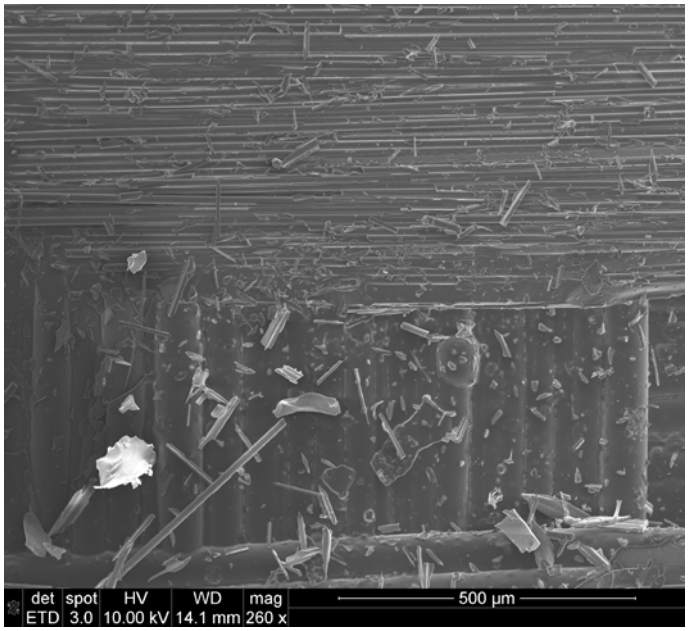

Figure 62 - SEM image showing smooth delamination zone of Hi-Nicalon/PyC/HyperSiC Ceramic Composite specimen tested in compression at 20 MPa at 1200 °C in air

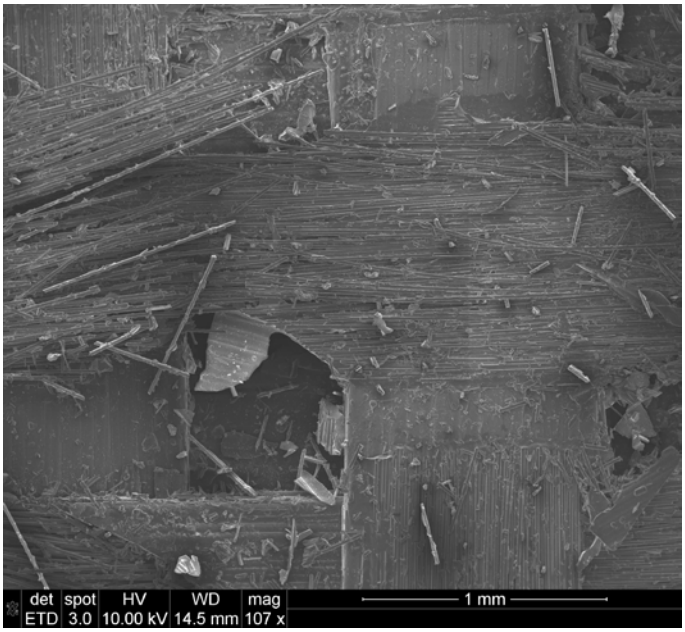

Figure 63 - SEM image showing smooth delamination zone of Hi-Nicalon/PyC/HyperSiC Ceramic Composite specimen tested in compression at 20 MPa at 1200 °C in air

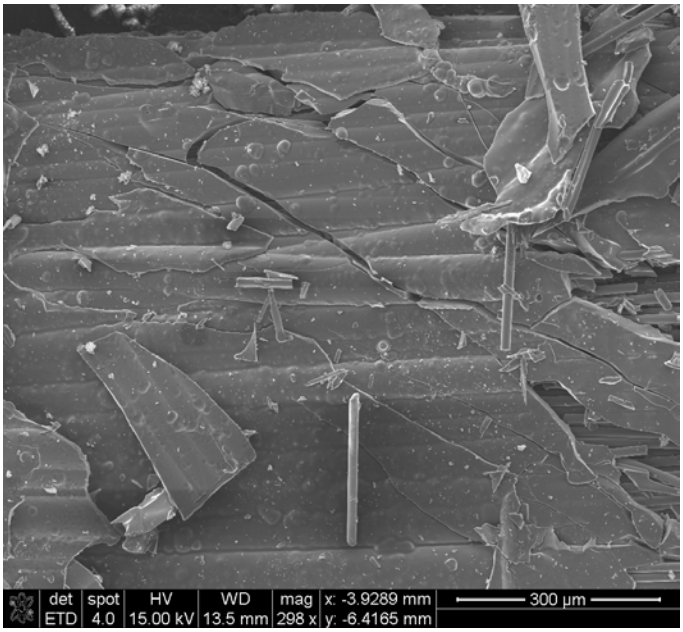

Figure 64 - SEM image showing cracked matrix of Hi-Nicalon/PyC/HyperSiC Ceramic Composite specimen tested in compression at 20 MPa at 1200 °C in air

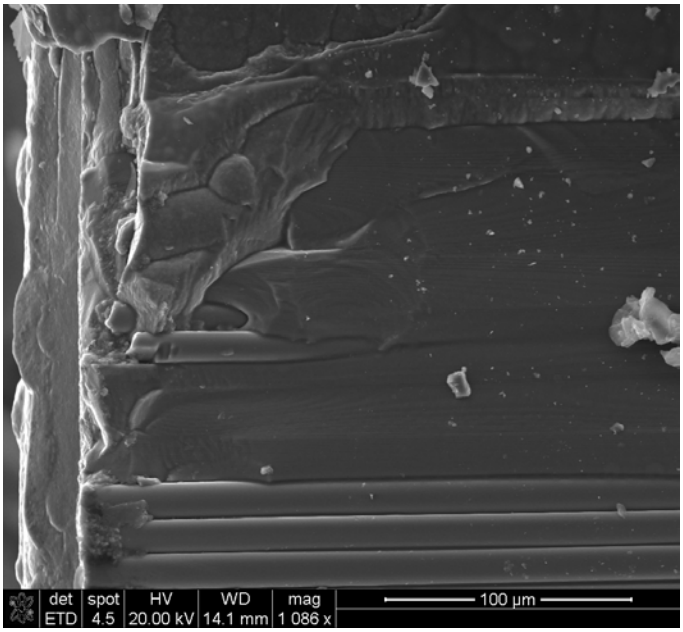

Figure 65 - SEM image showing cracked matrix toward edge of Hi-Nicalon/PyC/HyperSiC Ceramic Composite specimen tested in compression at 20 MPa at 1200 °C in air

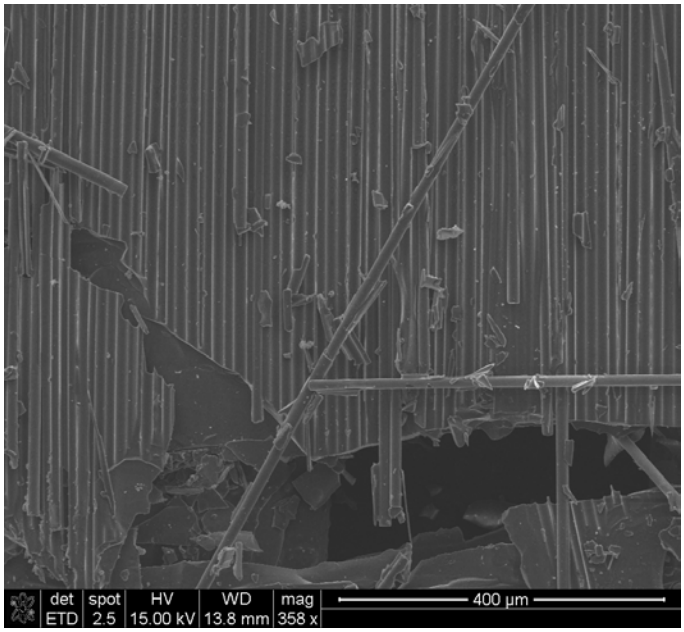

Figure 66 - SEM image showing clean fiber grooves in matrix of Hi-Nicalon/PyC/HyperSiC Ceramic Composite specimen tested in compression at 20 MPa at 1200 °C in air

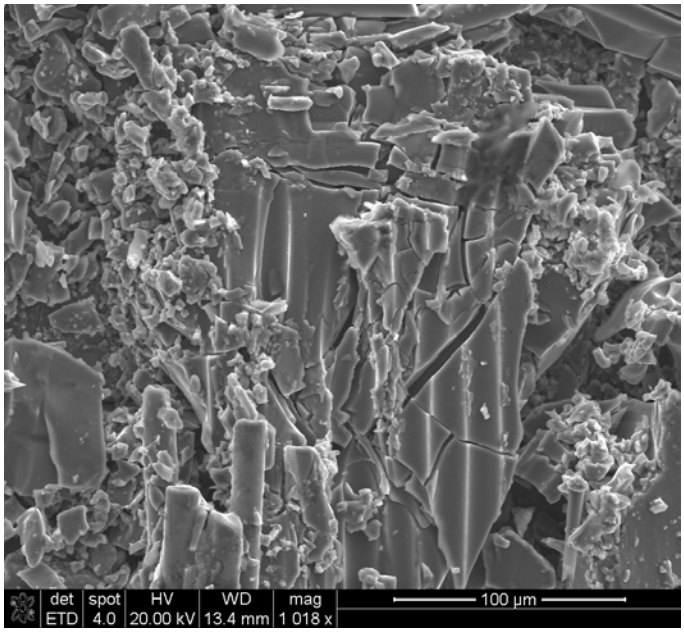

Figure 67 - SEM image showing cracked matrix with intact fiber grooves of Hi-Nicalon/PyC/HyperSiC Ceramic Composite specimen tested in compression at 20 MPa at 1200 °C in air

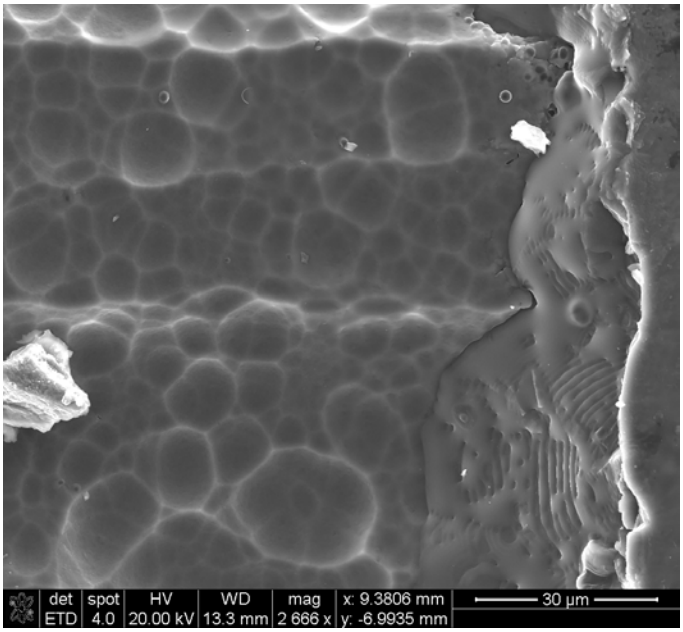

Figure 68 - SEM image showing glass emerging from matrix within matrix crack at edge of Hi-Nicalon/PyC/HyperSiC Ceramic Composite specimen tested in compression at 20 MPa at 1200 °C in steam

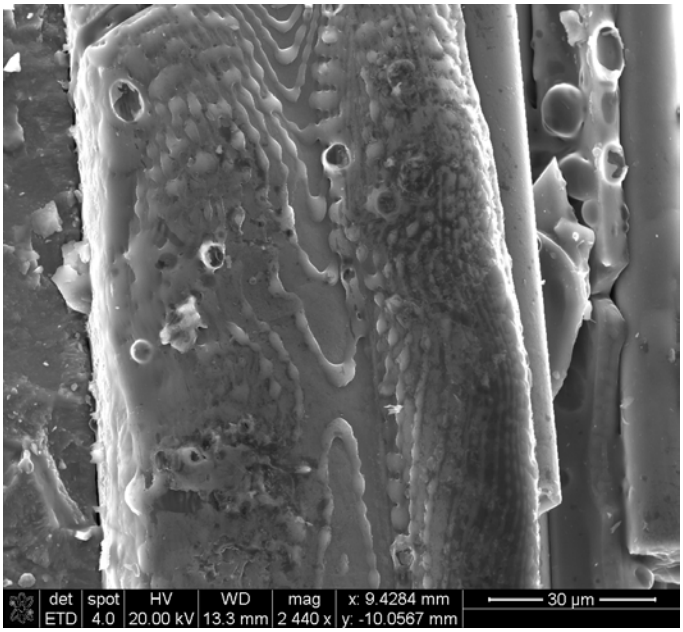

Figure 69 - SEM image showing glass emerging from matrix of Hi-Nicalon/PyC/HyperSiC Ceramic Composite specimen tested in compression at 20 MPa at 1200 °C in steam

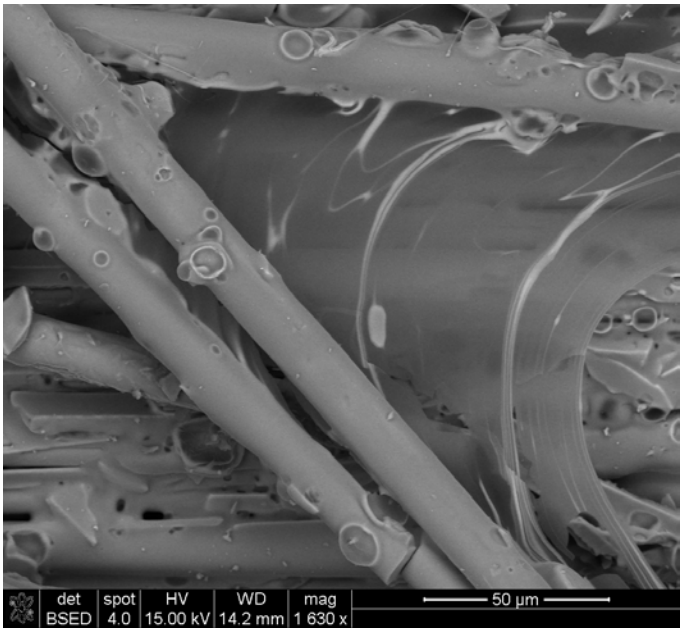

Figure 70 - SEM image showing thin glass film spread between two fibers of Hi-Nicalon/PyC/HyperSiC Ceramic Composite specimen tested in compression at 20 MPa at 1200 °C in steam

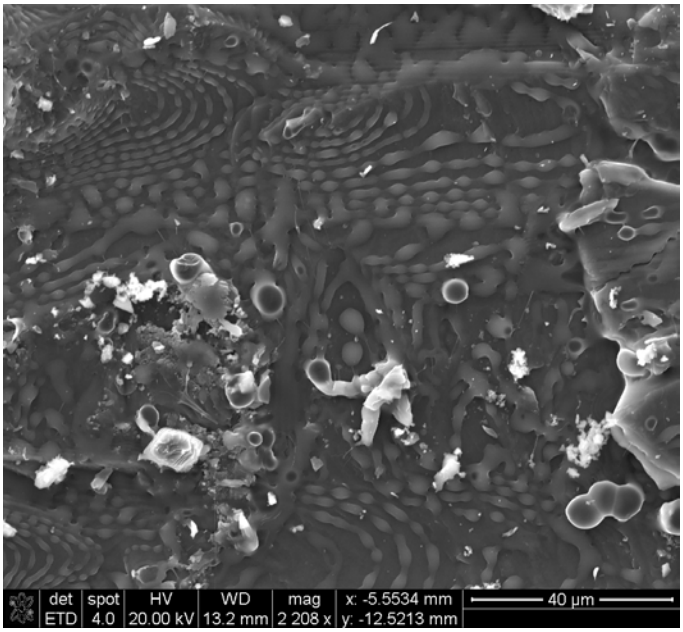

Figure 71 - SEM image showing glass emerging from matrix of Hi-Nicalon/PyC/HyperSiC Ceramic Composite specimen tested in compression at 20 MPa at 1200 °C in steam

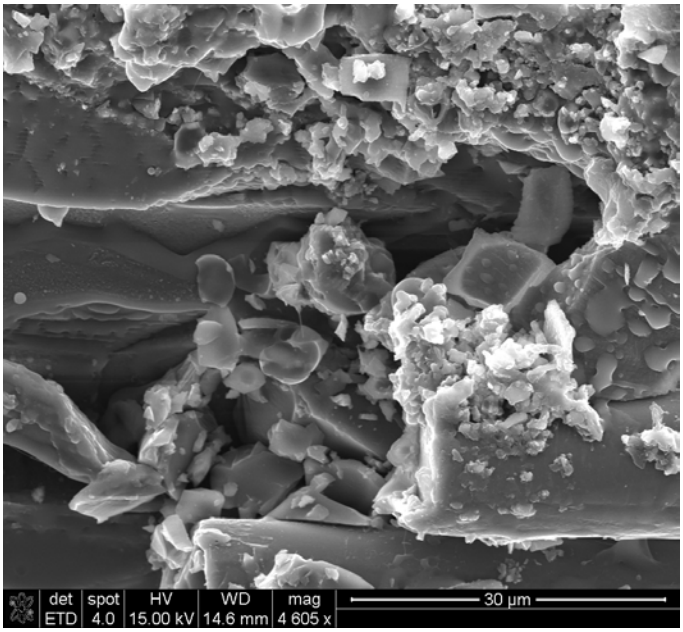

Figure 72 - SEM image showing glass emerging within matrix void of Hi-Nicalon/PyC/HyperSiC Ceramic Composite specimen tested in compression at 20 MPa at 1200 °C in steam

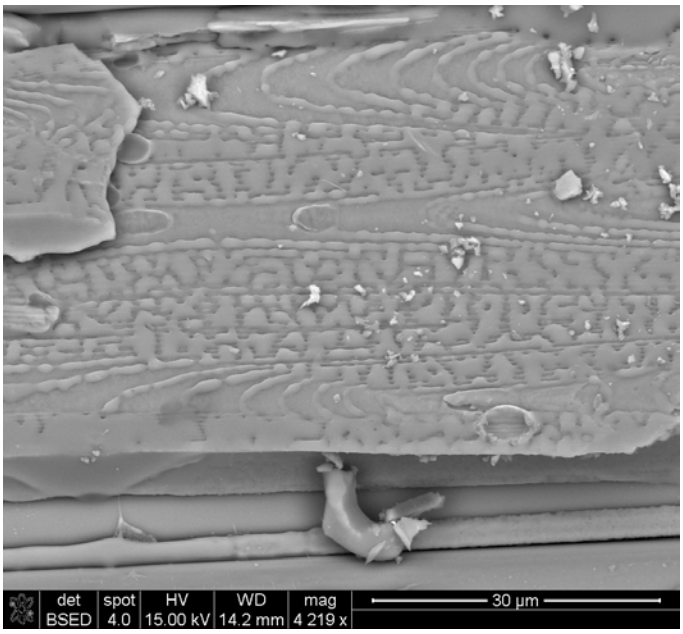

Figure 73 - SEM image showing glass emerging from matrix of Hi-Nicalon/PyC/HyperSiC Ceramic Composite specimen tested in compression at 20 MPa at 1200 °C in steam

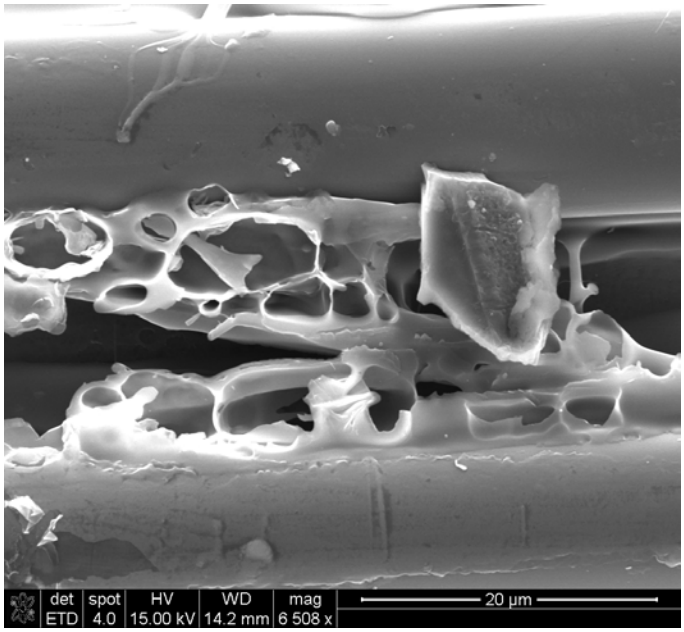

Figure 74 - SEM image showing glass formation between two fibers of Hi-Nicalon/PyC/HyperSiC Ceramic Composite specimen tested in compression at 20 MPa at 1200 °C in steam

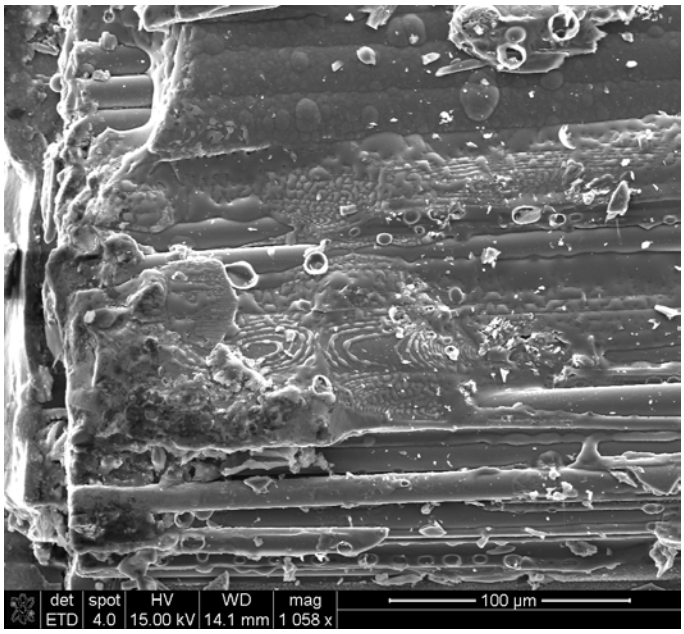

Figure 75 - SEM image showing glass emerging from matrix of Hi-Nicalon/PyC/HyperSiC Ceramic Composite specimen tested in compression at 20 MPa at 1200 °C in steam

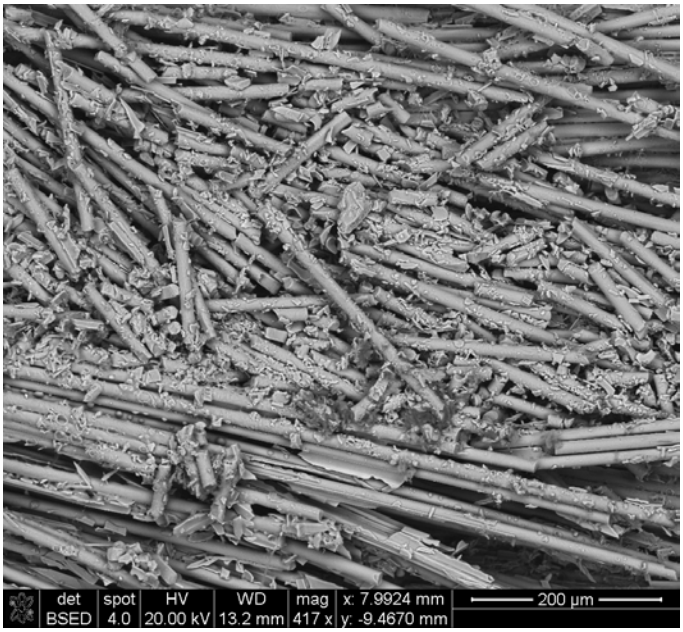

Figure 76 - SEM image showing fractured fibers bound with glass and matrix of Hi-Nicalon/PyC/HyperSiC Ceramic Composite specimen tested in compression at 20 MPa at 1200 °C in steam

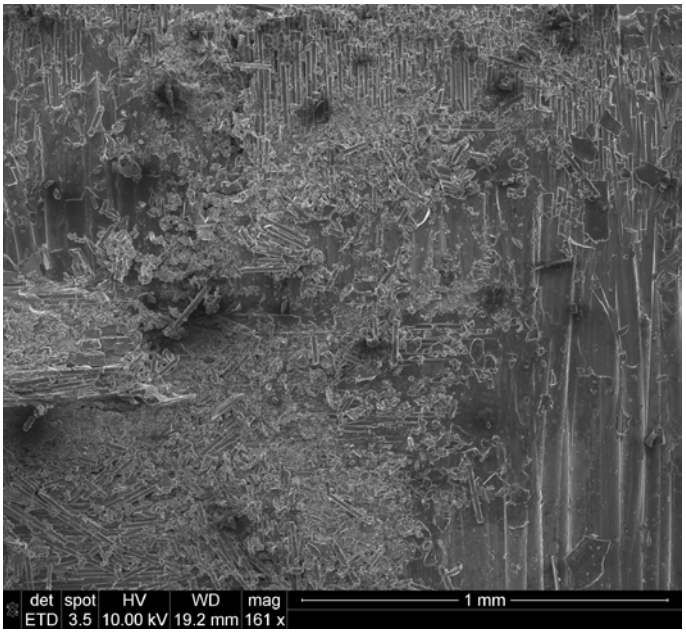

Figure 77 - SEM image showing delamination zone with minimal debris of Hi-Nicalon/PyC/HyperSiC Ceramic Composite specimen tested in compression at 22 MPa at 1200 °C in air

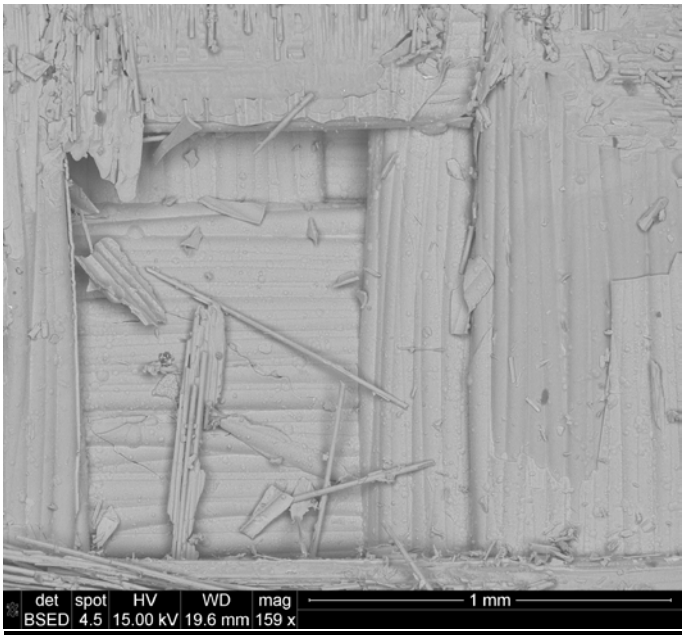

Figure 78 - SEM image showing clean delamination zone and void of Hi-Nicalon/PyC/HyperSiC Ceramic Composite specimen tested in compression at 22 MPa at 1200 °C in air

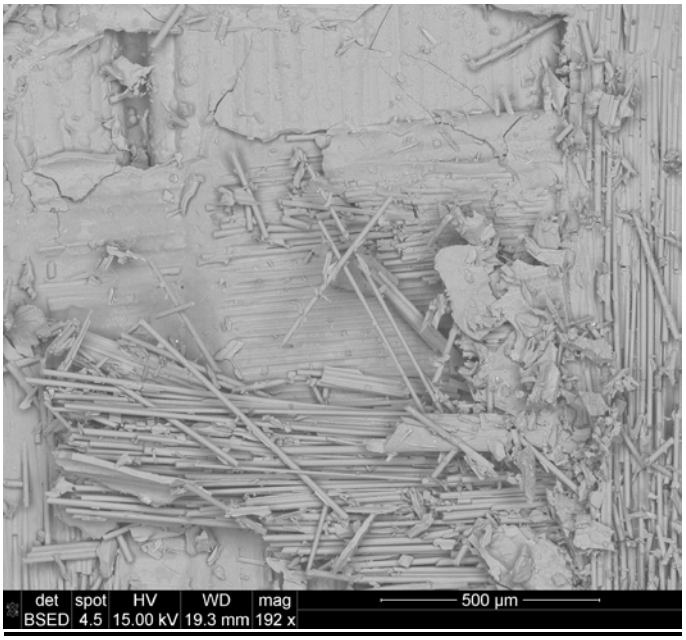

Figure 79 - SEM image showing delamination zone with debris of Hi-Nicalon/PyC/HyperSiC Ceramic Composite specimen tested in compression at 22 MPa at 1200 °C in air

Figure 80 - SEM image showing delamination zone with minimal debris of Hi-Nicalon/PyC/HyperSiC Ceramic Composite specimen tested in compression at 22 MPa at 1200 °C in air

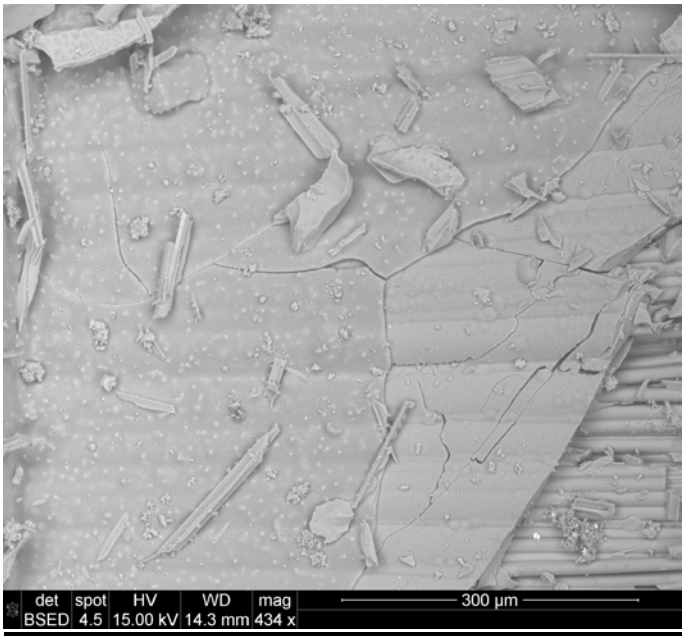

Figure 81 - SEM image showing smooth cracked matrix of Hi-Nicalon/PyC/HyperSiC Ceramic Composite specimen tested in compression at 22 MPa at 1200 °C in air

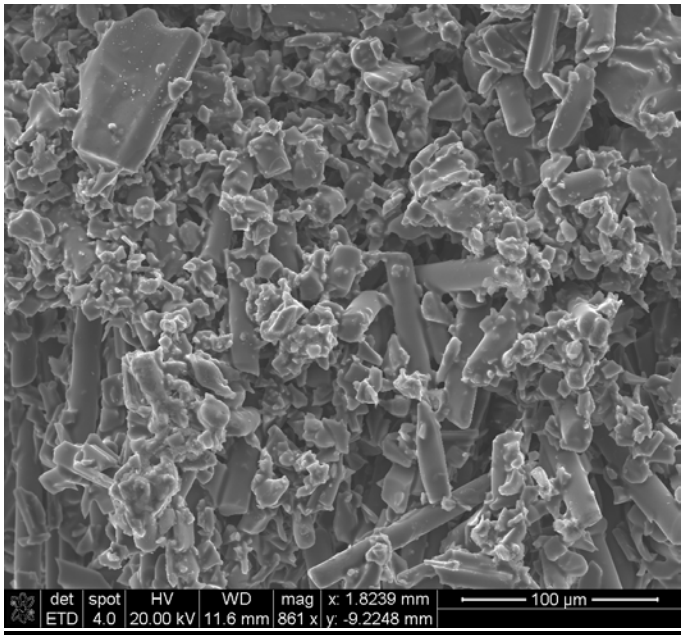

Figure 82 - SEM image showing surface debris of Hi-Nicalon/PyC/HyperSiC Ceramic Composite specimen tested in compression at 22 MPa at 1200 °C in air

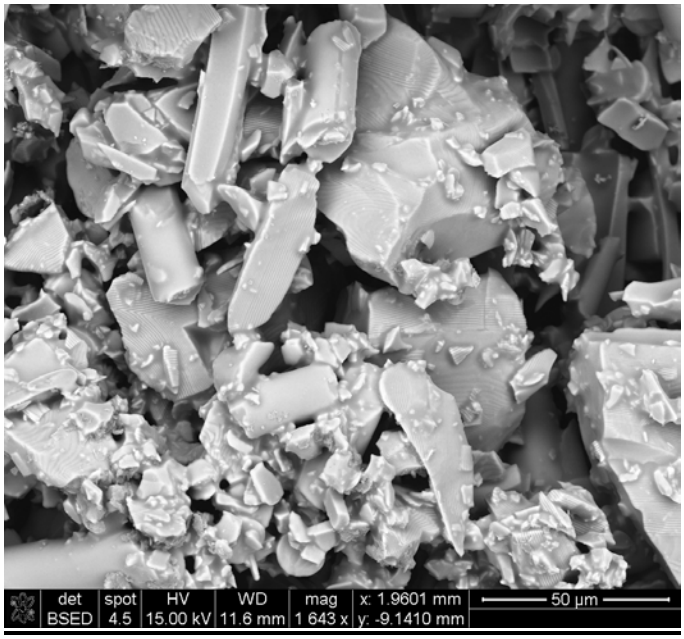

Figure 83 - SEM image showing clear matrix layers within debris of Hi-Nicalon/PyC/HyperSiC Ceramic Composite specimen tested in compression at 22 MPa at 1200 °C in air

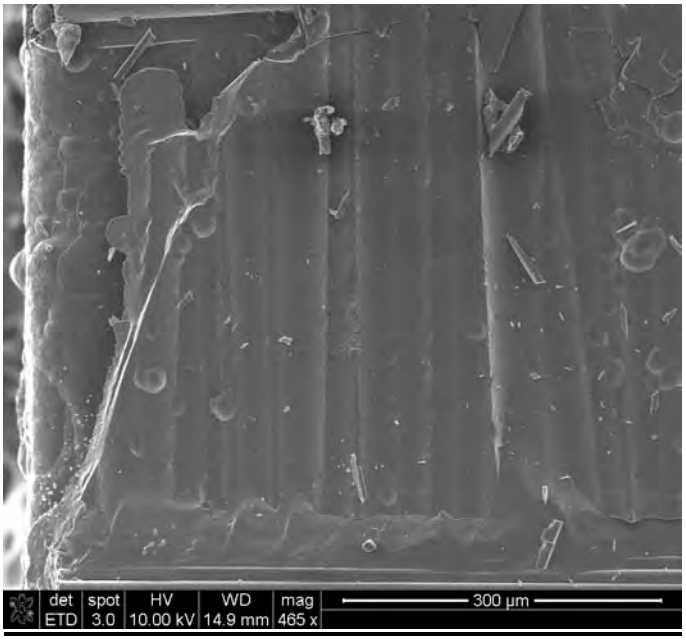

Figure 84 - SEM image showing delamination zone with intact matrix of Hi-Nicalon/PyC/HyperSiC Ceramic Composite specimen tested in compression at 22 MPa at 1200 °C in steam

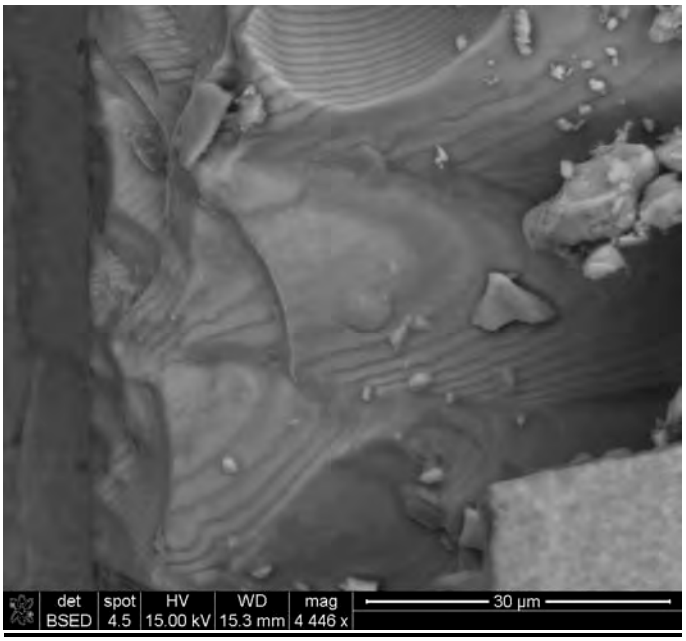

Figure 85 - SEM image showing delamination zone cracked matrix of Hi-Nicalon/PyC/HyperSiC Ceramic Composite specimen tested in compression at 22 MPa at 1200 °C in steam

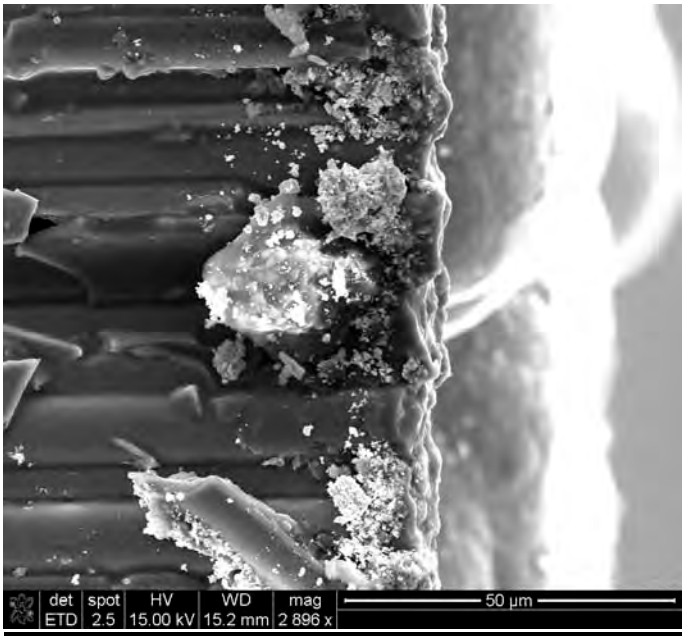

Figure 86 - SEM image showing beginning of glass formation at edge of Hi-Nicalon/PyC/HyperSiC Ceramic Composite specimen tested in compression at 22 MPa at 1200 °C in steam

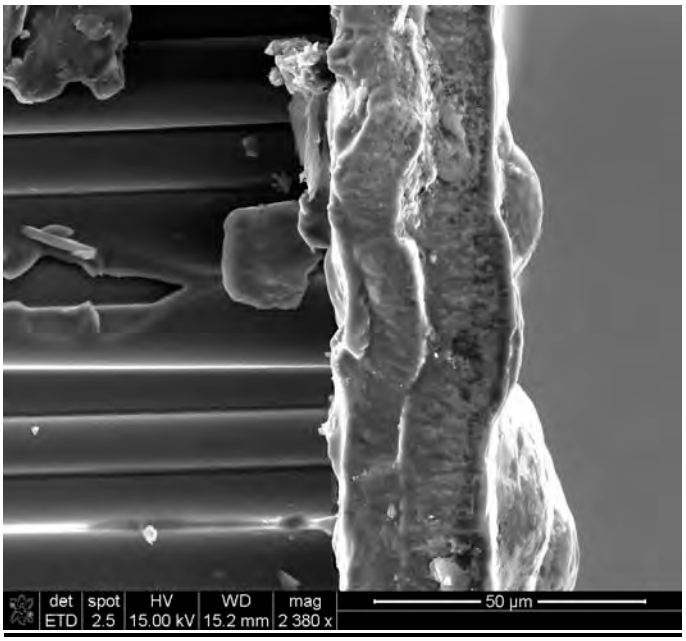

Figure 87 - SEM image showing beginning of glass formation at edge of Hi-Nicalon/PyC/HyperSiC Ceramic Composite specimen tested in compression at 22 MPa at 1200 °C in steam

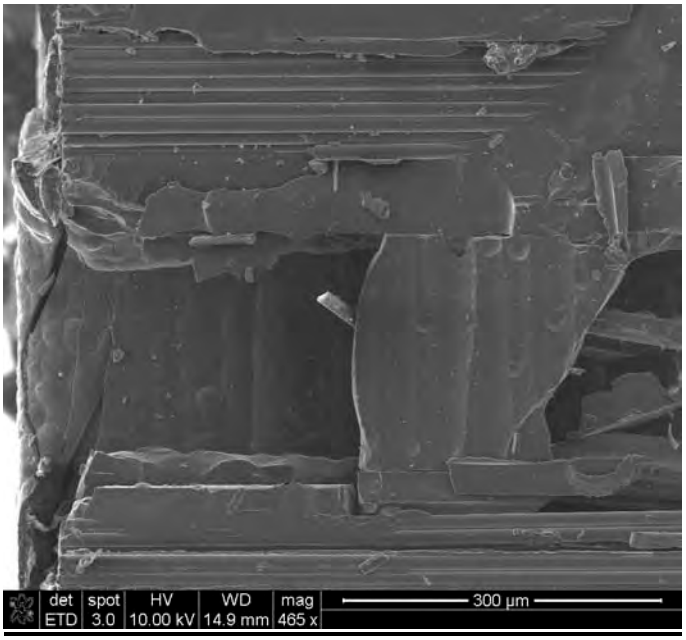

Figure 88 - SEM image showing cracked matrix without glass formation at edge of Hi-Nicalon/PyC/HyperSiC Ceramic Composite specimen tested in compression at 22 MPa at 1200 °C in steam

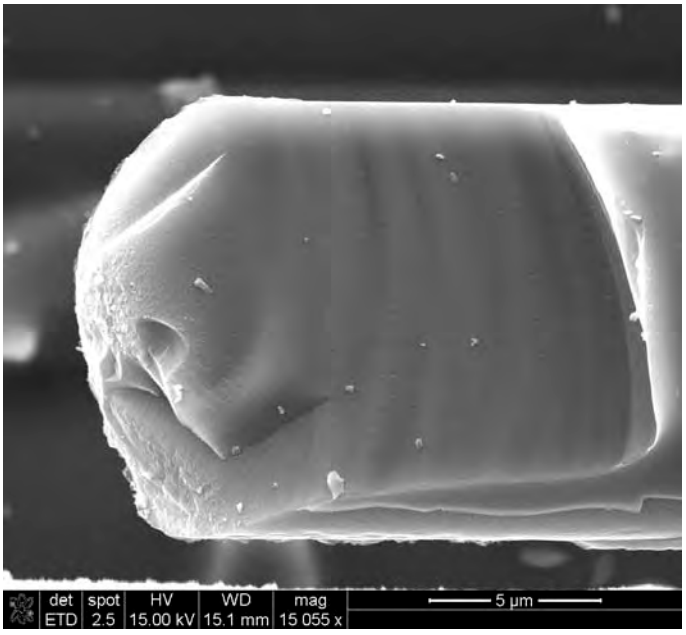

Figure 89 - SEM image showing fractured fiber of Hi-Nicalon/PyC/HyperSiC Ceramic Composite specimen tested in compression at 22 MPa at 1200 °C in steam

VI. Conclusions and Recommendations

Creep behavior in interlaminar shear was examined to characterize of a Hi-Nicalon/PyC/HyperSiC ceramic composite in both air and steam environments at 1200°C.

Compression testing to failure was conducted to obtain the as-processed interlaminar shear strength of 27.2 MPa and an average failure strain of 0.149%. Compressive creep behavior at 1200°C in both air and steam was evaluated for interlaminar shear stresses ranging from 16 to 22 MPa. At a compressive creep stress level of 16 MPa (~59% ILSS), the specimen achieved run-out of 100 hours at 1200°C in both air and steam.

The presence of steam generally decreased interlaminar shear performance of the SiC/SiC composite at stress levels above 16 MPa. At 18 MPa (~66% ILSS), steam decreased creep life by ~12% and increased strain by ~0.17%. At 20 MPa (~74% ILSS), the presence of steam decreased creep life by ~28% and increased strain by ~0.13%. However, at 22 MPa (~80% ILSS), the presence of steam actually increased creep life by ~123% and increased strain by ~0.06% above that observed in air.

The specimen pre-crept in steam strained to 0.170% and only retained 75% ILSS, whereas the specimen pre-crept in air strained to only 0.068% and retained 96% of the as-processed ILSS. The retained ILSS of the run-out specimen in air was only 4% less than the as-processed ILSS but the strain for the specimen pre-crept in air (0.068%) was significantly less than the as-processed material (0.149%), indicating that specimen pre-crept for 100 hours in air had a better creep resistance than the as-processed material.

Future efforts in characterizing this material should expand upon the data set given here by repeating the experiments at each stress in order to develop a level of confidence in creep lifetimes reported at given stress levels.

Investigation of both rate dependence and tensile ILS behavior would also yield important information required to further characterize this material.

Finally, the use of TEM to investigate changes in grain size might shed further light on how changes in grain size may affect creep life.

Appendix A: Additional Optical Micrographs

Figure 90 – P6-3, Fracture surface of Hi-Nicalon/PyC/HyperSiC Ceramic Composite specimen tested in compression to failure at 1200 °C in air

Figure 91 – P8-1, Fracture surface of Hi-Nicalon/PyC/HyperSiC Ceramic Composite specimen tested in compression to failure at 1200 °C in air

Figure 92 – P2-3, Fracture surface of Hi-Nicalon/PyC/HyperSiC Ceramic Composite specimen tested in compression to failure at 1200 °C in air

Figure 93 – P9-1, Fracture surface of Hi-Nicalon/PyC/HyperSiC Ceramic Composite specimen tested in compression to failure at 1200 °C in air

Figure 94 – P6-4, Fracture surface of Hi-Nicalon/PyC/HyperSiC Ceramic Composite specimen tested in creep at -16 MPa and 1200 °C in air

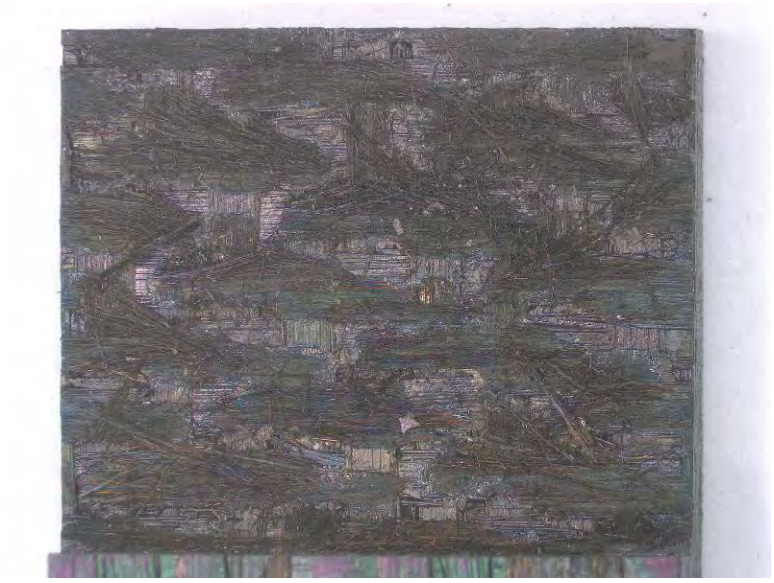

Figure 95 – P9-2, Fracture surface of Hi-Nicalon/PyC/HyperSiC Ceramic Composite specimen tested in creep at -18 MPa and 1200 °C in air

Figure 96 – P8-4, Fracture surface of Hi-Nicalon/PyC/HyperSiC Ceramic Composite specimen tested in creep at -20 MPa and 1200 °C in air

Figure 97 – P2-6, Fracture surface of Hi-Nicalon/PyC/HyperSiC Ceramic Composite specimen tested in creep at -22 MPa and 1200 °C in air

Figure 98 – P2-5, Fracture surface of Hi-Nicalon/PyC/HyperSiC Ceramic Composite specimen tested in creep at -16 MPa and 1200 °C in steam

Figure 99 – P8-5, Fracture surface of Hi-Nicalon/PyC/HyperSiC Ceramic Composite specimen tested in creep at -18 MPa and 1200 °C in steam

Figure 100 – P9-3, Fracture surface of Hi-Nicalon/PyC/HyperSiC Ceramic Composite specimen tested in creep at -20 MPa and 1200 °C in steam

Figure 101 – P9-4, Fracture surface of Hi-Nicalon/PyC/HyperSiC Ceramic Composite specimen tested in creep at -22 MPa and 1200 °C in steam

Appendix B: Additional SEM Micrographs

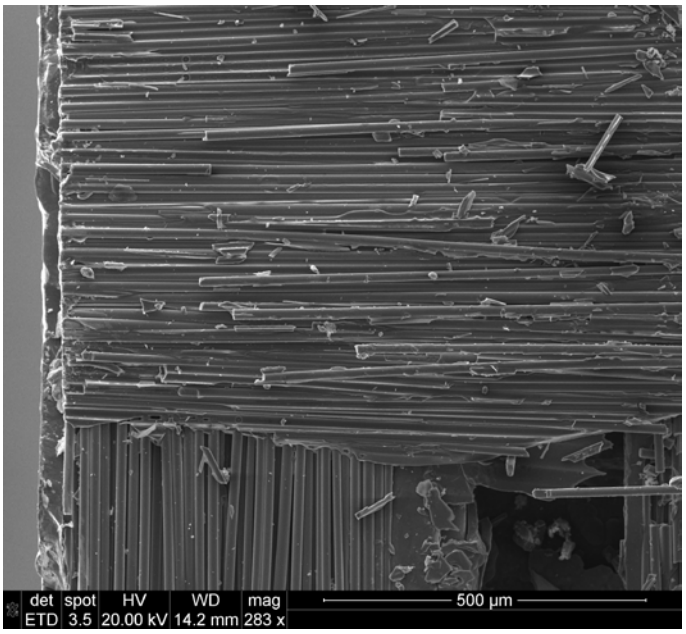

Figure 102 - SEM image showing clean delamination zone of Hi-Nicalon/PyC/HyperSiC Ceramic Composite specimen tested in compression to failure at 1200 °C in air

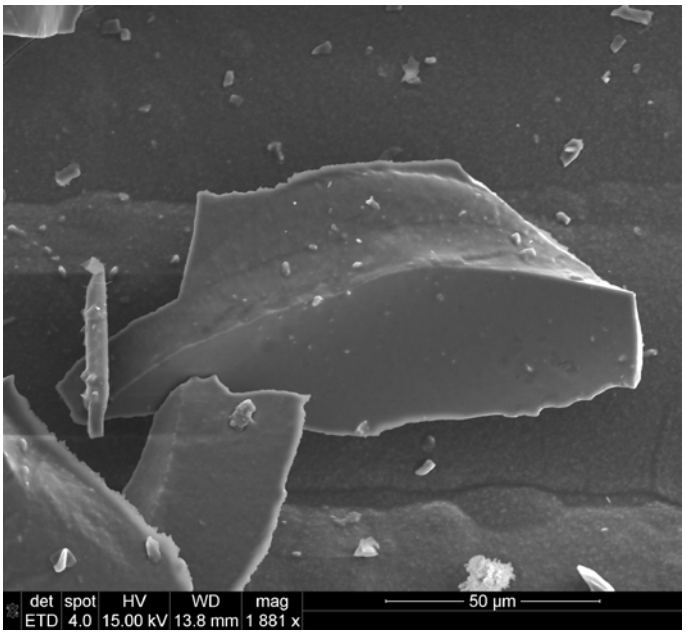

Figure 103 - SEM image showing sharp edges of broken matrix of Hi-Nicalon/PyC/HyperSiC Ceramic Composite specimen tested in compression to failure at 1200 °C in air

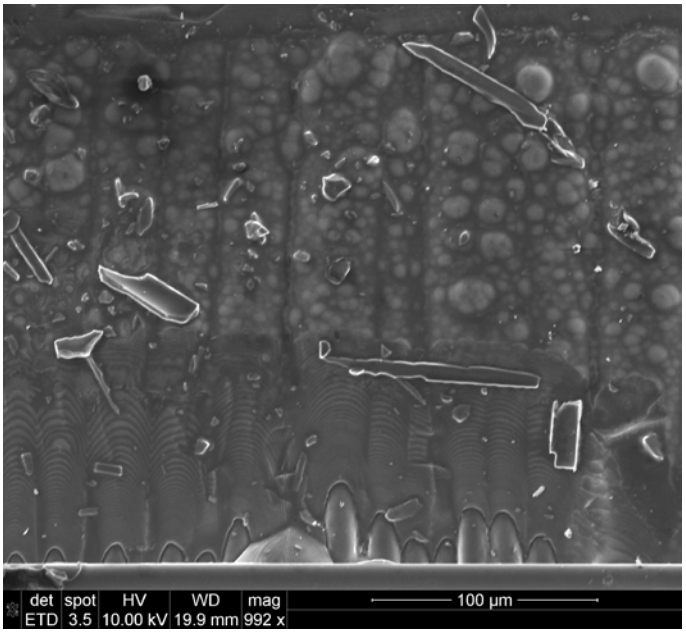

Figure 104 - SEM image showing absence of glass formation on broken matrix of Hi-Nicalon/PyC/HyperSiC Ceramic Composite specimen tested in compression to failure at 1200 °C in air

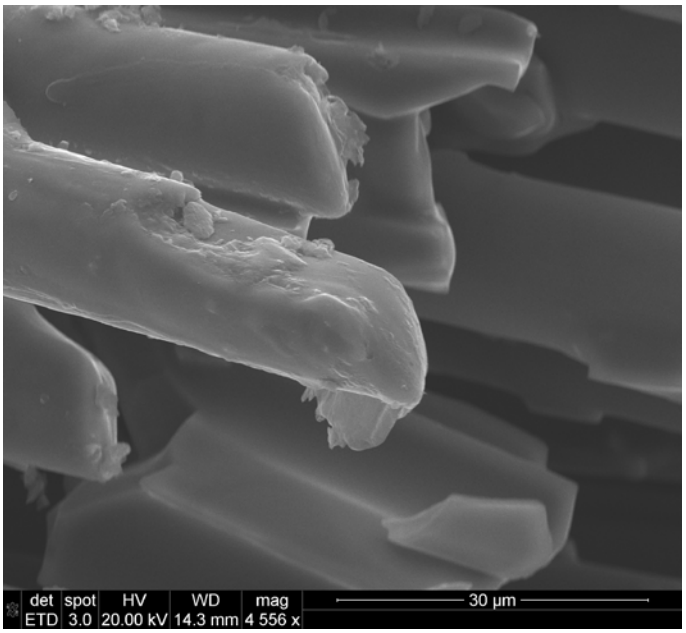

Figure 105 - SEM image showing minimal glass formation on external fiber tip of Hi-Nicalon/PyC/HyperSiC Ceramic Composite specimen tested in compression at 16 MPa at 1200 °C in air

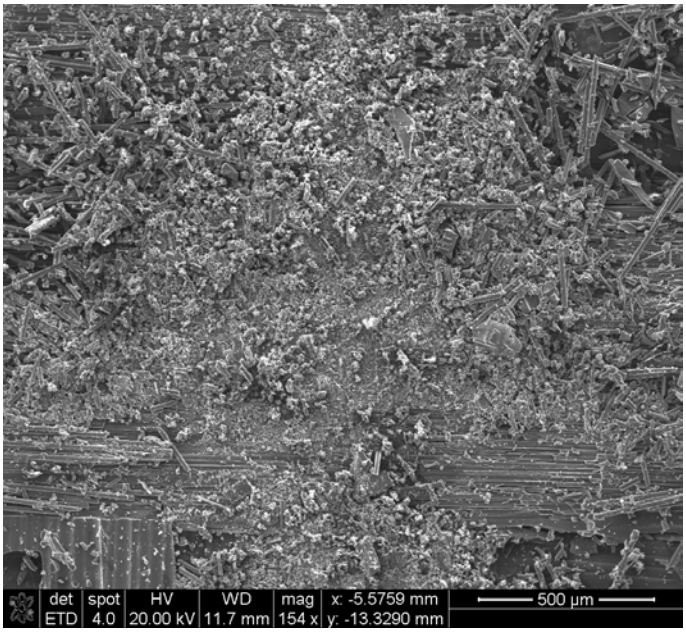

Figure 106 - SEM image showing disintegrated matrix of Hi-Nicalon/PyC/HyperSiC Ceramic Composite specimen tested in compression at 16 MPa at 1200 °C in air

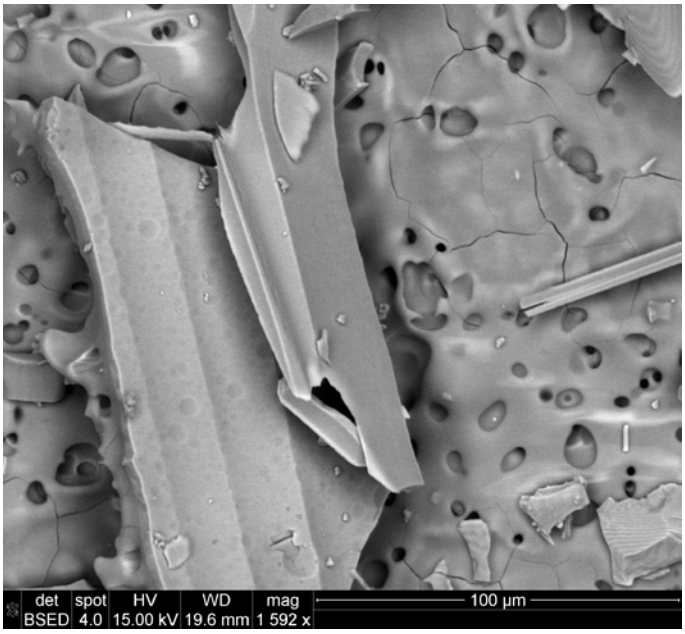

Figure 107 - SEM image showing glass formation of Hi-Nicalon/PyC/HyperSiC Ceramic Composite specimen tested in compression at 16 MPa at 1200 °C in steam

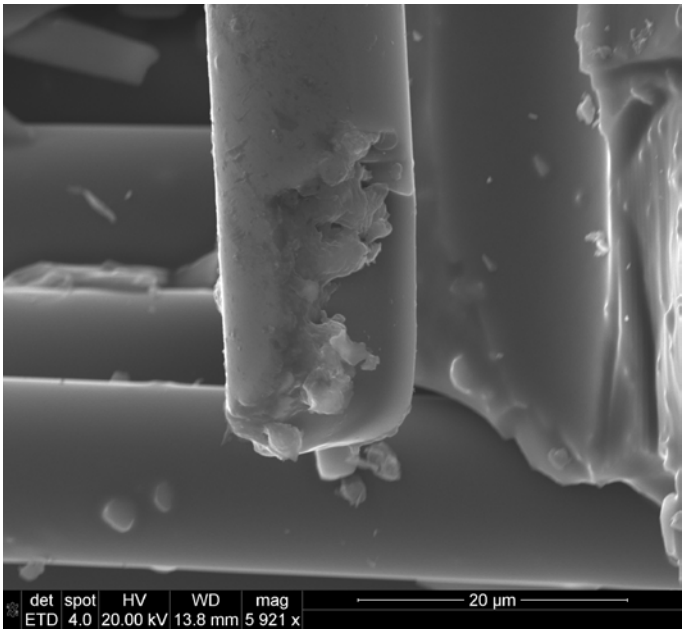

Figure 108 - SEM image showing fractured fiber tip of Hi-Nicalon/PyC/HyperSiC Ceramic Composite specimen tested in compression at 16 MPa at 1200 °C in steam

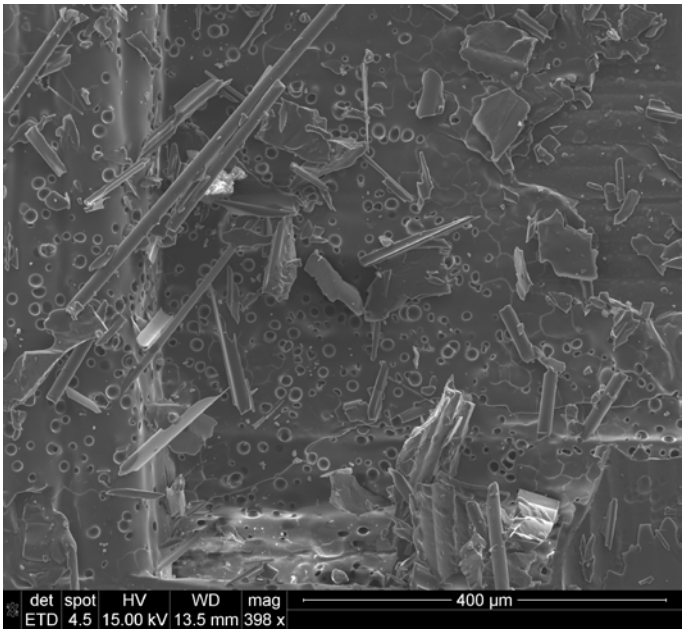

Figure 109 - SEM image showing glass formation of Hi-Nicalon/PyC/HyperSiC Ceramic Composite specimen tested in compression at 16 MPa at 1200 °C in steam

Figure 110 - SEM image showing glass formation of Hi-Nicalon/PyC/HyperSiC Ceramic Composite specimen tested in compression at 16 MPa at 1200 °C in steam

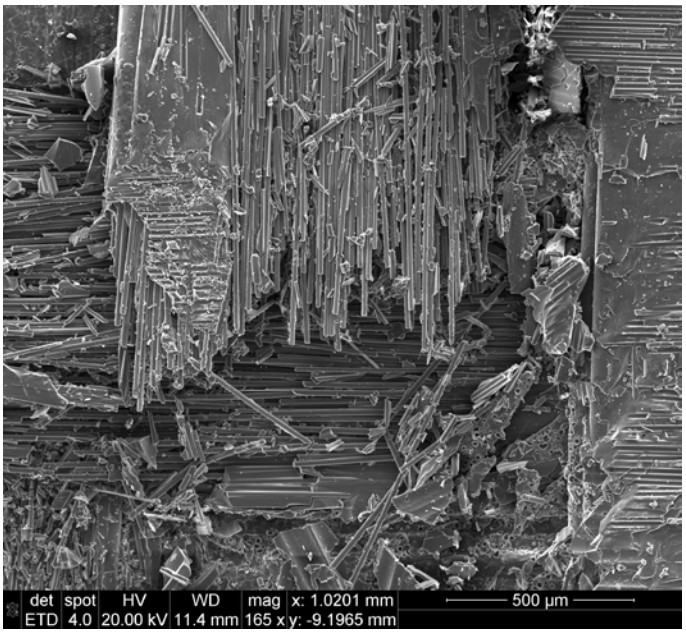

Figure 111 - SEM image showing failed fibers of Hi-Nicalon/PyC/HyperSiC Ceramic Composite specimen tested in compression at 16 MPa at 1200 °C in steam

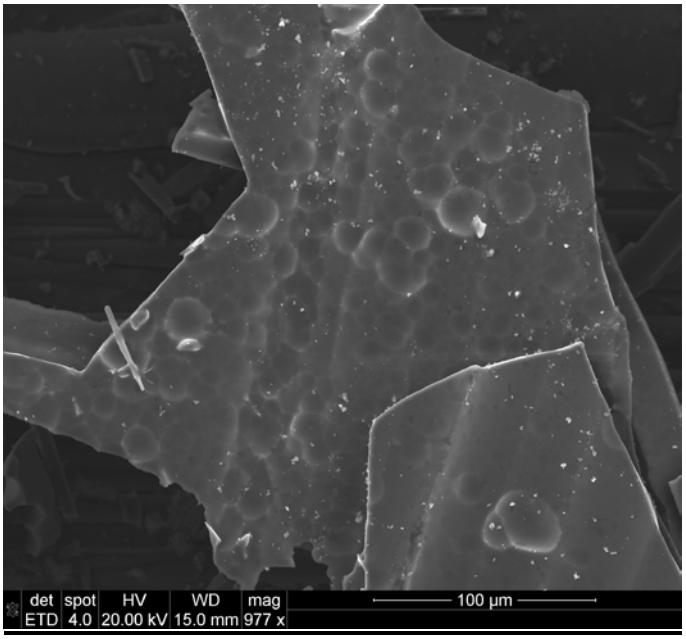

Figure 112 - SEM image showing sharp edges broken matrix of Hi-Nicalon/PyC/HyperSiC Ceramic Composite specimen tested in compression at 18 MPa at 1200 °C in air

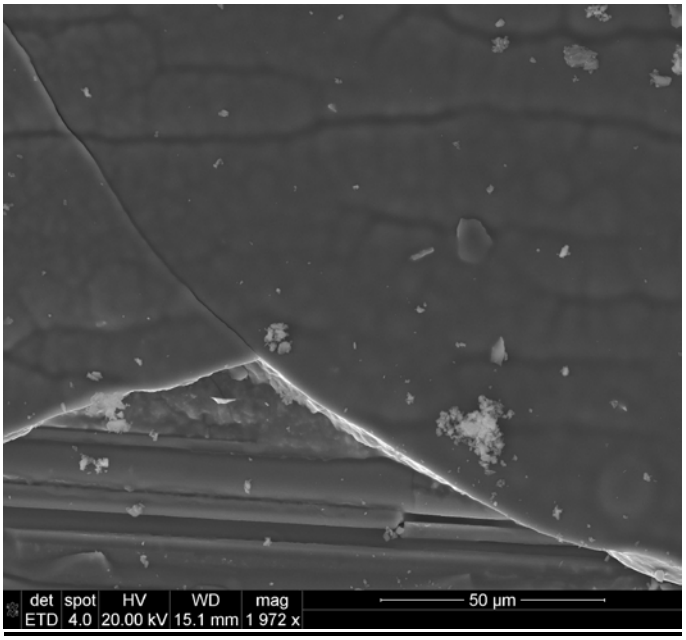

Figure 113 - SEM image showing sharp edges broken matrix of Hi-Nicalon/PyC/HyperSiC Ceramic Composite specimen tested in compression at 18 MPa at 1200 °C in air

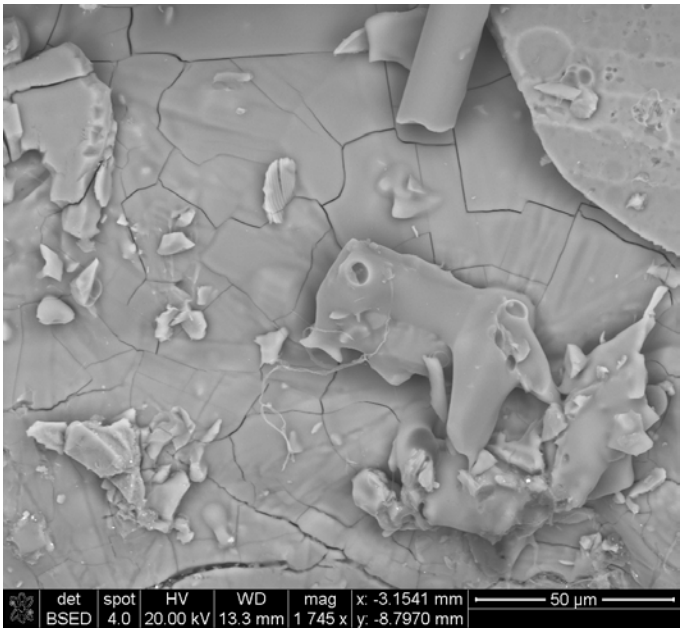

Figure 114 - SEM image showing thick glass formation of Hi-Nicalon/PyC/HyperSiC Ceramic Composite specimen tested in compression at 18 MPa at 1200 °C in steam

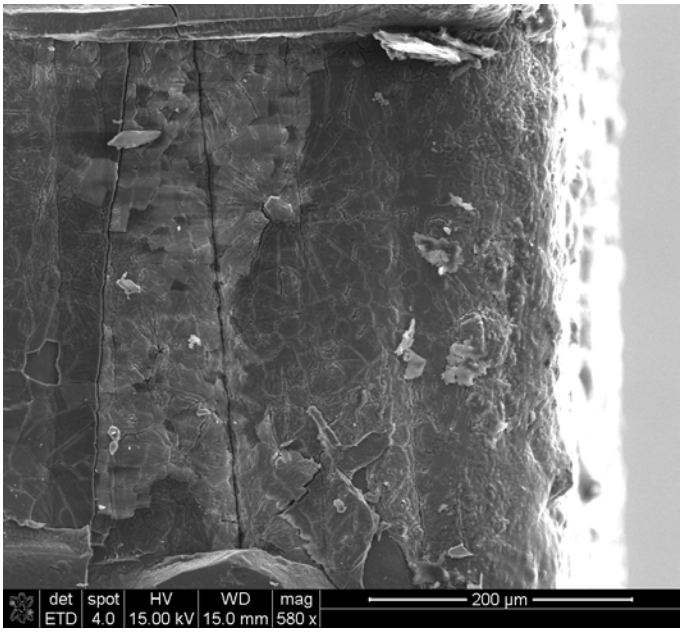

Figure 115 - SEM image showing thick glass formation at specimen edge of Hi-Nicalon/PyC/HyperSiC Ceramic Composite specimen tested in compression at 18 MPa at 1200 °C in steam

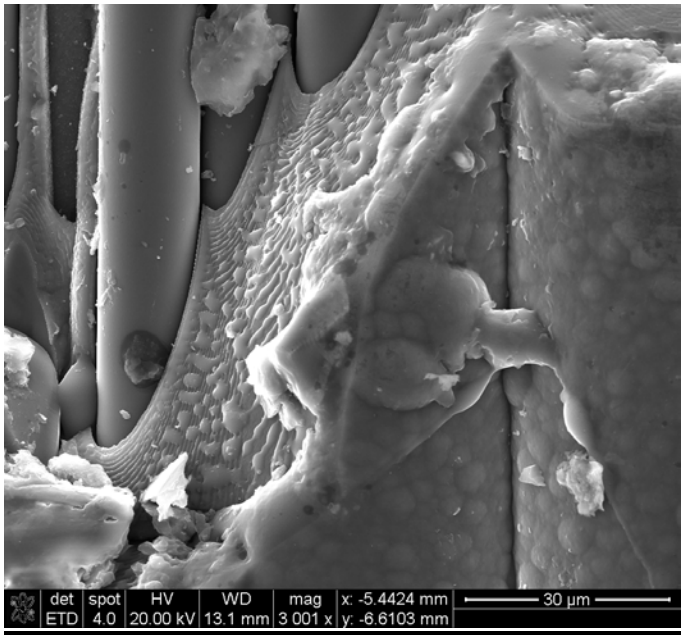

Figure 116 - SEM image showing thick glass formation flowing from fractured matrix of Hi-Nicalon/PyC/HyperSiC Ceramic Composite specimen tested in compression at 18 MPa at 1200 °C in steam

Figure 117 - SEM image showing thick glass formation at matrix void of Hi-Nicalon/PyC/HyperSiC Ceramic Composite specimen tested in compression at 18 MPa at 1200 °C in steam

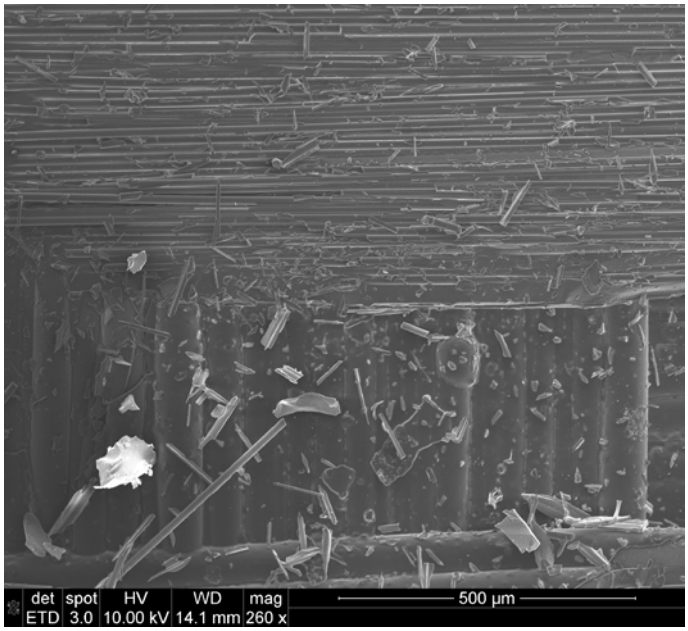

Figure 118 - SEM image showing smooth delamination zone of Hi-Nicalon/PyC/HyperSiC Ceramic Composite specimen tested in compression at 20 MPa at 1200 °C in air

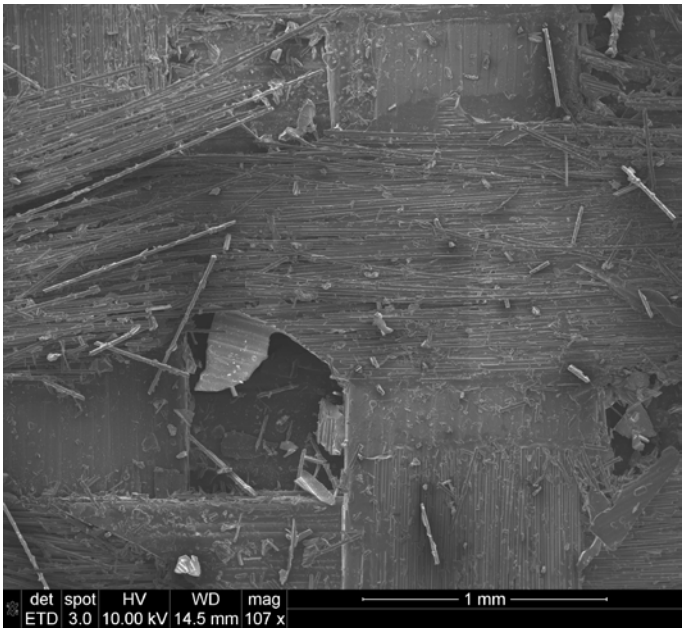

Figure 119 - SEM image showing smooth delamination zone of Hi-Nicalon/PyC/HyperSiC Ceramic Composite specimen tested in compression at 20 MPa at 1200 °C in air

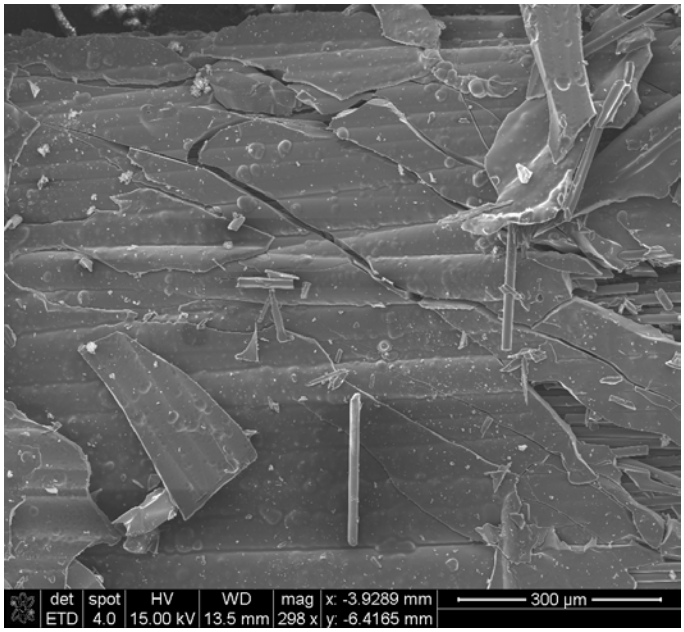

Figure 120 - SEM image showing cracked matrix of Hi-Nicalon/PyC/HyperSiC Ceramic Composite specimen tested in compression at 20 MPa at 1200 °C in air

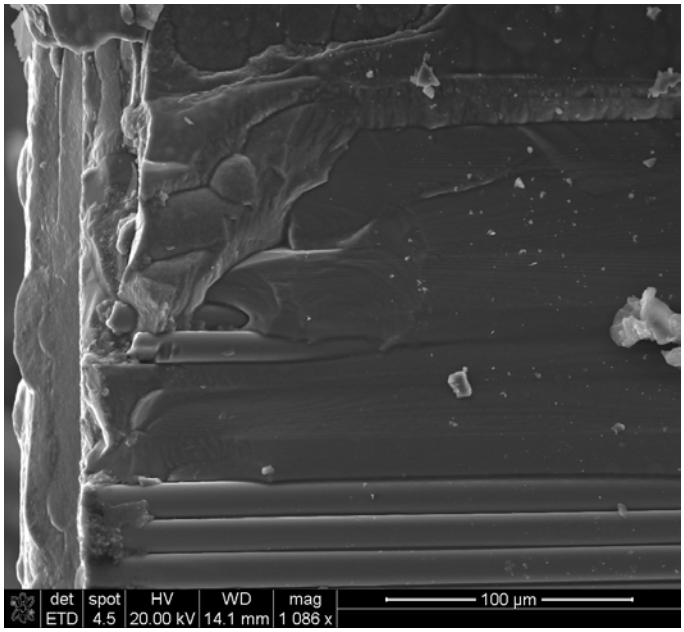

Figure 121 - SEM image showing cracked matrix toward edge of Hi-Nicalon/PyC/HyperSiC Ceramic Composite specimen tested in compression at 20 MPa at 1200 °C in air

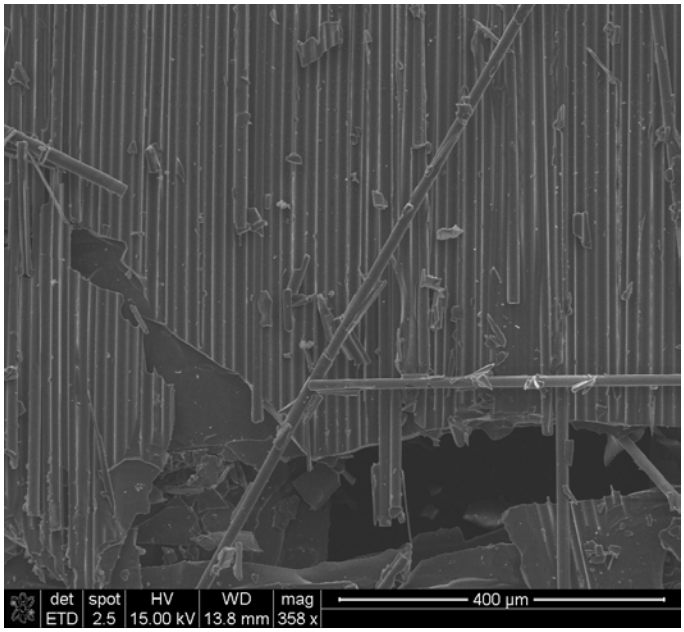

Figure 122 - SEM image showing clean fiber grooves in matrix of Hi-Nicalon/PyC/HyperSiC Ceramic Composite specimen tested in compression at 20 MPa at 1200 °C in air

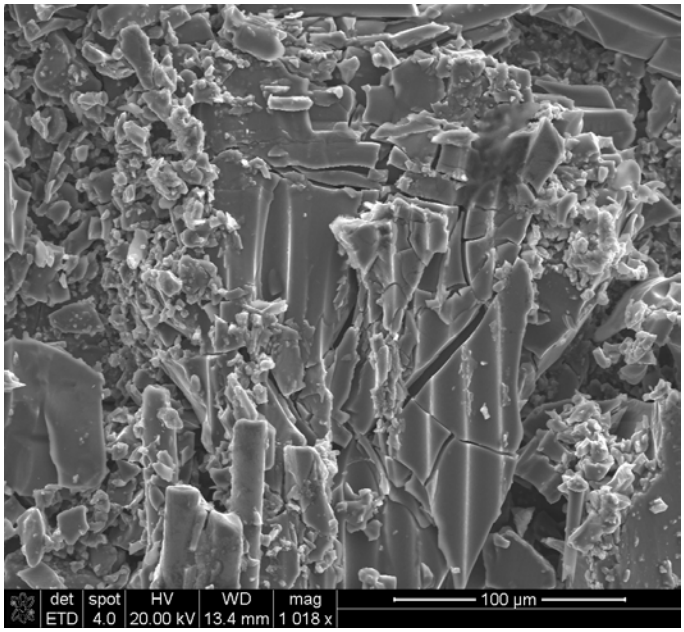

Figure 123 - SEM image showing cracked matrix with intact fiber grooves of Hi-Nicalon/PyC/HyperSiC Ceramic Composite specimen tested in compression at 20 MPa at 1200 °C in air

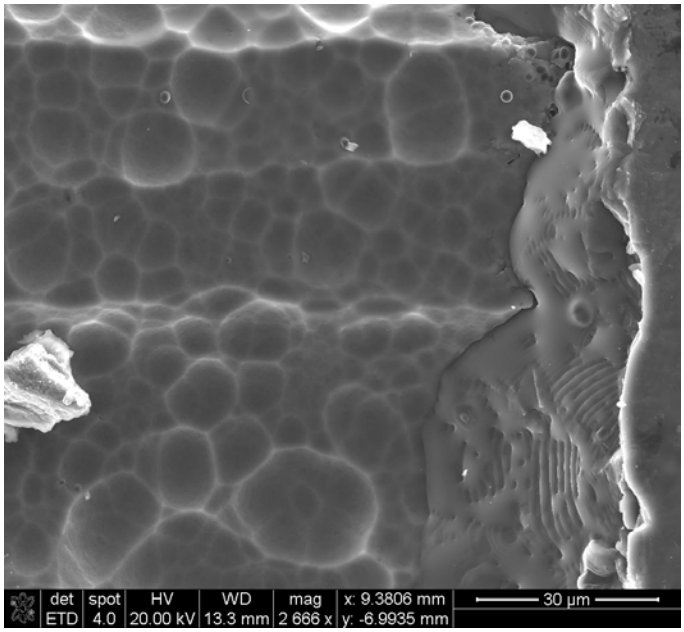

Figure 124 - SEM image showing glass emerging from matrix within matrix crack at edge of Hi-Nicalon/PyC/HyperSiC Ceramic Composite specimen tested in compression at 20 MPa at 1200 °C in steam

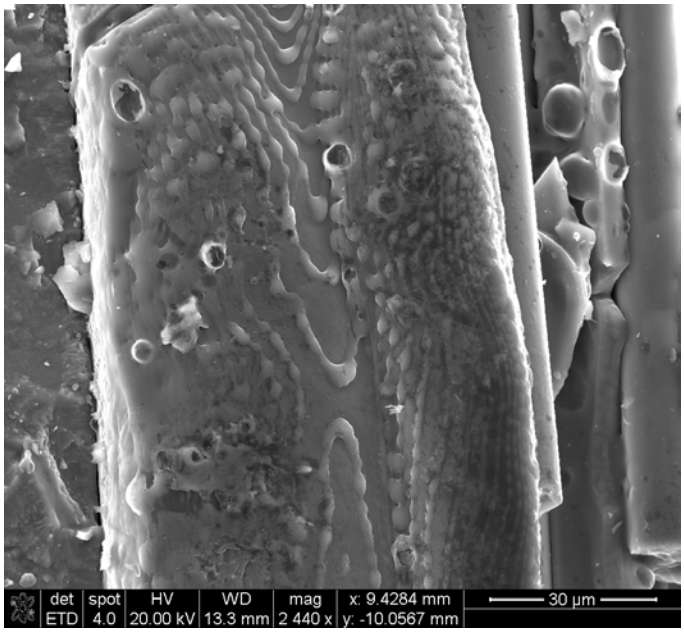

Figure 125 - SEM image showing glass emerging from matrix of Hi-Nicalon/PyC/HyperSiC Ceramic Composite specimen tested in compression at 20 MPa at 1200 °C in steam

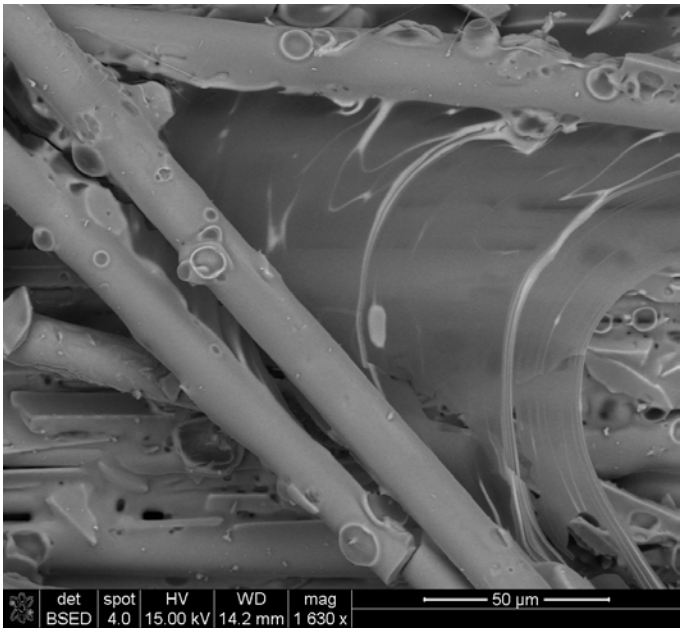

Figure 126 - SEM image showing thin glass film spread between two fibers of Hi-Nicalon/PyC/HyperSiC Ceramic Composite specimen tested in compression at 20 MPa at 1200 °C in steam

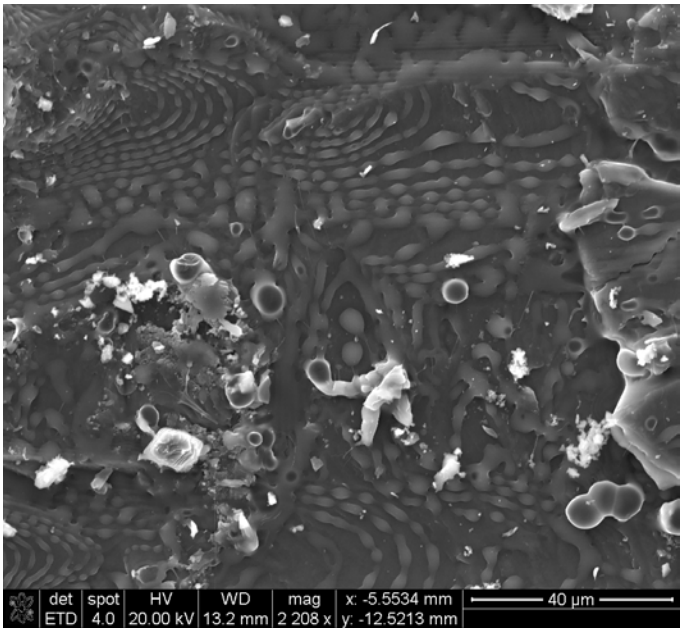

Figure 127 - SEM image showing glass emerging from matrix of Hi-Nicalon/PyC/HyperSiC Ceramic Composite specimen tested in compression at 20 MPa at 1200 °C in steam

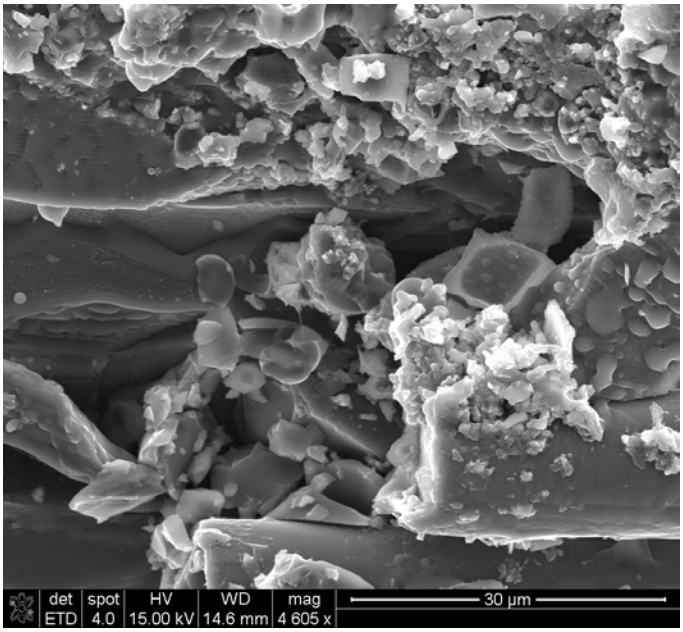

Figure 128 - SEM image showing glass emerging within matrix void of Hi-Nicalon/PyC/HyperSiC Ceramic Composite specimen tested in compression at 20 MPa at 1200 °C in steam

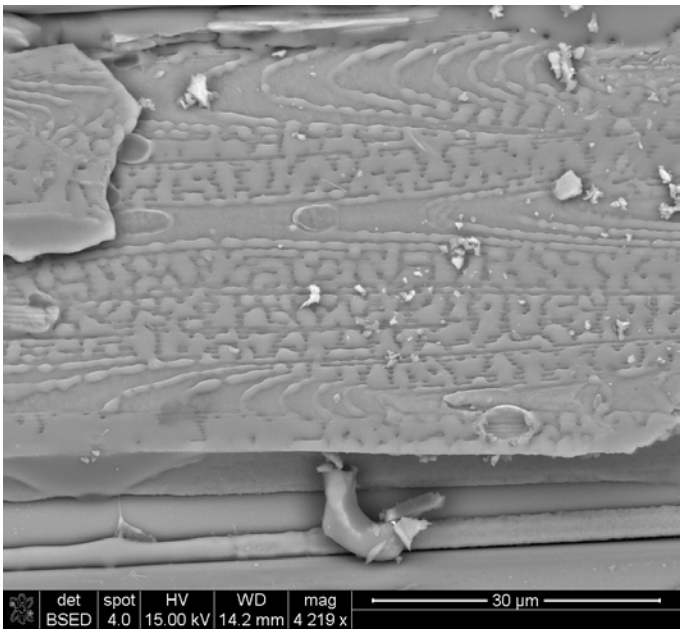

Figure 129 - SEM image showing glass emerging from matrix of Hi-Nicalon/PyC/HyperSiC Ceramic Composite specimen tested in compression at 20 MPa at 1200 °C in steam

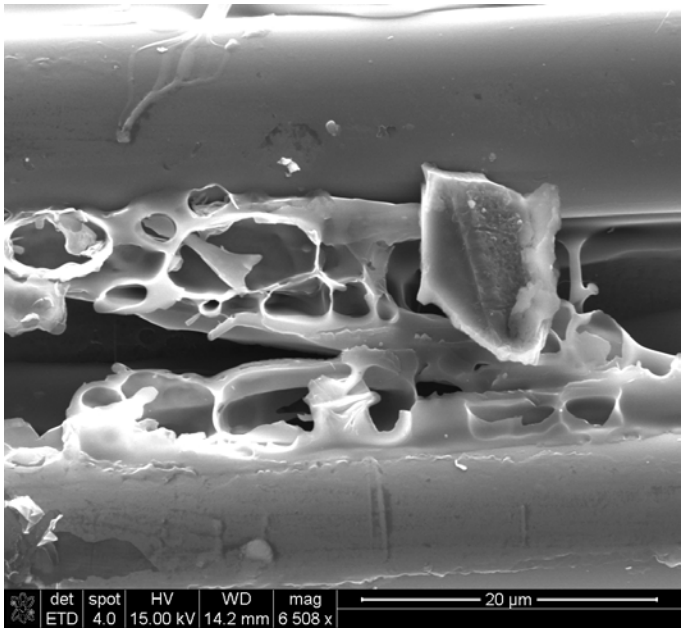

Figure 130 - SEM image showing glass formation between two fibers of Hi-Nicalon/PyC/HyperSiC Ceramic Composite specimen tested in compression at 20 MPa at 1200 °C in steam

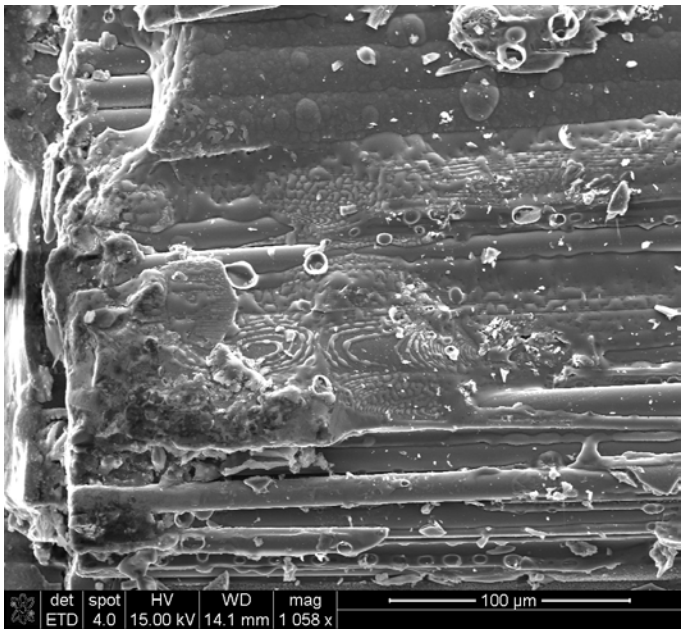

Figure 131 - SEM image showing glass emerging from matrix of Hi-Nicalon/PyC/HyperSiC Ceramic Composite specimen tested in compression at 20 MPa at 1200 °C in steam

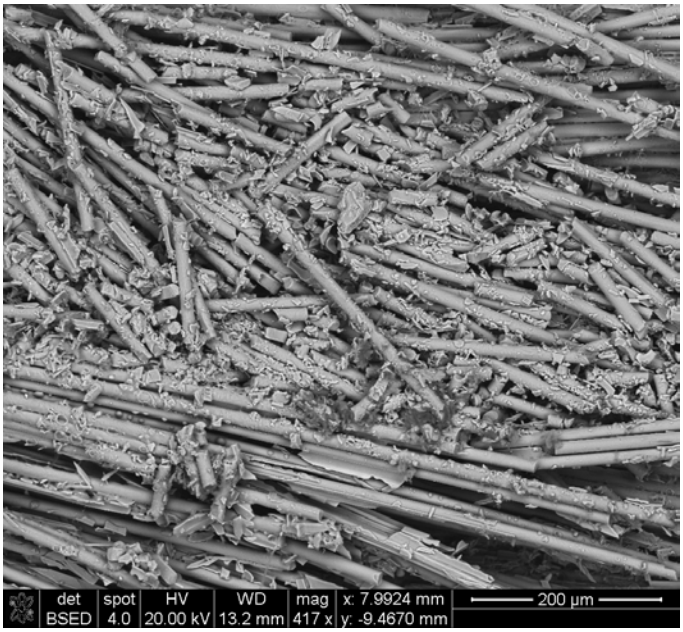

Figure 132 - SEM image showing fractured fibers bound with glass and matrix of Hi-Nicalon/PyC/HyperSiC Ceramic Composite specimen tested in compression at 20 MPa at 1200 °C in steam

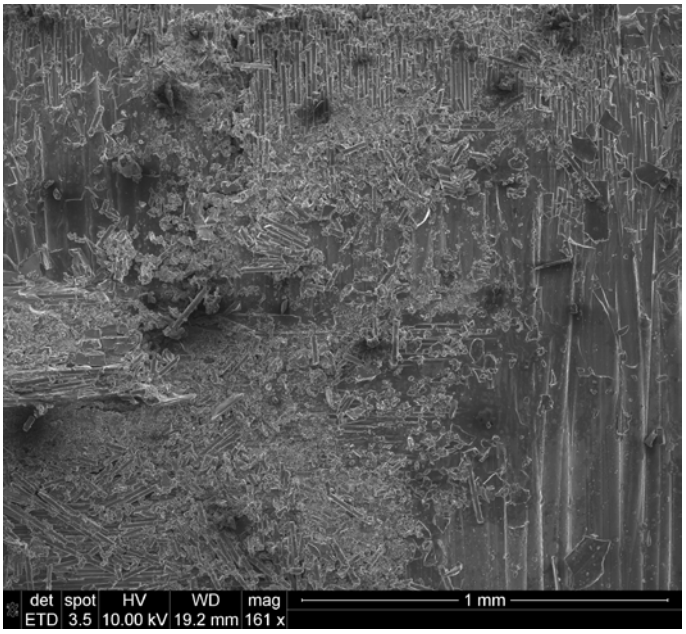

Figure 133 - SEM image showing delamination zone with minimal debris of Hi-Nicalon/PyC/HyperSiC Ceramic Composite specimen tested in compression at 22 MPa at 1200 °C in air

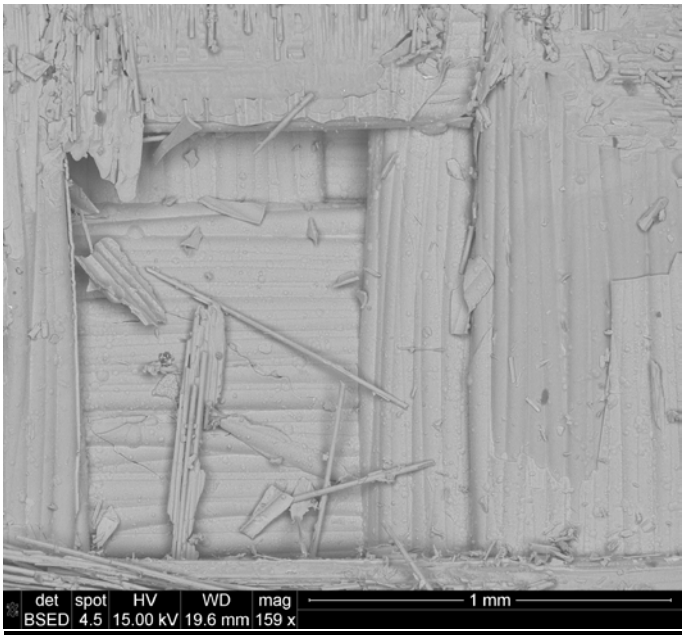

Figure 134 - SEM image showing clean delamination zone and void of Hi-Nicalon/PyC/HyperSiC Ceramic Composite specimen tested in compression at 22 MPa at 1200 °C in air

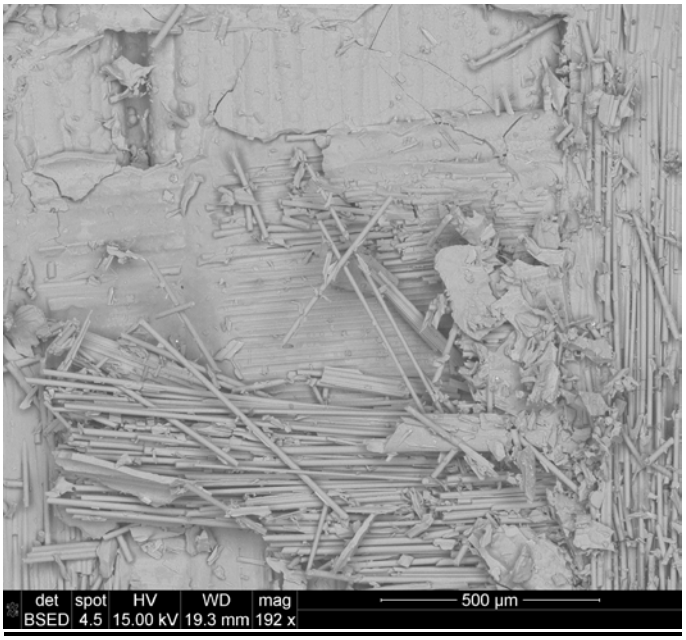

Figure 135 - SEM image showing delamination zone with debris of Hi-Nicalon/PyC/HyperSiC Ceramic Composite specimen tested in compression at 22 MPa at 1200 °C in air

Figure 136 - SEM image showing delamination zone with minimal debris of Hi-Nicalon/PyC/HyperSiC Ceramic Composite specimen tested in compression at 22 MPa at 1200 °C in air

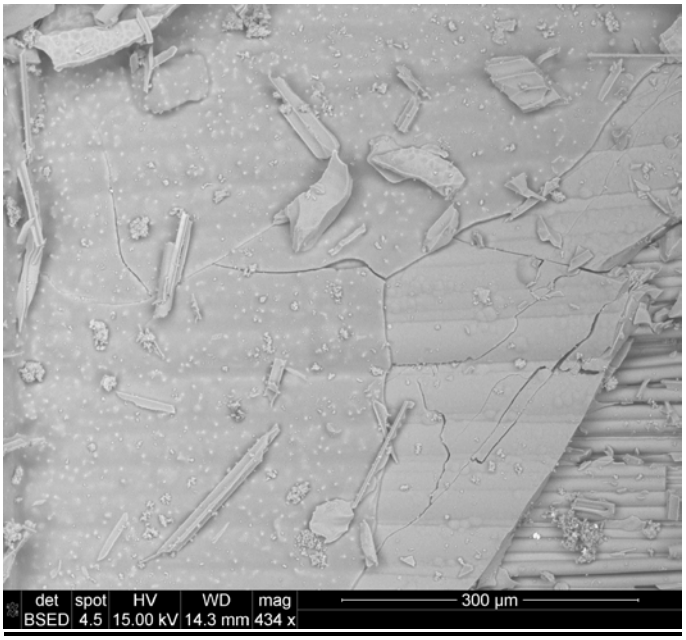

Figure 137 - SEM image showing smooth cracked matrix of Hi-Nicalon/PyC/HyperSiC Ceramic Composite specimen tested in compression at 22 MPa at 1200 °C in air

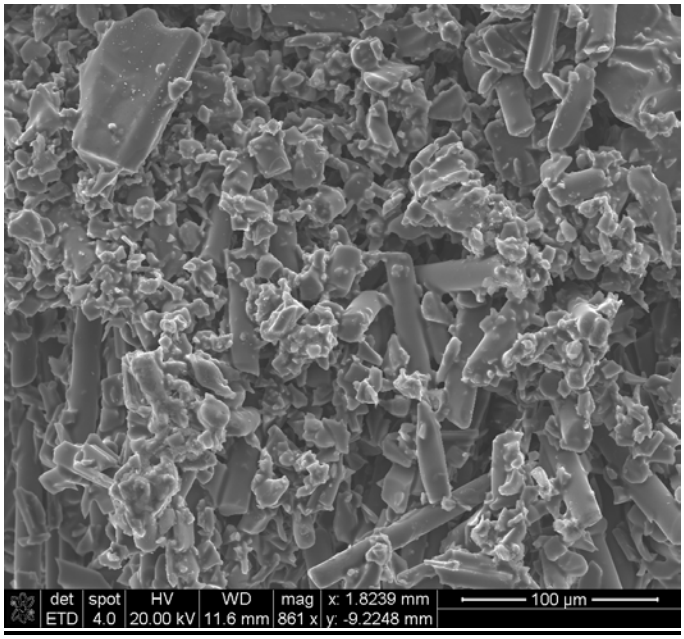

Figure 138 - SEM image showing surface debris of Hi-Nicalon/PyC/HyperSiC Ceramic Composite specimen tested in compression at 22 MPa at 1200 °C in air

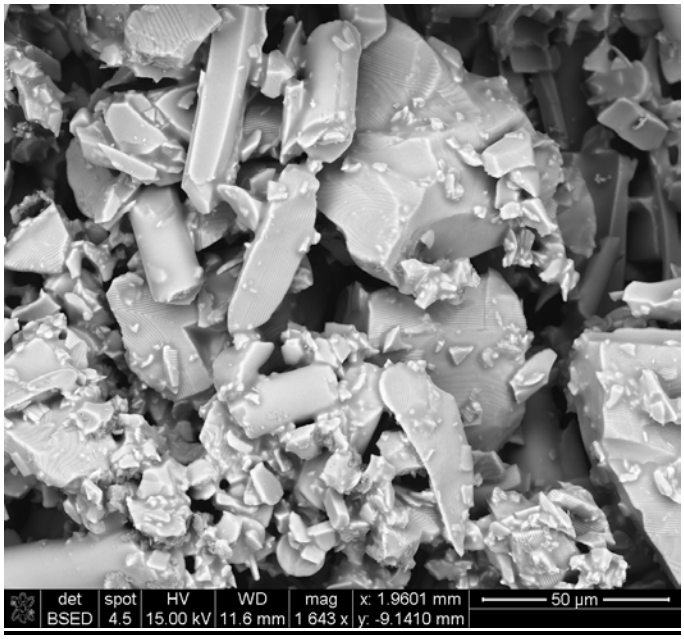

Figure 139 - SEM image showing clear matrix layers within debris of Hi-Nicalon/PyC/HyperSiC Ceramic Composite specimen tested in compression at 22 MPa at 1200 °C in air

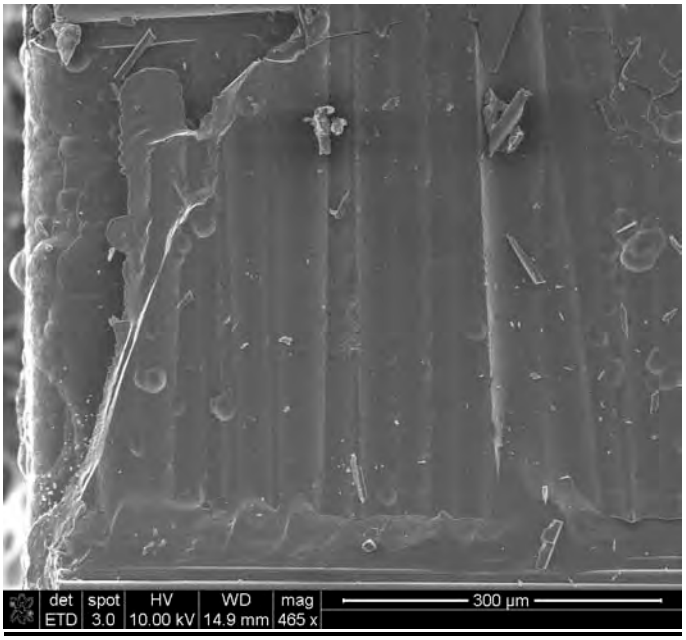

Figure 140 - SEM image showing delamination zone with intact matrix of Hi-Nicalon/PyC/HyperSiC Ceramic Composite specimen tested in compression at 22 MPa at 1200 °C in steam

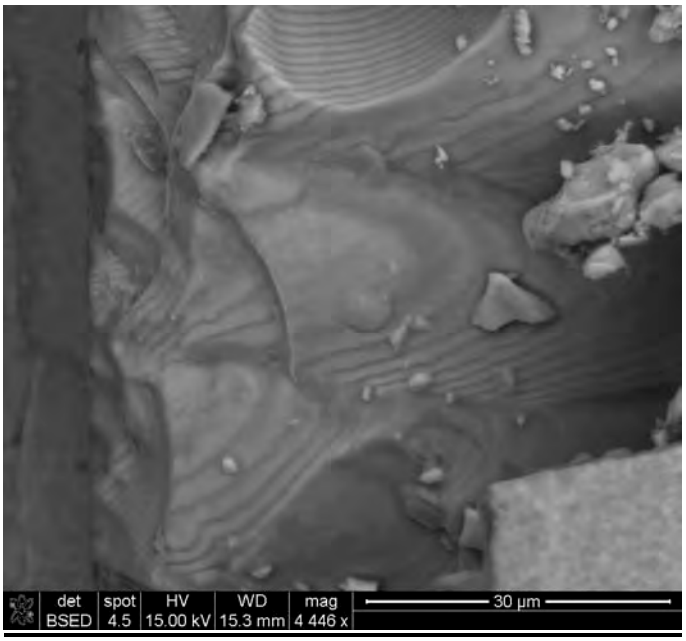

Figure 141 - SEM image showing delamination zone cracked matrix of Hi-Nicalon/PyC/HyperSiC Ceramic Composite specimen tested in compression at 22 MPa at 1200 °C in steam

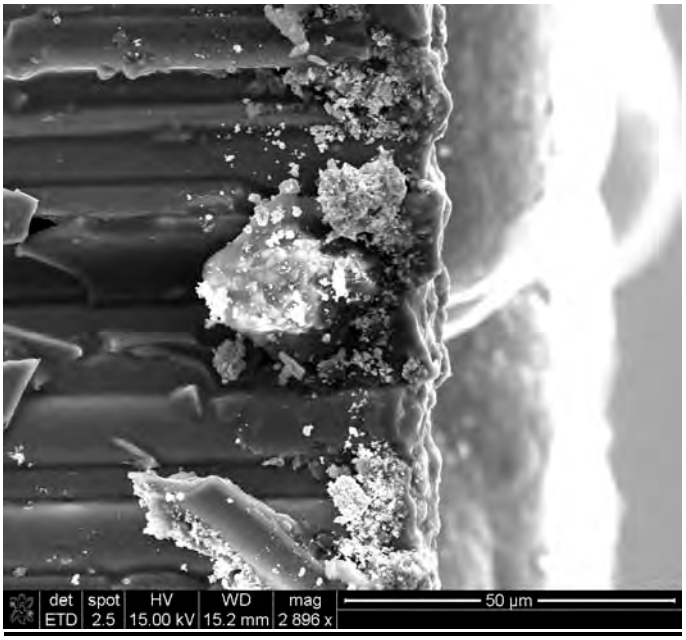

Figure 142 - SEM image showing beginning of glass formation at edge of Hi-Nicalon/PyC/HyperSiC Ceramic Composite specimen tested in compression at 22 MPa at 1200 °C in steam

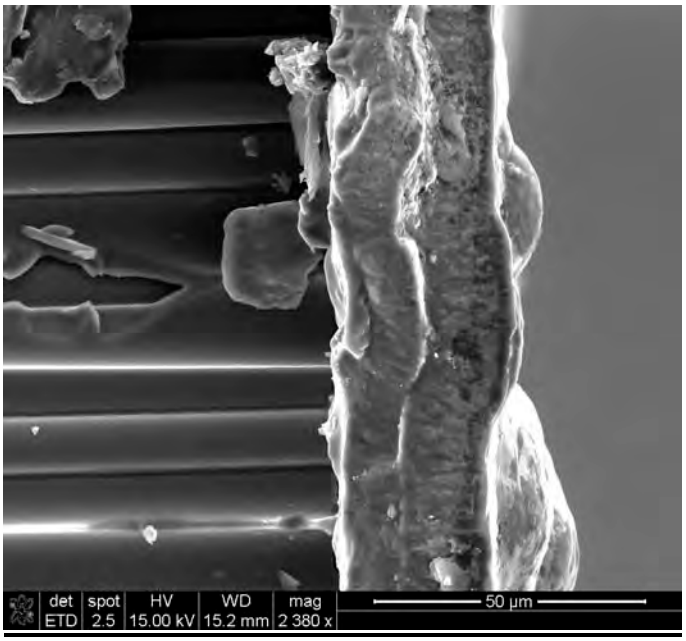

Figure 143 - SEM image showing beginning of glass formation at edge of Hi-Nicalon/PyC/HyperSiC Ceramic Composite specimen tested in compression at 22 MPa at 1200 °C in steam

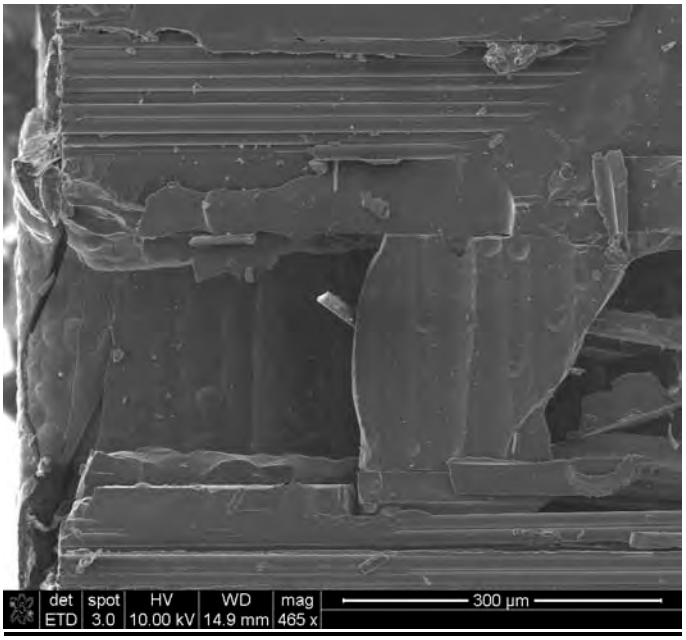

Figure 144 - SEM image showing cracked matrix without glass formation at edge of Hi-Nicalon/PyC/HyperSiC Ceramic Composite specimen tested in compression at 22 MPa at 1200 °C in steam

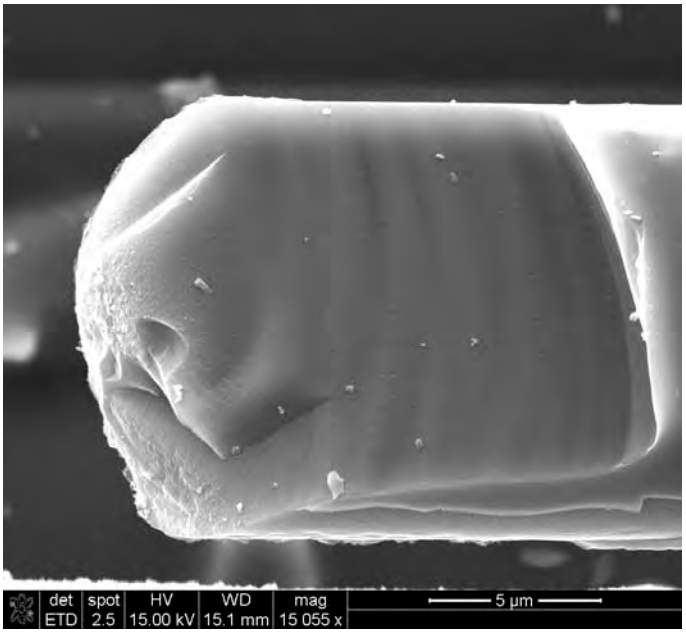

Figure 145 - SEM image showing fractured fiber of Hi-Nicalon/PyC/HyperSiC Ceramic Composite specimen tested in compression at 22 MPa at 1200 °C in steam

Bibliography

[1] K. K. Chawla . *Ceramic Matrix Composites* 1993.

[2] H. Ohnabe, S. Masaki, M. Onozuka, K. Miyahara and T. Sasa. Potential application of ceramic matrix composites to aero-engine components. *Composites Part A: Applied Science and Manufacturing 30(4),* pp. 489-496. 1999.

[3] L. P. Zawada, J. Staehler and S. Steel. Consequence of intermittent exposure to moisture and salt fog on the high-temperature fatigue durability of several ceramic-matrix composites. *J Am Ceram Soc 86(8),* pp. 1282-1291. 2003.

[4] J. A. DiCarlo, H. Yun, G. N. Morscher and R. T. Bhatt. *Handbook of Ceramic Composites.*2010.

[5] W. Krenkel, R. Naslain, H. Schneider and International Conference on High-Temperature Ceramic-Matrix Composites. *High temperature ceramic matrix composites*. 2001.

[6] M. Parlier and M. H. Ritti. State of the art and perspectives for oxide/oxide composites. *Aerospace Science and Technology 7(3),* pp. 211-221. 2003.

[7] M. K. Ferber, H. T. Lin and J. Keiser. Oxidation behavior of non-oxide ceramics in a high-pressure, high-temperature steam environment. *ASTM Spec. Tech. Publ. (1392),* pp. 201-215. 2001.

[8] M. B. Ruggles-Wrenn, D. T. Christensen, A. L. Chamberlain, J. E. Lane and T. S. Cook. Effect of frequency and environment on fatigue behavior of a CVI SiC/SiC ceramic matrix composite at 1200 °C. *Composites Sci. Technol. 71(2),* pp. 190-196. 2011.

[9] K. S. Mazdiyasni. *Fiber reinforced ceramic composites: Materials, processing, and technology*. 1990.

[10] S. Mall and W. A. Weidenaar. Tension-compression fatigue behaviour of fibre-reinforced ceramic matrix composite with circular hole. *Composites 26(9),* pp. 631-636. 1995.

[11] S. R. Choi, R. W. Kowalik, D. J. Alexander and N. P. Bansal. Assessments of life limiting behavior in interlaminar shear for hi-nic SiC/SiC ceramic matrix composite at elevated temperature. *Ceram. Eng. Sci. Proc. 28(2),* pp. 179-189. 2008.

[12] S. R. Choi and N. P. Bansal. Interlaminar tension/shear properties and stress rupture in shear of various continuous fiber-reinforced ceramic matrix composites. *Ceramic Transactions 175*pp. 119-134. 2006.

[13] P. Brondsted, F. E. Heredia and A. G. Evans. In-plane shear properties of 2-D ceramic matrix composites. *Journal of the American Ceramic Society. 77(10),* pp. 2569. 1994.

[14] E. Lara-Curzio and M. K. Ferber. Shear strength of continuous fiber ceramic composites. *ASTM Special Technical Publication. 1309*pp. 31. 1997.

[15] O. Unal and N. P. Bansal. In-plane and interlaminar shear strength of a unidirectional hi-nicalon fiber-reinforced celsian matrix composite. *Ceramics International. 28(5),* pp. 527. 2002.

[16] S. R. Choi and N. P. Bansal. Shear strength as a function of test rate for SiCf~/BSAS ceramic matrix composite at elevated temperature. *Journal- American Ceramic Society,* 87pp. 1912-1918. 2004.

[17] S. R. Choi, N. P. Bansal, A. M. Calomino and M. J. Verrilli. Shear strength behaviors of ceramic matrix composites at elevated temperatures. Presented at 106th Annual Meeting of the American Ceramic Society, April 18, 2004 - April 21. 2004.

[18] F. C. Campbell. *Manufacturing Technology for Aerospace Structural Materials* 2006.

[19] N. P. Bansal. *Handbook of ceramic composites*. 2005.

[20] "Standard Test Method for Interlaminar Shear Stength of 1-D and 2-D Continuous Fiber-Reinforced Advanced Ceramics at Elevated Temperatures." Practice No. C1425-05. American Society for Testing and Materials, 2005.

[21] N. J. J. Fang and Tsuwei Chou. Characterization of interlaminar shear strength of ceramic matrix composites. *J Am Ceram Soc 76:10*pp. 2539-2548. 1993.

[22] Laffey, P.D. *The Effects of Environment on the Interlaminar Shear Performance of an Oxide-Oxide Ceramic Matrix Composite at Elevated Temperature.* MS thesis, AFIT/GAE/ENY/07-J11. School of Engineering and Management, Air Force Institute of Technology (AU), Wright-Patterson AFB OH, March 2007.

[23] Mehrman, J.M. *Effect of Hold Times on Fatigue Behavior of Nextel™ 720/Alumina Ceramic Matrix Composite at 1200°C in Air and in Steam Environment.* MS thesis, AFIT/GA/ENY/06-M23. School of Engineering and Management, Air Force Institute of Technology (AU), Wright-Patterson AFB, OH March 2006.

[24] Siegert, G. *Effect of Environment on Creep Behavior of an Oxide/Oxide CFCC with ±45° Fiber Orientation.* MS thesis, AFIT/GA/ENY/06-J15. School of Engineering and Management, Air Force Institute of Technology (AU), Wright-Patterson AFB, OH June 2006.

[25] Choi, S. R., A. M. Calomino, N. P. Bansal, and M. J. Verrilli. *Life Limiting Behavior in Interlaminar Shear of Continuous Fiber-Reinforced Ceramic Matrix Composites at Elevated Temperatures*. NASA/TM 2006-214088, 2006.

[26] S. Martin. Oxidation of boron carbide at high temperatures. *J. Nucl. Mater. 336(2–3),* pp. 185-193. 2005.

REPORT DOCUMENTATION PAGE

Form Approved
OMB No. 074-0188

1. REPORT DATE *(DD-MM-YYYY)*	**2. REPORT TYPE**	**3. DATES COVERED** *(From – To)*
22-03-2012	Master's Thesis	SEP 10 – MAR 12

TITLE AND SUBTITLE

Creep Behavior in Interlaminar Shear of a CVI SiC/SiC Composite at Elevated Temperatures in Air and Steam

5a. CONTRACT NUMBER

5b. GRANT NUMBER

5c. PROGRAM ELEMENT NUMBER

6. AUTHOR(S)

Pope, Matthew T.

5d. PROJECT NUMBER

5e. TASK NUMBER

5f. WORK UNIT NUMBER

7. PERFORMING ORGANIZATION NAMES(S) AND ADDRESS(S)
Air Force Institute of Technology
Graduate School of Engineering and Management (AFIT/ENY)
2950 Hobson Way, Building 640
WPAFB OH 45433-8865

8. PERFORMING ORGANIZATION REPORT NUMBER

AFIT/GMS/ENY/12-M02

9. SPONSORING/MONITORING AGENCY NAME(S) AND ADDRESS(ES)
Intentionally left blank

10. SPONSOR/MONITOR'S ACRONYM(S)

11. SPONSOR/MONITOR'S REPORT NUMBER(S)

12. DISTRIBUTION/AVAILABILITY STATEMENT
APPROVED FOR PUBLIC RELEASE; DISTRIBUTION UNLIMITED.

13. SUPPLEMENTARY NOTES
This material is declared a work of the U.S. Government and is not subject to copyright protection in the United States.

14. ABSTRACT

This research investigated the interlaminar shear performance of a SiC/SiC ceramic matrix composite. The interlaminar shear performance was observed in compression of double notched specimens (DNS) at 1200°C in both laboratory air and in steam. Compression to failure tests determined the as-processed interlaminar shear strength and interlaminar shear creep tests were conducted with stresses ranging from -22 MPa to -16 MPa. Primary and secondary creep regimes were observed in all creep tests.

The specimens tested in creep at –16 MPa in air achieved run-out, defined as 100 hours at creep stress. The residual strength decreased slightly after 100 h of creep in air at 1200°C and decreased significantly after 100 h in steam. The fracture surfaces of all samples were examined in order to determine the failure and environmental degradation mechanisms behind the reduced creep performance of the matrix in steam.

15. SUBJECT TERMS
Ceramic Matrix Composites, Composite Materials, Ceramic Fibers, Ceramic Materials, Fiber Reinforced Composites, HyperSiC

16. SECURITY CLASSIFICATION OF:			**17. LIMITATION OF ABSTRACT**	**18. NUMBER OF PAGES**	**19a. NAME OF RESPONSIBLE PERSON**
a. REPORT	**b. ABSTRACT**	**c. THIS PAGE**			Dr. Marina Ruggles-Wrenn
U	**U**	**U**	**UU**	xx	**19b. TELEPHONE NUMBER** *(Include area code)* (937) 255-3636, ext 4641; email: marina.ruggles-wrenn@afit.edu

Standard Form 298 (Rev. 8-98)
Prescribed by ANSI Std. Z39-18